

EXPERIMENTAL STUDY OF CELLULAR INSTABILITIES IN NON-PREMIXED FLAMES

THÈSE N° 3336 (2005)

PRÉSENTÉE À LA FACULTÉ SCIENCES ET TECHNIQUES DE L'INGÉNIEUR

Institut des sciences de l'énergie

SECTION DE GÉNIE MÉCANIQUE

ÉCOLE POLYTECHNIQUE FÉDÉRALE DE LAUSANNE

POUR L'OBTENTION DU GRADE DE DOCTEUR ÈS SCIENCES

PAR

David LO JACONO

DEA en dynamique des fluides, Institut National Polytechnique de Toulouse, France
et de nationalité française

acceptée sur proposition du jury:

Prof. P.A. Monkewitz, directeur de thèse
Prof. K. Boulouchos, rapporteur
Prof. M. Matalon, rapporteur
Prof. G. Searby, rapporteur

Lausanne, EPFL
2005

Remerciements

Je tiens à commencer mes remerciements par mon directeur de thèse, Peter Monkewitz, qui m'a communiqué une partie de son expérience, de son savoir puis pour m'avoir guidé, encouragé, conseillé, fait beaucoup voyager pendant quatre ans tout en me laissant une grande liberté. Je le remercie également de m'avoir laissé continuer ma recherche sur l'hydrodynamique dans des géométries confinées initié lors de mon DEA à Toulouse. Je remercie Alain Bergeon et Franck Plouraboué pour m'avoir accueilli en DEA et pour m'avoir invité régulièrement tout au long de ma thèse à l'IMFT et à l'Université Paul Sabatier à Toulouse afin de continuer notre collaboration. Je leur exprime ici tout ma gratitude pour leurs conseils, encouragements et leurs amitiés.

J'exprime ma sincère reconnaissance aux membres du jury, Geoff Searby, Konstantinos Boulouchos et Moshe Matalon pour leurs remarques et suggestions qui ont amélioré la qualité de ce manuscrit. Je remercie tout spécialement Moshe Matalon pour son aide et sa collaboration depuis le début de cette thèse.

Cette thèse n'aurait pu aboutir sans le soutien moral et technique du Laboratoire de Mécanique des Fluides. Je remercie Paul Papas pour sa collaboration, sa confiance et sa patience à mes débuts. Je remercie Trong-Vien Truong pour ses conseils avisés pour mes mesures. Un très grand merci à l'équipe de l'atelier pour leur grand professionnalisme et leur patience à mon égard. Je pense notamment à Bernard Savary et à Gaby Grandjean qui ont dû réaliser tout au long de cette thèse les pièces nécessaires au stand expérimental à partir de (très) simples croquis. Je remerci Navid Bohrani, Bartu Ugurtas et Eva Gasser pour leur soutien moral et leurs gentillesse. Je tiens à remercier les thésards du laboratoire pour leurs aides, amitiés, conseils

et soutien pendant toutes ces années. Un grand merci aux ‘anciens’: Marc Fūri, Jean-Daniel Ruedi, Redha Raïis et Denis Martinand. Aux ‘jeunes’: Radboud Nelissen et Émeric Grandjean, et aux ‘nouveaux’: Étienne Robert et Richard Vonlanten. Merci à eux de m’avoir supporté lors de nos cohabitations dans le ‘labo’ et dans le ‘bureau’ et d’avoir supporté mes humeurs diverses et variées. Je tiens à remercier chaudement celui qui à commencé sa thèse en même temps que moi, celui qui m’a supporté (dans tout les sens du terme) le plus pendant toute ces années avec une longue collocation : Chris Pipe. Sa patience, son flegme typiquement britannique et son amitié m’ont été d’une très grande aide. Je tiens également à remercier les autres collègues des laboratoires voisins, je pense notamment à Thierry Ursenbacher, à Emmanuel Leriche et à Philippe Metzener. Je remercie tout particulièrement Roland Bouffanais pour sa présence quotidienne, son soutien moral et technique et son amitié. Je remercie l’équipe ETH-Zurich, notamment Christos Frouzakis pour son aide et sa collaboration sur ce sujet. Je remercie Friederich Busse pour ses conseils avisés. Je remercie mes étudiants pour m’avoir supporté, bon vent à eux.

Je remercie également, les thésards ‘extérieurs’, ceux qui m’ont aidé par leurs discussions, leurs conseils, leurs soutien et la relecture de cette thèse : Arnaud Antkowiak, Laurent Lacaze, Jérôme Hébrard et Cecilia Robitallé. Evidemment je n’oublie pas mes amis de Toulouse et d’ailleurs pour m’avoir encouragé, hebergé, accueilli, amusé, en somme pour leurs amitiés. La liste serait longue et il en manquerait mais je veux qu’ils sachent que leur soutien moral ainsi que leur encouragement ont été plus que nécessaires. Je remercie Juliette, celle qui à partagé le plus de temps avec moi.

Je remercie mes parents qui m’ont toujours encouragé dans mes choix, ma soeur Laura pour sa relecture et mon frère Frédéric.

Malgré les distractions dont je fait souvent preuve, malgré la distance que j’ai pu prendre en me consacrant à mes recherches, que mes ami(e)s et ma famille soient assurés que leur amitié m’est plus précieuse que mes travaux.

Résumé

Ce travail consiste en une étude expérimentale systématique visant à élucider les conditions pour lesquelles on observe des formations cellulaires dans des flammes de diffusion de type hydrogène proche de l’extinction. La formation de ces instabilités cellulaires ont été étudiées avec plusieurs types de brûleurs, les brûleurs classiques dits “jet” (jet axisymétrique et jet bidimensionnel) et un nouveau brûleur unidimensionnel.

Les principaux paramètres régissant ces instabilités cellulaires sont les nombres de Lewis du combustible et du comburant et la composition initiale de mélange (rapport entre la concentration de combustible et la concentration de comburant normalisé par le rapport stoechiométrique). La formation des flammes cellulaires est favorisée pour des nombres de Lewis relativement bas et proches de la limite d’extinction. Pour des brûleurs “jet”, la zone d’instabilité cellulaire diminue soit en augmentant la composition initiale de mélange, soit en augmentant la vitesse de sortie du combustible. Pour un mélange particulier de combustible, les longueurs d’ondes associées aux instabilités cellulaires se sont avérées diminuées pour des concentrations d’oxygène décroissantes et pour des vitesses de jet croissantes.

Afin d’étudier les instabilités cellulaires dans des flammes de diffusion sans effet hydrodynamique, un nouveau brûleur a été développé dans le but de réaliser expérimentalement une flamme de diffusion plane unidimensionnelle non-étirée, précédemment uniquement considérée dans des modèles théoriques. Les zones d’instabilités cellulaires pour des flammes de type hydrogène sont en bon accord avec les prédictions théoriques et avec les expériences menés dans les brûleurs “jet” résultats du comportement d’une flamme de diffusion proche de l’extinction issu d’un tel dispositif sont comparables à ceux issu des brûleurs “jet”.

Abstract

A systematic experimental study was performed to elucidate the conditions for which cellular patterns of diluted hydrogen diffusion flames near extinction were observed. The formation of cellular instabilities was studied for several burners: jet burners (axisymmetric jet and two-dimensional jet) and a novel one-dimensional burner.

The fuel and oxidizer Lewis numbers and the initial mixture strength (fuel-to-oxygen concentration ratio normalized by the stoichiometric value) were identified as the key governing parameters. The formation of cellular flames occurs for low reactant Lewis numbers (less than one) and near the extinction limit. For the jet burners, the parameter space for cellularity was found to decrease with either decreasing initial mixture strength, either increasing the fuel jet velocity. For a given fuel mixture, the wavelength associated with the cellular instabilities was found to decrease with either decreasing oxygen concentration, or increasing the fuel jet velocity.

To study the suppression of hydrodynamic effects on the cellular instabilities, a unique burner was constructed to experimentally realize a one-dimensional *unstrained* planar non-premixed flame, previously only considered in idealized theoretical models. The results show that when the oxidizer diffuses against the bulk flow the propensity of cellular instabilities increases with decreasing the initial mixture strength which is in agreement with the theoretical predictions for this type of burner as well as experimental results for jet diffusion flames.

Contents

1	Introduction	1
2	Jet diffusion flame facilities	11
2.1	Introduction	11
2.2	Measurement techniques	12
2.2.1	Properties of the fuel and oxidizers	12
2.2.2	Flow controller system	13
2.2.3	Traverse equipment	14
2.2.4	Hotwire anemometer	14
2.2.5	Laser Doppler anemometry (LDA)	15
2.3	Description of facilities	18
2.3.1	Axisymmetric jet burner	18
2.3.2	Wolfhard–Parker burner	20
3	Cellular instabilities in jet diffusion flames	23
3.1	Introduction	23
3.2	Effect of reactant composition on cellular instabilities	
	<i>Combust. Theory and Modelling</i> , 7 , 2003 [67]	24
3.2.1	Introduction	25
3.2.2	Experimental description	27
3.2.3	Experimental results	28
3.2.4	Discussion and conclusions	34
3.3	Jet burner velocity profiles	38
3.3.1	Axisymmetric jet burner	38
3.3.2	Wolfhard–Parker burner	39
3.3.3	Determining the vorticity thicknesses	40

CONTENTS

3.4	Effect of jet velocity on cellular instabilities	42
3.4.1	Procedure	44
3.4.2	Results	48
4	Realization of a nearly one-dimensional diffusion flame	57
4.1	Introduction	57
4.2	The theoretical one-dimensional burner	58
4.3	Design considerations <i>Proc. Comb. Inst.</i> , 30 , 2005 [66], expanded	62
4.4	Experimental characterization of the burner <i>Proc. Comb. Inst.</i> , 30 , 2005 [66], expanded	67
4.4.1	Velocity profiles	67
4.4.2	Temperature and heat loss consideration	70
4.4.3	Flame position measurements	71
5	First investigation of cell formation in the new burner	77
5.1	Introduction	77
5.2	Preliminary results <i>Proc. Comb. Inst.</i> , 30 , 2005 [66]	78
5.3	Additional comments on the reverse configuration	86
5.4	Comments on possible thermal-convection	88
6	Summary and future work	93
A	Thermal properties of the reactants	97
	Curriculum vitae	115

List of Figures

1.1	Examples of morphogenesis.	2
1.2	Illustration of the morphogenesis mechanism.	3
1.3	Typical variation of the maximum reaction temperature with the Damköhler number for a non-premixed mixture.	6
1.4	Schematic diagram of the thermo-diffusive instability of a diffusion flame.	8
2.1	Schematic of the axisymmetric jet (AJ) burner apparatus. . .	19
2.2	Schematic of the Wolfhard–Parker (WP) burner apparatus. . .	21
3.1	Example of an hexagonal cellular flame instability of CH ₄ -O ₂ diffusion flame in the AJ burner.	27
3.2	Extinction limit and boundaries of different cellular instabilities observed for CO ₂ diluted, H ₂ -O ₂ jet diffusion flames. AJ burner for fixed velocities.	29
3.3	Streamwise integrated chemiluminescence images taken from the downstream jet axis.	30
3.4	Forward- and backward-transition oxygen values observed for 22.5% H ₂ -77.5% CO ₂ jet diffusion flames burning in O ₂ -CO ₂ . .	32
3.5	Theoretical cellular instability boundaries (lines) for an ideal unstretched planar flame and experimental jet flame data near extinction in the Le _F -Le _O plane.	36
3.6	Typical velocity measurements of the AJ burner.	39
3.7	Typical velocity measurements of the WP burner.	40
3.8	Vorticity thickness for the AJ and WP burner.	41

LIST OF FIGURES

3.9	Examples of several cellular modes coexisting for a particular state.	43
3.10	Typical two-dimensional cellular flame instability of a diluted hydrogen diffusion flame, from the WP burner.	44
3.11	Example of two top views of the AJ burner for two different fuel velocities.	45
3.12	Method for determining cellular wavelengths in the WP apparatus (1).	47
3.13	Method for determining cellular wavelengths in the WP apparatus (2).	47
3.14	Extinction limit and boundaries of different cellular instabilities observed for H ₂ -O ₂ diffusion flames in the AJ burner, for fixed oxidizer conditions.	49
3.15	Extinction limit and boundaries of the onset and lift-off of cellular instabilities observed for H ₂ -O ₂ diffusion flames in the WP burner.	50
3.16	Cellular wavelength measurements in the AJ and WP burner, versus fuel velocity for fixed initial mixture strength (1). . . .	52
3.17	Cellular wavelength measurements in the AJ and WP burner, versus fuel velocity for fixed initial mixture strength (2). . . .	53
3.18	Cellular wavelength measurements in the AJ and WP burner, versus initial mixture strength for fixed velocity conditions (1). . . .	54
3.19	Cellular wavelength measurements in the AJ and WP burner, versus initial mixture strength for fixed velocity conditions (2). . . .	55
4.1	Schematic of the ideal 1-D model.	59
4.2	Schematic of the idealized burner and sketch of the experimental realization.	63
4.3	Schematic of the 1-D burner, Mark I.	64
4.4	Section of the numerical simulation taken at the mid-plane of the computational domain.	66
4.5	Example of a flame side view in the 1-D burner.	67
4.6	One-dimensional burner, Mark Ia.	68
4.7	Velocity field and associated dimensional strain rate.	69

LIST OF FIGURES

4.8	Temperature profiles in the 1-D burner	71
4.9	Flame stand-off distance, experimental data and theoretical line.	75
5.1	Near-extinction limit and cellular instability boundaries observed for nearly unstrained planar non-premixed CO ₂ -diluted H ₂ -O ₂ flames.	79
5.2	Digital images of cellular instabilities in the 1-D burner.	80
5.3	Near-extinction limits observed in nearly unstrained planar non-premixed CO ₂ -diluted H ₂ -O ₂ flames.	87
5.4	Rayleigh number calculated for a H ₂ -O ₂ diluted in CO ₂ diffusion flames.	91
A.1	Properties of pure H ₂ , O ₂ , and CO ₂ versus temperature.	98
A.2	Kinematic viscosities and Prandtl numbers of H ₂ -O ₂ diluted in CO ₂ mixtures.	99
A.3	Fuel and oxidizer Lewis numbers for H ₂ -O ₂ diluted in CO ₂ mixtures.	100
A.4	Fuel and oxidizer Schmidt numbers of H ₂ -O ₂ diluted in CO ₂ mixtures.	101

LIST OF FIGURES

List of Tables

1.1	Wavelength of cellular instabilities for various reactants and configurations.	10
2.1	LDA specification.	16
3.1	Characteristic parameters for various flames near extinction in various burners.	35
4.1	Range of conditions for flame position measurements. For each initial reactant mixture investigated, the minimum and maximum parameter values are reported.	73

LIST OF TABLES

Nomenclature

Abbreviations

AJ	Axisymmetric jet
CF	Counterflow burner
CTA	Constant Temperature Anemometry
FB	Fuel bottom configuration
FT	Fuel top configuration
HW	Hotwire
I.D.	Inner diameter
LDA	Laser Doppler anemometry
NEF	Near equidiffusional formulation
O.D.	Outer diameter
SVF	Slowly varying flame
WP	Wolfhard–Parker

Chemical abbreviations

Ar	Argon
Al_2O_3	Aluminium oxide
CO_2	Carbon dioxide

Nomenclature

CF₄ Tetrafluoromethane

C₃H₈ Propane

CH₄ Methane

H₂ Hydrogen

He Helium

Kr Krypton

N₂ Nitrogen

O₂ Oxygen

OH Hydroxyl radical

SF₆ Sulfur hexafluoride

Xe Xenon

Greek letters

α Volumetric thermal expansion K^{-1}

ΔT Temperature differential K

δ_ω Vorticity thickness m

ϕ Initial mixture strength (molar)

ϕ_m Initial mixture strength (mass)

λ Thermal conductivity $\text{W}/(\text{m}\cdot\text{K})$

μ Dynamic viscosity $\text{kg}/(\text{m}\cdot\text{s})$

ν Kinematic viscosity $\text{m}^2\cdot\text{s}^{-1}$

ν'_k Stoichiometric coefficient of species k

ω Chemical reaction rate s^{-1}

NOMENCLATURE

ρ Density kg.m³

Adimensionalized number

Dam Damköhler number

Le Lewis number

Pe Péclet number

Pr Prandtl number

Ra Rayleigh number

Re Reynolds number

Sc Schmidt number

Roman letters

A Arrhenius pre-exponential factor

c_p Specific heat at constant pressure J/(kg.K)

\mathcal{D}_k Mass diffusivity of species k m².s⁻¹

\mathcal{D}_{th} Thermal diffusivity of the mixture m².s⁻¹

E_a Activation energy J

g Acceleration of gravity m².s⁻¹

L Characteristic length m

Q Total heat release J/m³

q Heat release per unit mass of fuel supplied J/kg

Q_F, Q_O Flow rate of fuel mixture and oxidizer mixture, respectively m³.s⁻¹

R Gas constant J/(mol.K)

s Tube center-to-center spacing m

Nomenclature

T	Temperature	K
\bar{u}	Mean velocity	m.s^{-1}
u	Velocity	m.s^{-1}
\bar{W}	Average molecular weight of the mixture	g/mol
W	Characteristic width	m
W_k	Molecular weight of the species k	g/mol
X_k	Mole fraction of species k	
Y_k	Mass fraction of species k	

Subscript

c	critical number
f	flame position
F	Fuel
O	Oxidizer
P	Products

Chapter 1

Introduction

The following experimental study deals with cellular instabilities in non-premixed flames. The term non-premixed refers to the way reactants are introduced into the combustor. In laminar flow, the fuel and oxidizer are initially separated and are brought to the reaction zone primarily due to molecular diffusion. This is in contrast to premixed flames where the fuel and the oxidizer are thoroughly mixed prior to reaching the reaction zone, also known as the flame front. Non-premixed flames form a high percentage of practical combustion problems. Although combustion will occur only where fuel and oxidizer meet, supplying them separately is convenient and safe. Diesel engines, gas turbines, most industrial burners, and coal combustion are just few examples of the many applications involving non-premixed combustion.

Instabilities in flames can have multiple origins. In general three ‘motors’ which drive the instability can be distinguished ranging from small-scale to large-scale phenomena. These are, in ascending order of size, combustion-driven, hydrodynamic-driven (Darrieus [18], Landau [61]) and buoyancy-driven (Taylor [106]) mechanisms. A comprehensive review of instabilities occurring in premixed flames can be found in Clavin [15] and in Buckmaster [7]. Cellular instabilities fall in to the category of combustion-driven mechanisms referred to in the following as reaction-diffusion problems.

1. INTRODUCTION

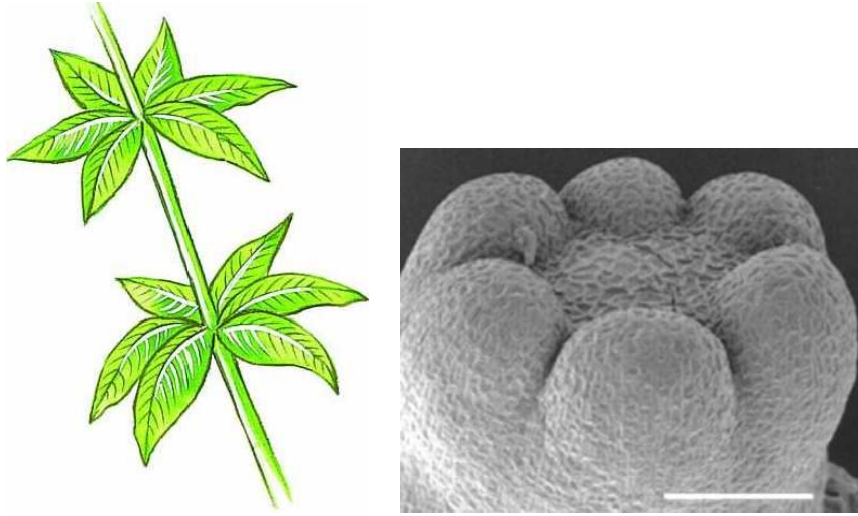


Figure 1.1: Typical examples of morphogenesis. The left sketch is of whorled leaves, e.g. an arrangement of several leaves radiating from a single node. The right figure is an SEM (Scanning Electron Microscope) image of developing somatic embryos showing 6 cotyledons taken from [37]. The scale bar is equal to 200 μm .

Reaction-diffusion model

Cellular patterns observed in reaction-diffusion problems are often related to the Turing instability. Although, as we shall see, the governing equations in combustion are different to those for reaction-diffusion, the Turing instability will be detailed here, since the underlying mechanism of this instability is instructive. Turing's work of interest here [90, 107] falls in the framework of the *morphogen theory of phyllotaxis* or *morphogenesis*. He suggested that this instability is at the origin of morphogenesis, like the formation of the freshwater polyp Hydra tentacles or whorled leaves. Figure 1.1 shows typical examples of morphogenesis in plants, such as the arrangement of several leaves radiating from a single node or developing somatic embryos showing 6 cotyledons equally spaced. Turing was influenced greatly by the biologist D'Arcy Thompson [17] who believed that biological forms were simply a result of chemical and physical processes. A common feature of biological development is a constant spacing between adjacent repetitions of an organ. Up to now, constant-spacing effects have been explained by reaction-diffusion

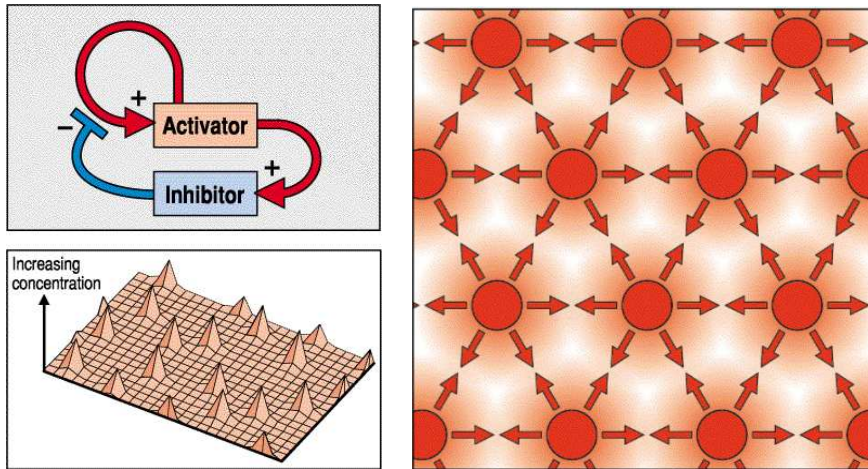


Figure 1.2: Left: Sketch illustrating the role of the different morphogens. Note that the inhibitor diffuses only on a short distance relative to the field size developing many evenly spaced peaks of activator. Right: This illustrates the activator peaks (circle) surrounded by diffuse halos of inhibitor. Taken from [115].

theory (in the phyllotaxis literature it is referred as the chemical theory). Turing suggested that a combination of chemical reactions and diffusion is adequate to account for the main phenomenon of morphogenesis, this theory being supported by contemporary biologists such as Wardlaw [109,110]. Turing assumed that pattern formation results if two interacting pattern-forming substances — the *morphogens* activator (A) and inhibitor (I) — diffusing at different rates in a third substance (the catalyst), satisfy particular diffusivity and reaction rate conditions. For example, suppose that cells have the capacity to autonomously produce a slowly diffusing activator (A). The activator (A) stimulates its own production (auto-catalysis) and also stimulates the production of inhibitor (I). (I) diffuses rapidly and inhibits the production of (A), thus creating a region of inhibitor surrounding an activator [72, 115]. Figure 1.2 illustrates the role of the different morphogens, taken from [115]. It should be noted that it has not been proven that these morphogens (activator or inhibitor) exist [1]. The wavelength of the pattern (Turing’s ‘chemical wavelength’ [107]) depends on the rates of reaction k and diffusion \mathcal{D} . Reaction rates give a characteristic time-scale $[k] = [\text{s}^{-1}]$ and diffusion gives proportionality between a characteristic distance and the

1. INTRODUCTION

time $[\mathcal{D}] = [\text{m}^2.\text{s}^{-1}]$. Reaction-diffusion equations are complex but generally lead to wavelength expressions that vary with the length scale $\sqrt{\mathcal{D}/k}$ (see Harrison [36]). Turing's predictions have been recently experimentally confirmed [11, 19, 81].

Some confusion prevails about what is meant by Turing structures. These structures are stationary concentration patterns, originating solely from the coupling of reaction and diffusion processes. They correspond to stable stationary solutions of a set of reaction-diffusion equations:

$$\frac{\partial c_i}{\partial t} = \mathcal{D}_i \Delta c_i + k \xi_i ,$$

where ξ_i are in general non-linear functions of c_i representing the contributions of reactive processes, and Δ the Laplacian operator. Thus, the characteristic 'chemical wavelength' is independent of the geometrical parameters. This separates the Turing patterns from other well known structures like the convective Bénard cells or the Taylor vortices in Couette flows [55]. Turing was not alone in arriving at these ideas. For the example detailed above and in Fig. 1.2, the function ξ could be a second order polynomial representing an autocatalyted reaction. For this particular form of ξ , similar ideas [44, 72] were introduced before Turing's 1953 work [107] by Kolmogorov, Petrovski and Piskunov [54], Fisher [25] and later by Rashevsky [88].

Cellular instabilities in combustion

Perhaps the earliest examples of cellular instabilities in flames are the observations made by Smithells and Ingle [100] in 1892, for premixed flames. The first analyses of these phenomena were made by Barenblatt, Zeldovich and Istratov [2] and suggested that the *thermo-diffusive* instability is similar to Turing's model, since it involves modification of the chemical reaction rate by differential diffusion of reactants and thermal energy as a reacting agent [68, 97]. However, the analysis of thermo-diffusive instability in flames is considerably more complicated than that of the bio-chemical model. The governing equations consist of the fluid mechanics equations (conservation of mass, conservation of momentum, and conservation of energy) supplemented by equations expressing the mass balance of the various species involved in

the chemical reaction. Therefore to a simple reaction-diffusion problem we add several layers of difficulties, namely advection and temperature dependence. Another complication comes from the fact that the reaction rate in combustion is strongly non-linear. Arrhenius showed that the relationship between temperature and the rate constant for a reaction obeys the following equation:

$$k = A \exp\left(\frac{-E_a}{RT}\right),$$

where k is the rate coefficient, A is a frequency factor, called the pre-exponential factor or the steric factor, and includes factors like the frequency of collision and their orientation and is often taken as constant, E_a is the activation energy, R is the universal gas constant, and T is the temperature. Molecules need sufficient energy above E_a for reaction to occur. For diffusion flames, the resulting flame temperature when plotted as a function of the Damköhler number¹, Dam , defined by the ratio of characteristic diffusion time and chemical time, gives an S-shaped curve defining three distinct regimes: a nearly frozen regime (weakly reacting) where the temperature increases due to chemical reactions up to the lower turning point, called static ignition point; an unstable partial burning regime where the reactants leak through the reaction zone near the upper turning point, called the static extinction point; and an intensely burning diffusion-controlled regime resulting in a very thin reaction zone (see Fig. 1.3). Several flame behaviors can be distinguished: for very large Damköhler number an infinitesimally thin reaction sheet exist as envisaged by Burke & Schumann [9], but for moderate values of Damköhler, combustion is incomplete and there is leakage of one or both reactants through the reaction zone [64].

The main research efforts on thermo-diffusive instability in flames have been directed towards premixed flames and examples which exploit the largeness of the activation energy parameter [8, 70, 71]. Since cellular instabilities can come from thermo-diffusive instabilities the Lewis number is of impor-

¹In the literature it is found that for the advection-reaction-diffusion problem, the Damköhler number is defined as the ratio between the advection time and the reaction time. Another number is then supplied for the ratio between the diffusion time and the reaction time, namely the Thiele modulus number (ϕ^2). However in the combustion community, the Thiele modulus is simply renamed as the second Damköhler number.

1. INTRODUCTION

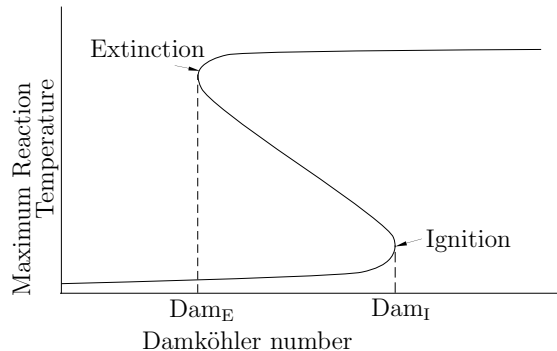


Figure 1.3: Typical variation of the maximum reaction temperature with the Damköhler number for a non-premixed mixture.

tance. The Lewis number (or Lewis–Semenov) is defined as the ratio between thermal diffusivity and mass diffusivity. By using activation energy asymptotics, the analysis of Sivashinsky [97] in adiabatic one-dimensional premixed flames showed that the cellular instability can occur if the mass diffusivity of the limiting reactant is sufficiently larger than the thermal diffusivity, i.e. the Lewis number is less than unity. Joulin and Clavin [45] extended the analysis to non-adiabatic premixed flames and showed that an oscillatory instability also occurs when the mass diffusivity of the limiting reactant is sufficiently small compared to the thermal diffusivity.

For diffusion flames, theoretical analysis is difficult due to the unmixed configuration. Instead of having a single term for the Lewis number (or other nondimensionalized numbers), we have to take into account both Lewis numbers, one for the fuel Le_F and one for the oxidizer Le_O . Nevertheless, a starting point for previous theoretical studies was to take equal Lewis numbers. Thermo-diffusive instability in diffusion flames was first investigated numerically for planar disturbances by Kirkby and Schmitz [53]. Later, Lewis number effects on diffusion flames were discussed for several burner configurations [14,51,101]. Kim, Williams and Ronney [52] theoretically investigated thermo-diffusive instabilities in a one-dimensional diffusion flame with equal Lewis numbers less than unity (for slowly varying flames, SVF) and for stoichiometric conditions. They focused on near extinction flames leading to a striped or cell pattern proportional to the reaction zone thickness. Their results predicted cellular instabilities for flames sufficiently close to quasi-

steady extinction. Kim [48] extended the analysis for a quasi-one-dimensional burner namely the opposed jet configuration. Kim [49] further investigated thermo-diffusive instabilities in diffusion flames with Lewis numbers close to unity (similar to the near equidiffusional flame, NEF, formulation). Kim [49] developed a general model and also considered the more general case where the Lewis number deviates from unity by a small amount and is defined for the deficient reactant. His results exhibited two types of unstable solution, depending on whether the Lewis number is less than or greater than unity. For sufficiently small Lewis numbers, a cellular instability arises. However, for flames with large Lewis numbers, a pulsating instability was found. The pulsating instability is beyond the scope of this document, and an exhaustive survey can be found in Fűri [26, 59]. The adopted configuration is the same as that of Kim *et al.* [52]. In this configuration, there is a constant velocity, directed from the porous oxidizer plate toward the porous fuel plate, and fuel and oxidizer diffuse from their respective supply plates to the reaction sheet where they react to release thermal energy. At each porous plate the concentration of the species supplied is maintained constant. Kim and Lee [50] and Lee and Kim [62] with the same method (NEF) focused on the counterflow configuration and found similarly oscillatory behavior for Lewis numbers higher than one and stripe patterns for Lewis numbers less than one. They pointed out that unlike the chaotic behavior of the cellular structure in premixed-flames [75, 97–99], coming from the integration of the Kuramoto–Sivashinsky equation, the strip structure is found to be stationary. These theoretical investigations indicated the importance of the Lewis number but did not study the importance of the initial mixture strength, ϕ (ϕ_m), defined as the fuel-to-oxygen molar (mass) ratio normalized by the stoichiometric value. Furthermore the instabilities presented are fast-time instabilities (growth rate scaled on the reaction time) which restricts the study very near extinction. The work of Cheatham and Matalon [12] addressed these last issues, and confirmed the importance of the Lewis numbers as well as the importance of the Damkőhler number, by conducting a general asymptotical theory for diffusion flames. Cheatham and Matalon [12] focused then on the onset of cellular instabilities for a one-dimensional burner, by providing stability curves that map the Lewis-number parameter plane

1. INTRODUCTION

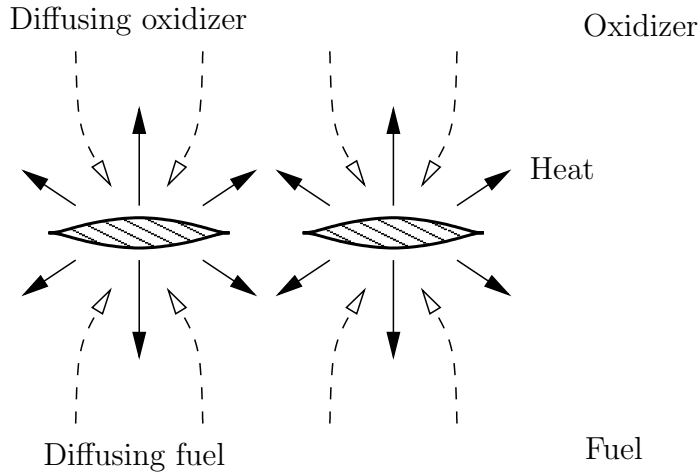


Figure 1.4: Schematic diagram of the thermo-diffusive instability of a diffusion flame. The hatched regions represent cells where heat release is reinforced by rising temperature. Mechanisms working against the instability: heat loss (solid arrows) and non-uniform diffusive reactant supply (dashed arrows).

for several values of ϕ_m . This one-dimensional burner is different from the one used by Kim *et al.* [52] and Kim [49]. This idealized burner was the same as Kirkby and Schmitz [53], first studied by Zeldovich [118], extending the work of Shvab [94]. This model allows the study of instabilities without any hydrodynamic disturbance, such as stretch (counterflow burner) or shear (jet burner), and will be the topic of Chap. 4-5.

The aim of this study is to elucidate the physics underlying cell formation for diffusion flames. The basic mechanism of these thermal-diffusive instabilities is relatively simple: if, within a part of the reaction zone, the temperature and the heat release perturbations are in phase, a mutual reinforcement of the two perturbations occurs, provided the reinforcement is not stopped by diffusion of heat or species and/or advective transport, see Fig. 1.4. For stationary cells in particular, the local temperature maxima associated with the maxima of reaction rate are local sinks for the reactants. These maxima are self-sustained provided that the thermal conductivity is low (small heat loss of the high temperature region) and the reactant diffusivities are high (small “resistance” to the non-uniform supply of reactants to the reaction rate maxima), i.e. provided the Lewis numbers are small (typically < 1). However,

the detailed analysis of the complete process is complex as it depends on a large number of parameters: the Damköhler number (Dam), the fuel and oxidizer Lewis numbers (Le_F , Le_O), the initial mixture strength (ϕ_m), and finally the standard hydrodynamic parameters must be included.

The first reported experiments on thermo-diffusive instabilities in diffusion flames are those of Garside and Jackson [29,30]. For a flame burning in air with a fuel mixture of hydrogen diluted in carbon dioxide, or nitrogen, they observed a polyhedral structure in an axisymmetric jet (AJ) burner. Later Dongworth and Melvin [22] reported cellular flames in a Wolfhard–Parker (WP) burner. They carried out experiments for hydrogen-oxygen flames and found cellular flames when the reactants were diluted with nitrogen or argon. However when the two reactants were diluted with helium, no cells were reported. Later Ishizuka and Tsuji [43] reported similar behavior in their counterflow diffusion burner for hydrogen flames. The burner was in fact a Tsuji burner, i.e. a porous cylinder immersed in a uniform stream. The experimental work of Chen, Mitchell and Ronney [13] reported the occurrence of cellular flames for various reactants in a WP burner. They clearly demonstrated the importance of low Lewis numbers on the formation of cells in diffusion flames. Fűri [26] pointed out the importance of the initial mixture strength, and conducted experiments in WP and AJ burners. He obtained cellular instabilities with SF_6 diluted methane burning in pure oxygen. For all these experiments, cellular instabilities were found near the extinction limit (associated with low Damköhler numbers) and for sufficiently low Lewis numbers, typically less than one.

None of the above experiments systematically investigated the influence of hydrodynamic forces or the influence of the initial mixture strength, on the onset and characteristics of the cellular instabilities. The observation of cells in these studies was in many cases of secondary importance [22, 29, 30, 43]. Chen *et al.* [13] performed a systematic study on the effect of Lewis number for a WP burner. Later, Fűri [26] reported the effect of initial mixture strength. Table 1.1 reports the typical wavelength of the cellular patterns observed in the works cited above involving different burner geometries. These previous experiments confirm the theoretical prediction for the Lewis dependence, e.g. the cellular regime occurs for relatively low Le_O but more

1. INTRODUCTION

Reference	Burner	Fuel	Inert	Le_F	Le_O	λ [cm]
Garside & Jackson [29, 30]	AJ	H ₂	CO ₂	0.27	1.13	0.7
Dongworth & Melvin [22]	WP	H ₂	N ₂	0.31	1.21	1.0
Ishizuka & Tsuji [43]	CF	H ₂	N ₂	0.30	1.20	0.7 ^a
Chen <i>et al.</i> [13]	WP	H ₂	N ₂	0.32	1.25	0.7–1.6 ^b
Füri [26]	AJ	CH ₄	SF ₆	0.50	0.50	0.4
Füri [26]	WP	CH ₄	SF ₆	0.50	0.50	0.32

^a taken from [52]

^b several exit velocities.

Table 1.1: Wavelength of cellular instabilities for various reactants and configurations.

importantly for low Le_F . Several wavelengths were found, ranging from 0.3 to 1.6 cm. These wavelengths were compared to theoretical prediction, but since these predictions were based on different geometries (often idealized) the comparison was only qualitative.

The dissertation will first introduce the experimental techniques and the jet burners used throughout this work in Chap. 2. Results will be described for cellular instabilities occurring in jet diffusion flames in Chap. 3. The influence of the initial mixture strength will be presented in Sec. 3.2, this first work [67] illustrates the effect of ϕ , in agreement with theory [12]. The influence of hydrodynamics and scaling issues will be described in Sec. 3.4. This first work on hydrodynamic effects will provide useful information for modeling and comparing results quantitatively with theories. Following this we shall investigate cellular instabilities in a burner without hydrodynamics effects, in Chap. 5 by constructing a novel one-dimensional unstrained burner depicted in Chap. 4. Finally a summary and concluding remarks will be given in Chap. 6.

Chapter 2

Jet diffusion flame facilities

2.1 Introduction

Jet test facilities are often used to study both reactive and non-reactive shear layers between gas or liquid streams. In this study two classical jet facilities are examined, namely the axisymmetrical jet (AJ) burner and the two-dimensional burner, referred as the Wolfhard–Parker (WP) jet burner. A novel burner was also studied and is presented in Chap. 4. Diffusion flame experiments consist of bringing fuel and oxidizer into a zone called the “mixing layer” in order to achieve the combustion process. Here the term mixing does not necessarily mean molecularly mixed, but a zone where both reactants can be found. These types of burners are present in various industrial devices: for example, coaxial jets constitute an efficient way of mixing species for combustion applications. They are also used for aeroacoustical purposes: the noise produced by a single jet can be damped with the addition of a surrounding coaxial stream [114]. Mixing in both non-reactive and reactive single-phases has been the subject of a number of experimental investigations into plane shear layers¹. These investigations typically focus on three main areas: the characterization of the mixing transition, the variation of the composition of the mixed fluid across the shear layer, and finally, the role of molecular diffusivity.

¹The streams can be either gas or liquid, which are characterized respectively by high and low molecular diffusivity.

2. JET DIFFUSION FLAME FACILITIES

In the high Damköhler² limit, e.g. when very fast kinetics characterize the chemical reaction, the reaction zone and the diffusive inter-penetration between the streams coincide [20, 79, 113, 117]. Therefore the geometry and the stirring conditions just after the contact play a crucial role.

In this chapter, several measurement techniques used throughout the dissertation are described in Sec. 2.2. Then, details on the flame test facilities are presented for the axisymmetrical jet (AJ) burner in Sec. 2.3.1 and for the Wolfhard–Parker (WP) burner in Sec. 2.3.2.

2.2 Measurement techniques

2.2.1 Properties of the fuel and oxidizers

The current investigation used hydrogen H_2 as the fuel mixed with various inerts and various O_2 -containing mixtures as the oxidant. The physical properties, e.g. thermal conductivities, diffusion coefficients, and thermal diffusion coefficients, were calculated with a software package developed at Sandia National Laboratories, CHEMKIN [46], coupled with a Perl script to automatically retrieve reactant properties at several conditions. This software provided both the mixture-averaged forms [47, 111] as well as the multicomponent formulations [21]. Basically, the code first computes third order polynomial fits of the physical properties versus the temperature. The properties are the dependent parts of the kinetic theory expressions for pure species viscosities and binary diffusion coefficients. Then a subroutine returns either pure species properties or multicomponent gas mixture properties. All the results given here come from the multicomponent formulation. The mixture-averaged calculation was not used because unlike the 1983 version [47] the binary diffusion computed in the mixture-averaged formulation does not use second-order correction [46]. The binary diffusion coefficients and the single component viscosities are given from the standard kinetic theory [39]. This expression is a function of the Lennard–Jones potential well depth, the dipole moment and the collision integral factor. The first two functions are read in

²Damköhler number Dam, is the ratio between the characteristic diffusion and the chemical reaction times.

2.2 Measurement techniques

an external database, and are available for numerous hydrocarbon combustion species in the correct format in [28] or from the NASA-Lewis data file. The collision integral value is determined by a quadratic interpolation of the tables based on Stockmayer potentials given in [76]. Appendix A presents the properties for the reactants used.

2.2.2 Flow controller system

Teledyne–Hastings® flow controllers (model HFC 202/203, “Low Flow”) were used to accurately control the flow rates of each gas. These instruments did not require any temperature correction and were insensitive to small upstream and downstream pressure changes. Separate flow controllers were used for each gas and application. The precision of these flow controllers was about 1% of full scale. Each flow controller had a shunt, which could be adapted to the desired flow range. The range of these flow controllers varied (for air equivalent) from 0–30, 0–10 and 0–3 sL/min, where sL/min represents liters per minute at standard conditions. The power supply was ± 15 VDC and both the driving and response signal were between 0–5 VDC. The input and output voltages to the mass flow controllers were regulated via two National Instrument data acquisition boards (PCI-6025E and PCI-6713). The PCI-6025E had a maximum sampling rate of 200 kS/s, an input range ± 0.05 to ± 10 V, a 12 bit input resolution and 16 analog inputs which could thus monitor up to 16 devices. The PCI-6713 had a sampling rate ranging from 740 kS/s to 1 MS/s, an input range from ± 0.05 to ± 10 V, a 12 bit output resolution and 8 analog outputs; it could thus control up to 8 input voltages from the flow controllers. Custom programs were written and developed with Labview® and allowed the user to make/check the calibration for the different gases and to simultaneously monitor all gas flows in the test facility. The program worked as follows: the total flow rate was set for each mixture (oxidizer and fuel) and desired the concentration of each mixture (in % vol.) was selected.

Calibration was made for each gas with a flow calibrator Bios® DryCal, DC-2. The Bios DryCal DC-2 primary flow meter uses near-frictionless piston and photo optic sensing technology to obtain volumetric and standard-

2. JET DIFFUSION FLAME FACILITIES

ized volumetric flow readings. Each calibration was made by averaging over a hundred measurements. Depending on the volumetric flow two flow cell ranges were used: a small one ranging from 10 to 1000 mL/min, and a large range from 1 to 50 L/min. The DryCal DC-2 uses internal sensors to automatically correct readings for standardized temperature and pressure conditions. Instantaneous readouts for the volumetric flow, volumetric flow average, standardized flow and standardized flow average were visible simultaneously on the LCD. A validation of flow calibrations was made prior to each series of experimental runs.

2.2.3 Traverse equipment

The axisymmetric jet burner (AJ) was vertically oriented and mounted on a precision two-dimensional traverse (Dantec® model 57G20). The precision of this traverse was $\pm 80 \mu\text{m}$. Some measurements required a greater precision (see Sec. 3.3.3). This system was completed with a more accurate two-dimensional traverse (Newport®) with a MM4006 motion controller. The precision stated by the manufacturer for the motion controller and the linear motor was $\pm 2 \mu\text{m}$. Unfortunately, unlike the Dantec® model, this traverse was designed with a side screw driven technology, which led to large errors ($\pm 0.5 \text{ mm}$). These errors were not acceptable so another feature was added: a high precision gauge (Sylvac® Mini dial gauge S233), which had a course length of 12.5 mm and a precision of $5 \mu\text{m}$. The gauge was supplied with the RS232 cable. The motion controller and the precision gauge were controlled with the RS232 port. A custom program was written and developed with Labview® and allowed the user to make a feedback control loop of the traverse system. With this system, the position was precise to within $5 \mu\text{m}$ with approximately three iteration steps.

2.2.4 Hotwire anemometer

Hotwire (HW) anemometry works on the basis of convective heat transfer from a heated thin wire to the surrounding fluid, the heat transfer being primarily related to the fluid velocity. The constant temperature technique (CTA) is the most used where the wire is placed in a bridge circuit which

2.2 Measurement techniques

keeps the wire resistance (temperature) constant. In this mode the current required to achieve constant temperature is a measure of fluid velocity normal to the wire.

The CTA measurements were performed using a Dantec® single hot wire, model 55 P11, and an anemometer TSI® model: IFA-100. The measurements were performed in a region where LDA measurements were not possible or for development/design purposes. These velocity profiles were measured in air, and calibrated with a dedicated calibrator with a low-turbulent free jet, whose velocity is calculated on basis of volumetric flow (see Sec. 2.2.2). The calibration curve was then fitted with a 4th order polynomial. These non-reacting velocity profiles in air were performed to measure the vorticity thickness (see Sec. 3.3.3) in the slot burner and to help design and develop a new 1-D burner (see Chap. 4. This technique (CTA) is not very accurate for small velocities (less than 10 cm.s^{-1}). A more suitable technique was used for small velocities, the constant current method. This method is similar to the CTA, fluid flow cools the thermistor thereby lowering its resistance and unbalancing the Wheatstone bridge and yielding a measurable voltage. The thermistor measurements were made using a device [38] borrowed from J.-A. Hertig from the Environmental Fluid Mechanics Laboratory, EPFL (EFLUM).

For a more comprehensive reference and review of the hotwire literature see [5, 6].

2.2.5 Laser Doppler anemometry (LDA)

Characteristics

Velocity measurements were performed using a three-component fiber-optic LDA system. A schematic view of the LDA measuring facility is shown in Fig. 2.1. Its components and their specifications are summarized below. For complete details see [24]. An Ar-Ion laser, Coherent Innova 90 was used. With this laser, an output of 10 W can be achieved. During the measurements the laser was run at about 2 W. This power provided sufficient intensity of the backscattered light of the particles. The optical head consists of two elements: the outgoing laser beam, which is split into two compo-

2. JET DIFFUSION FLAME FACILITIES

nents, and the backscatter sensor for detection of the scattered light. The two outgoing laser beams cross at a half-angle of 4.6° . At the intersection, the beams interfere and when a particle moving with the flow goes through the intersection, it scatters the light of the interfering laser beams with a frequency proportional to the velocity of the particle. This phenomenon is called Doppler frequency shift. The scattered light is detected by the optical head sensor and transmitted to a photo multiplier tube via fiber-optic cables. Three types of laser beams, distinguished by wavelength, i.e. by their color, were used for the experiments. The specifications of the three beams are given in Table 2.1.

Laser color		Blue	Green	Violet
Wavelength	[nm]	488.0	541.5	476.5
Calib.	[m.s ⁻¹ /MHz]	3.06	3.226	2.988
Beam distance d	[mm]	8	8	8
Focal length f	[mm]	50	50	50
Measurement volume				
Size Δx	[mm]	0.031	0.033	0.030
Size Δy	[mm]	0.031	0.033	0.030
Size Δz	[mm]	0.390	0.411	0.380
Volume	[10 ⁻⁴ mm ³]	2.0	2.3	1.8

Table 2.1: Specifications of the LDA apparatus. Calib. stands for calibration factor and is the conversion factor Doppler frequency-to-velocity. The spatial dimensions of the measurement volume are given by Δx , Δy , Δz .

The spatial resolution of the LDA (i.e. the measuring volume) obtained with this apparatus was between 0.18 and $0.23 \cdot 10^{-4} \text{ mm}^3$. The beam distance d is the distance between the split components of the laser at the lens. The optical signal received from the backscatter sensor in the optical head was amplified in a photomultiplier tube and processed by a burst spectrum analyzer, type Dantec® BSA model S, 57N10 and 57N25. The data acquisition was obtained with the Dantec® software BURSTware (1991), version 3.11. The Dantec® software was not used to perform the statistical calculations and to control the traverse — the BSA-computer and software are quite old and not supported by Dantec® anymore. It was not possible to change the BSA-computer because of compatibility problems with the burst spectrum

2.2 Measurement techniques

analyzers, giving rise to three issues: (1) extracting the binaries from the BSA-computer, (2) writing a code to process the binaries, and (3) managing the positioning of the optical head, controlled by the main computer, with the BSA computer. Installing the old-DOS network solved the first issue. The second issue was the easiest task and details are given in Sec. 3.3.3. The last issue was more difficult to solve. The BSA-computer displayed on the monitor a progress bar while acquiring the data. A Labview® code controlling a webcam (model: Typhoon Webshot II USB 300K Web Cam) focused on the progress bar and triggered the traverse system when necessary.

Seeding technique

In order to perform velocity profiles with the laser Doppler anemometry technique, it was necessary to appropriately seed the flow with particles. Since the size of the particles is a key parameter one must prevent agglomeration of the particles. It is always difficult to seed homogeneously a low mass flow rate of gas with solid particles. For very small velocities, $O(10 \text{ cm.s}^{-1})$, the best system was the use of a magnetic stirrer. This apparatus consists of a hermetically closed cylinder containing the seeding particles placed on a magnet agitator that actuates a metallic rod inside the cylinder. The particles are dispersed and the gas flow through the bin carries the particles along. For larger velocities a rotating disk technique showed the best results. This seeding system was larger than the first one and consisted of two joint metallic cylinders, the upper one containing the seeding particles. An electric motor is integrated in the lower cylinder and continuously turns a scratched disk. The gas flow is led between the upper and the lower cylinder where the seeding powder is continuously interspersed. For more details on the size specification for suitable particle tracers and a review of a wide variety of seeders see [73].

Seeding particles

The particles used in this work are Al_2O_3 particles (Micropolish® nominal diameter of $0.3 \text{ }\mu\text{m}$). Ideally seeding particles should have the following properties [24]: the same density as the fluid, ability to follow the flow, good

2. JET DIFFUSION FLAME FACILITIES

light scattering, non-toxic, non-corrosive, non-abrasive, non-volatile, or slow to evaporate, and chemically inactive.

An additional consideration, concerned with the motion of the particle relative to the fluid, is of importance when seeding particles are used as flow field tracers. Indeed, the motion of particles suspended in a fluid is affected by several interactions described by the two-phase flow theory. Some of the properties affecting the motion of the particle are the following: particle shape, particle size, relative density of particle and fluid, concentration of particles in the fluid, body forces, viscous drag, and electrostatic and thermophoretic forces.

More details on choosing the materials can be found in [24] (Sec. 10.5–10.8). The importance of added mass, history of acceleration and pressure gradient due to fluid accelerations has been determined for particle motion in turbulent fluid by Hjelmfelt *et al.* and was used to check if the particles followed well the fluid motion [40].

2.3 Description of facilities

2.3.1 Axisymmetric jet burner

P. A. Monkewitz and E. Pfizenmaier [78] designed the axisymmetrical jet (AJ) test facility to meet fluid mechanical and aeroacoustical conditions.

Figure 2.1 shows a sketch of the AJ burner with the LDA apparatus. The jet burner was vertically oriented and each gas (fuel, oxygen and inert) was individually connected to fully automated flow controllers (Sec. 2.2.2). The upstream pressure of the flow controllers was set with pressure regulators connected to the outlet of each gas cylinder. The fuel-inert mixture first passed through a seeder (Sec. 2.2.5) before entering a sound muffler where axial perturbations, coming essentially from the seeder and the flow controllers, were efficiently damped. The muffler was directly followed by a tube section, which contained a honeycomb flow straightener, and several turbulence screens followed by a contoured axisymmetric contraction with an area ratio of 100:1 from the settling chamber cross-section down to the round nozzle exit (inner diameter $D = 7.5$ mm). The hot gases were evacu-

2.3 Description of facilities

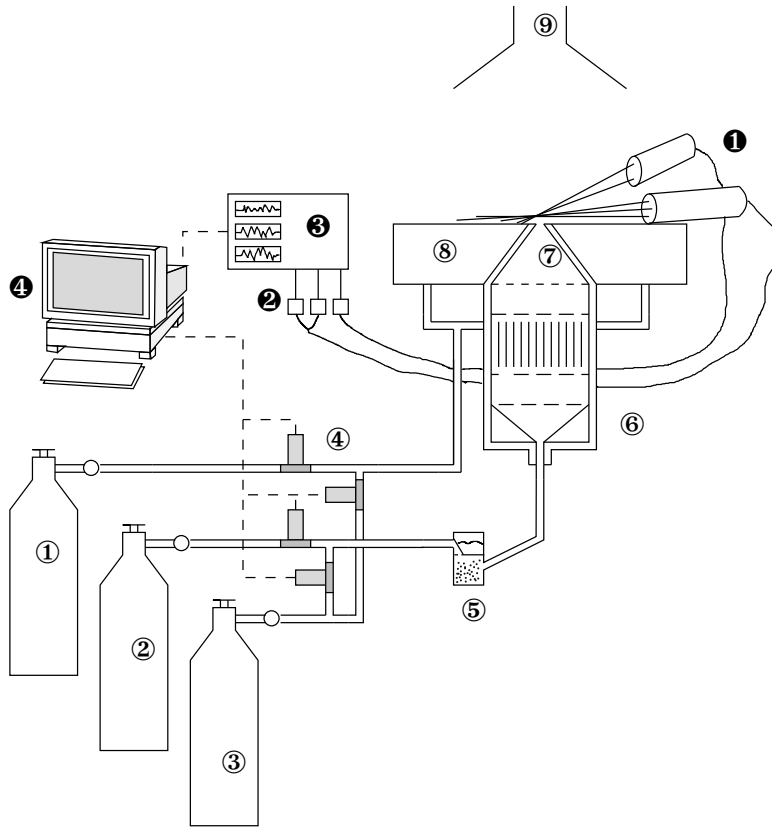


Figure 2.1: Schematic of the axisymmetric jet (AJ) burner and the LDA apparatus. Flow management: ① Oxidizer gas cylinder, ② Fuel gas cylinder, ③ Inert gas cylinder, ④ Flow controllers, ⑤ Particle seeder, ⑥ Turbulence management section, ⑦ Contoured nozzle 100:1, ⑧ Porous sintered metal sheet, ⑨ Exhaust system. LDA apparatus: ① LDA optical head, ② Photomultiplier Tubes (PMT), ③ Burst Spectrum Analyzer (BSA), ④ Data acquisition computer.

ated by the exhaust system of the laboratory. On the oxidizer side (co-flow) the oxygen-inert mixture were introduced through a porous sintered metal plate (Mott Metallurgical, 100 μ grade) of 75 mm diameter that surrounded the fuel jet nozzle. This porous plate ensured a high pressure drop. The co-flow velocity profile at the exit was shown to be uniform (HW measurements located at 0.5 mm above the jet nozzle [26]). The diameter chosen was large enough to avoid any disturbance due to external flow. However, there were two major drawbacks in the design of the co-flow. Firstly, the porous plated

2. JET DIFFUSION FLAME FACILITIES

precluded any non-intrusive measurements such as LDA. Since, the co-flow could not be seeded a bias was introduced in the LDA measurements of the velocity in the shear layer. Note that this bias did not play a significant role for the measurement of the *initial* vorticity thickness [24, 26]. Secondly the co-flow diameter prevented a high flow of oxidizer ($U_{\text{co-flow}} \approx 14 \text{ cm.s}^{-1}$ for 30 L/min at standard conditions) because of the limited maximum range of the flow controllers.

2.3.2 Wolfhard–Parker burner

The Wolfhard–Parker burner (WP), or slot burner, is a two-dimensional burner. A schematic view and the dimensions of the burner are shown in Fig. 2.2. The fuel jet in this burner has a large 7:1 aspect ratio (ratio of length to width) in order to minimize the end effects. The burner designed and constructed by Fűri [26] was modified here in order to have better flow uniformity at the exit. The fuel and oxidizer are introduced from the bottom section of the burner, passing a first diffusor of perforated sheet metal before passing through four metal grids. The brass metal grids had a wire thickness of 0.35 mm; the mesh spacing was 0.5 mm. The geometrical dimensions of the fuel outlet were $l = 56 \text{ mm}$ for the length and $W = 8 \text{ mm}$ for the width. For this burner, post-combustion gases are also evacuated by the exhaust system of the laboratory. The results of these modifications are a uniform and symmetric top hat profile at the exit, see Sec. 2.3.2.

2.3 Description of facilities

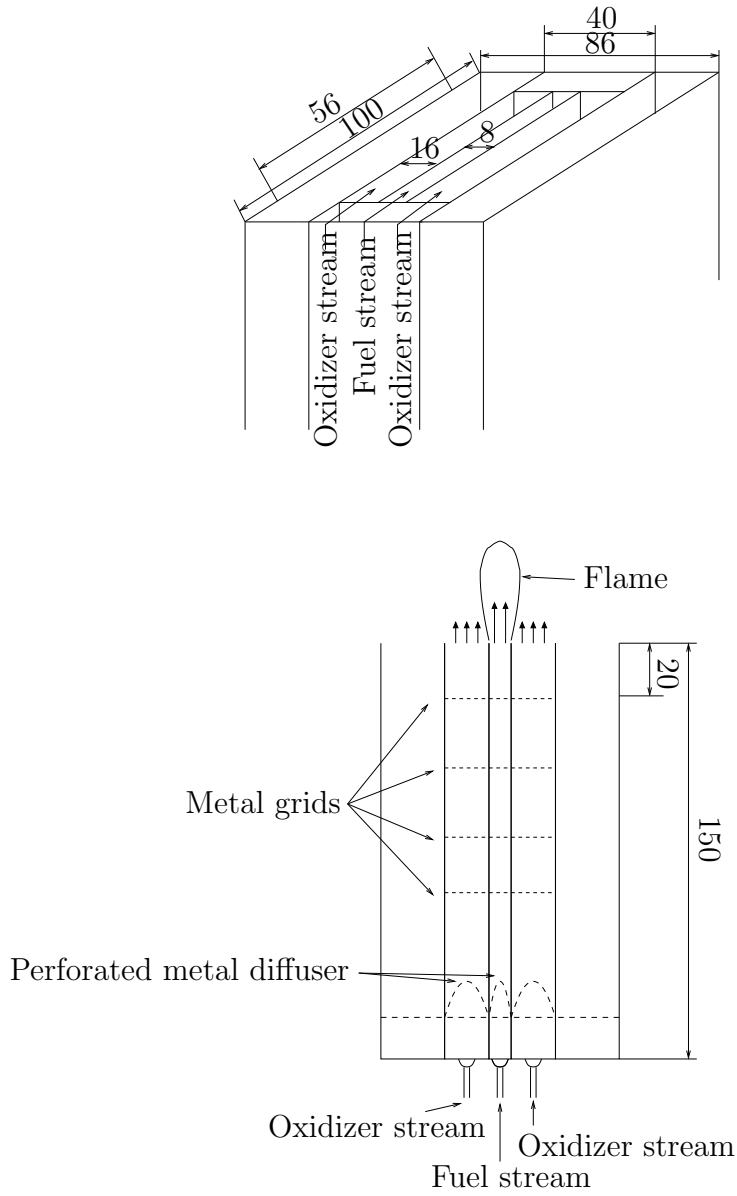


Figure 2.2: Schematic view of the Wolfhard–Parker burner. Dimensions are given in mm.

2. JET DIFFUSION FLAME FACILITIES

Chapter 3

Cellular instabilities in jet diffusion flames

3.1 Introduction

This chapter is concerned with the cellular instabilities occurring in jet diffusion flames for several parameters. Few experimental observations have reported cellular instabilities of diffusion flames [13, 22, 26, 29, 30, 43]. None of them performed a systematic investigation on flame diffusion instabilities. Several theoretical studies were undertaken for idealized burner in diffusion flames [12, 52]. These studies are likely to compare their model to experience by comparing wavelength associated to the maximal growth rate at marginal stability.

The first section (Sec. 3.2), will introduce the first systematic experimental work study on $\text{H}_2\text{-O}_2$ diluted with CO_2 diffusion flames in an axisymmetric jet near-extinction. This work will cover a wide range of initial mixture fraction, and will show clearly the crucial role of this initial mixture fraction, ϕ -space parameter, on the occurrence of cellular instabilities. The second space parameter studied is the fuel velocity exit for a fixed initial concentration. This study involves the formation of coherent structures linking hydrodynamic and combustion instabilities. The jet flow properties at the nozzle exit are mainly imposed by the upstream geometrical properties such as the shape of the contoured nozzle or different flow straighteners. The ratio

3. CELLULAR INSTABILITIES IN JET DIFFUSION FLAMES

between the nozzle radius and the momentum thickness of the shear layer at the jet nozzle exit (vorticity thickness) plays a significant role in the jet behavior [16,41,74,77]. Characteristics on the velocity profiles and vorticity thickness are presented in Sec. 3.3. The results of these characteristics on the cellular formation in jet diffusion flames are then presented for this space parameter in Sec. 3.4.

3.2 Effect of reactant composition on cellular instabilities

Combust. Theory and Modelling, **7**, 2003 [67]

This experimental work will introduce the first systematic study of cellular instabilities of H₂-O₂ diluted with CO₂ diffusion flames in an axisymmetric jet. Past theoretical work [12] demonstrated the importance of the mixture strength, in addition to Lewis numbers, on the formation of cellular instabilities, thus this experimental study, and will show clearly the crucial role of this mixture fraction on the occurrence of cellular instabilities. This first study was published at the *Combustion Theory and Modelling* [67]. For consistency purposes minor modification were made to the original paper such as figures positions in text and figures and table numbers. The references to other publications correspond to references in the general bibliography.

Cell formation in non-premixed, axisymmetric jet flames near extinction

Abstract

Systematic experiments with CO₂ diluted H₂-O₂ circular jet diffusion flames have been undertaken to study the formation of cellular flames, which occur for relatively low reactant Lewis numbers and near the extinction limit. The jet Reynolds number for all experiments was about 500 based on the center-line velocity, jet diameter and ambient fuel properties. The Lewis numbers, based on the initial mixture strength ϕ and ambient conditions, of the investigated near-extinction mixtures vary in the range [1.1–1.3] for oxygen and [0.25–0.29] for hydrogen (ϕ is defined here as the fuel-to-oxygen molar ratio normalized by the stoichiometric value). Various conditions near the extinction limit were investigated by fixing the fuel composition (H₂-CO₂ mixture), and systematically lowering the oxygen concentration in the co-flowing oxidizer stream past the point where cellular structures formed, until extinction occurred. The observed different instability states were correlated with the initial mixture strength and the proximity to the extinction limit.

The parameter space for cellularity was found to increase with decreasing initial mixture strength. For a given initial mixture strength, several cellular states were found to co-exist near the extinction limit, and the preferred number of cells (the azimuthal wave number) was observed to decrease with decreasing oxygen concentration (Damköhler number). These trends are consistent with previous theoretical work and our own stability analysis to be reported elsewhere.

3.2.1 Introduction

Experimental studies on the formation of cells in premixed circular burners have revealed that a wide variety of spatio-temporal patterns. For premixed jet flames, these states include uniformly rotating ring(s) of cells [34], nonuniform or intermittent rotations [34], and ratcheting or chaotic motions [33].

3. CELLULAR INSTABILITIES IN JET DIFFUSION FLAMES

The formation of cellular structures in premixed flames is attributed to thermo-diffusive instabilities which occur when a weighted Lewis number is sufficiently low [15], and simple phenomenological models have been developed to replicate the particular cellular patterns [82].

Although the first observations of cellular instabilities in non-premixed flames date back many decades [22,29], theoretical analyses of thermo-diffusive instabilities in non-premixed flames are quite recent [12, 49, 59, 83, 84]. The stability analysis performed by Matalon and Cheatham [12] demonstrated that both reactant Lewis numbers are important for non-premixed flames, and the propensity for the formation of cells increases with decreasing reactant Lewis numbers, Damköhler number, and initial mixture strength or 'equivalence ratio.' In this study, the initial mixture strength ϕ , which can be specified for purely gaseous non-premixed flames, is defined as the fuel-to-oxygen molar ratio normalized by the stoichiometric ratio. The experimental investigation of Chen *et al.* [13] clearly demonstrated the importance of relatively low Lewis and Damköhler numbers for the formation of cells in non-premixed flames. Little attention has been given, however, to the selection criteria of cellular patterns— in particular, to the influence of the initial mixture strength ϕ and the dynamics of these cellular patterns. More recent work in our laboratory has demonstrated the importance of the initial mixture strength on gaseous non-premixed flame instabilities [26, 27]. Figure 3.1 shows the formation of a cellular $\text{CH}_4\text{-SF}_6$ jet flame burning in pure oxygen [26]. The low luminosity from diluted hydrogen flames makes photography difficult; thus, Fig. 3.1 was chosen because it represents a clearer visualization, while still reproducing all the qualitative features of the cellular $\text{H}_2\text{-O}_2$ flames considered in this paper. In Fig. 3.1, the reactant Lewis numbers of both methane and oxygen are about 0.5 based on the overall mixture ($\phi = 0.42$) at ambient conditions. Other experiments at higher initial mixture strengths for both SF_6 -diluted methane- and propane-oxygen flames indicated that cell formation could be suppressed by increasing initial mixture strength, despite the relatively low reactant Lewis numbers of these systems.

Since the number of physical effects (and parameters) potentially involved in cell formation is large, experimental information is required to elucidate

3.2 Effect of reactant composition on cellular instabilities

Combust. Theory and Modelling, 7, 2003 [67]

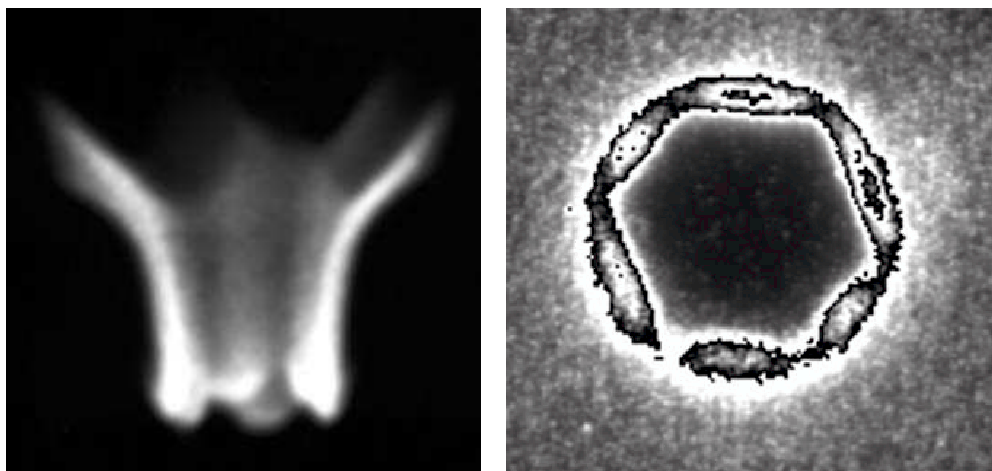


Figure 3.1: Hexagonal cellular flame instability of an axisymmetric methane jet diffusion flame (taken from [26]). 21% CH_4 -79% SF_6 fuel mixture burning in 100% O_2 . Left: side view (photograph); Right: axial view (streamwise integrated chemiluminescence image taken from the downstream jet axis).

the underlying physics. Such information is still largely incomplete, particularly regarding the dynamics and types of cellular patterns which develop in non-premixed flames (e.g. the preferred number of cells in a particular system) and the parameter space (e.g. the range of initial mixture strengths) in which different cell patterns appear. This relative lack of experimental data has provided the motivation for the current investigation.

3.2.2 Experimental description

Only a brief overview is given here, since a detailed description of the EPFL facility can be found elsewhere [26]. The flame test facility consists of a free jet rig, oriented vertically up and mounted on a precision traverse, of a laser Doppler anemometer (LDA) and a setup for laser-induced fluorescence (LIF), together with PC-based data acquisition and control systems. An intensified CCD (LaVision, Flamestar II) with 384×576 pixels and 14-bit resolution was used to record images of the streamwise integrated chemiluminescence emission from above the flame tip. The flow rates of the fuel, inert and oxygen gases to the jet apparatus were set with fully automated flow con-

3. CELLULAR INSTABILITIES IN JET DIFFUSION FLAMES

trollers (Teledyne-Hastings, HFC 202/203) that had a nominal accuracy of 1% (Full Scale). Flow rate calibrations were verified with a flow calibrator (Bios, DC-2M). The gaseous fuel passed through a muffler, settling chamber with honeycomb straighteners and turbulence screens, and finally through a contoured axisymmetric contraction with an area ratio of 100:1. The diameter of the circular fuel nozzle is $D = 7.5$ mm. In order to control the oxidizer characteristics, a uniform co-flow of an oxygen-inert mixture could be introduced through a porous plate of 75 mm diameter which surrounds the fuel nozzle.

3.2.3 Experimental results

For the experiments reported in this study, the fuel centerline and co-flowing oxidizer velocities (flow rates) were fixed at $U_F \approx 76$ and $U_O \approx 4$ cm.s⁻¹, respectively. The corresponding jet Reynolds number, based on U_F , the jet diameter and fuel properties at 300 K, is about 500. The parameter space near the extinction limit was investigated by fixing the fuel composition (H₂-CO₂ mixture) and systematically lowering the concentration of O₂ in the oxidizer stream (O₂-CO₂ mixture) until extinction was reached. Specifically, experiments were performed for thirteen different hydrogen concentrations in the range of 17-35% hydrogen by volume, which are indicated by arrowheads next to the ordinate of Fig. 3.2. For each of these thirteen fuel compositions, the oxygen concentration was decreased in steps of 0.1%. In terms of reactant Lewis numbers, based on the overall reactant mixture at 300 K, these near extinction experiments cover the range of [1.1–1.2] for oxygen and [0.25–0.28] for the hydrogen fuel. In terms of initial mixture strength, the experiments mostly cover the region $\phi \lesssim 1$. The two dotted straight lines through the origin of Fig. 3.2 are lines of constant ϕ . The line $\phi = 1$ then divides the figure into a part on the left with overall “fuel-rich” mixtures and a part on the right with “fuel-lean” mixtures.

Within this parameter space, the different flame regimes, e.g. the type of cellular structures, were recorded and the dynamic extinction limit, shown as thick solid line in Fig. 3.2, was determined *for the flow conditions of the current experiments*. Regardless of the concentration of the other reactant,

3.2 Effect of reactant composition on cellular instabilities

Combust. Theory and Modelling, 7, 2003 [67]

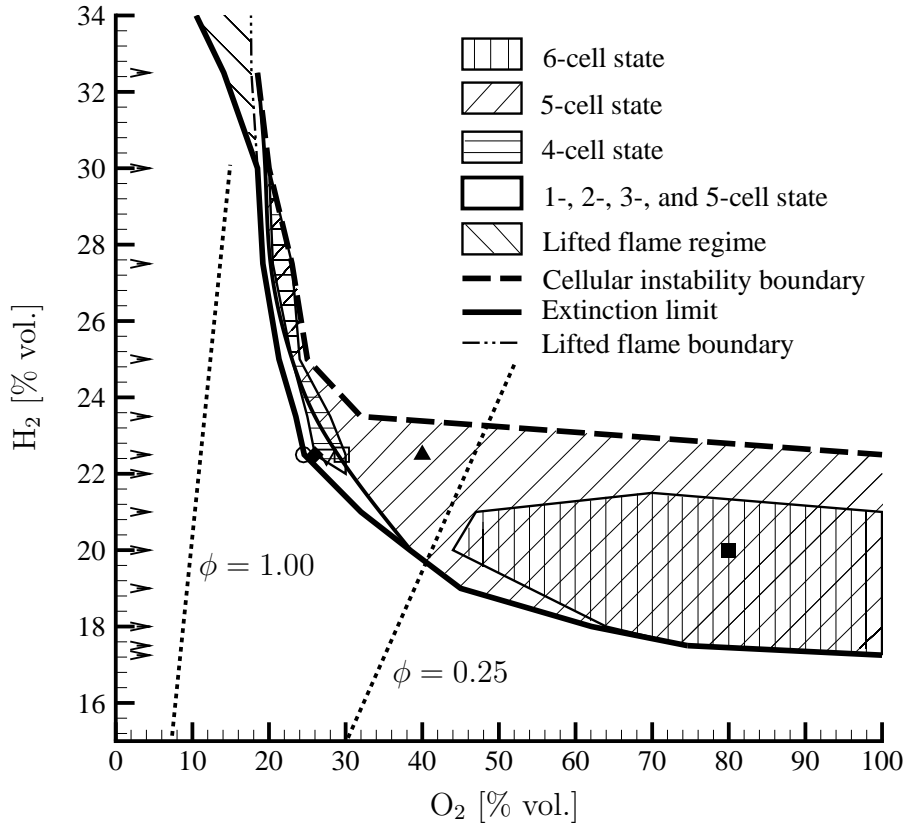


Figure 3.2: Extinction limit and boundaries of different cellular instabilities observed for CO_2 diluted, $\text{H}_2\text{-O}_2$ jet diffusion flames. Centerline fuel velocity $U_F \approx 76 \text{ cm.s}^{-1}$. Oxidizer co-flow velocity $U_O \approx 4 \text{ cm.s}^{-1}$. [O]: Rotating single-cell state of Fig. 3.3(a); [D]: rotating 2-cell state of Fig. 3.3(b); [V]: rotating 3-cell state of Fig. 3.3(d); [Q]: 4-cell state of Fig. 3.3(d); [P]: 5-cell state of Fig. 3.3(e); and [■]: 6-cell state of Fig. 3.3(f).

this extinction curve reveals that a diffusion flame could not be established below the asymptotic (limiting) hydrogen concentration of about 17.3%, or approximately a limiting oxygen concentration of about 18% by volume. It is noted that above a hydrogen concentration of about 30% (and $\phi \gtrsim 1$), lifted flames are observed below an oxygen concentration of 18% ; thus, the above limiting oxygen concentration is not a real asymptote. The anchoring

3. CELLULAR INSTABILITIES IN JET DIFFUSION FLAMES

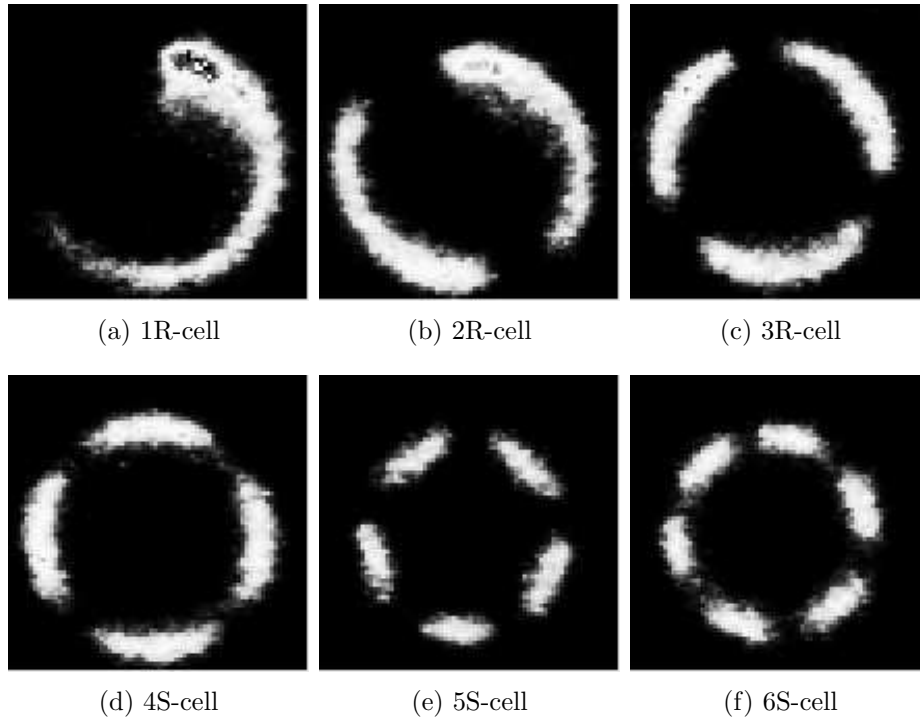


Figure 3.3: Streamwise integrated chemiluminescence images taken from the downstream jet axis of a 22.5% H_2 (77.5% CO_2) jet flame burning in (a) 24.6% O_2 (75.4% CO_2) co-flow; (b) 26.0% O_2 co-flow; (c) 27.5% O_2 co-flow; (d) 31.0% O_2 co-flow, (e) 40.0% O_2 co-flow, and (f) 20.0% H_2 (80.0% CO_2) jet flame burning in 80.0% O_2 co-flow. “R” designates rotating and “S” stationary cell patterns. Fuel and oxidizer velocities as in Fig. 3.2.

edges of these flames, which were lifted above the jet nozzle rim, were found to meander in the downstream direction, but regular flame-edge oscillations [26,27] were not observed for the conditions explored. Since it is not the focus of the current study, this lifted flame regime will not be further discussed.

Additional tests were performed to ensure that the measurements of the extinction limit are not compromised by air entrainment into the oxidizer co-flow, especially for O_2 concentrations below the 21% concentration in air, i.e. H_2 concentrations in Fig. 3.2 above about 25%. In this parameter region, an air entrainment would cause a nominally lower oxygen concentration at

3.2 Effect of reactant composition on cellular instabilities

Combust. Theory and Modelling, 7, 2003 [67]

extinction because of the differences in the inert¹ specific heat values of CO₂ and N₂, and the higher oxygen concentration in air. The tests consisted of preventing air entrainment by completely surrounding the co-flow with a quartz cylinder of 20 cm diameter and 50 cm length. The resulting extinction limit was found to be identical to the one determined without a quartz cylinder, and reported in Fig. 3.2 for the entire non-lifted regime of interest here.

The various types of cellular modes shown in Fig. 3.2 are illustrated by the images of Fig. 3.3 obtained at a fixed jet fuel composition (22.5% H₂, except for the last image (f) obtained with 20.0% H₂) and various oxygen concentrations above the extinction limit of 23.2% O₂. The images, labeled Fig. 3.3(a)–3.3(f), correspond to the six individual symbols in Fig. 3.2. These images were taken with a digital camera (71 × 74 pixel images) pointed at the flame from the downstream jet axis. The gray-scale is related to the intensity of the chemiluminescence, integrated in the streamwise direction over the entire length of the flame. All the images shown here are of flames typified by Fig. 3.1: a distinctively cellular flame structure which varies little in the streamwise direction and a total flame length of less than three jet diameters. Following the terminology of other investigators [34], the particular cellular states in this Fig. 3.3 are labeled by the number of cells, followed by the letters “R” or “S” for rotating and stationary states, respectively. The lower-numbered cellular structures (3R, 2R, and 1R states) rotated around the jet axis in either the clockwise or counterclockwise direction, depending on the initial conditions.

The observed cellular states result from a sequence of transitions which occur within a narrow range of parameters (oxygen concentration in this example). Since different states have been observed to compete near the extinction limit, the state realized in a particular experiment is determined by the initial conditions and the path adopted in parameter space to reach the experimental conditions (for instance, the way the O₂ concentration is changed). Consequently, mode switches can be also induced by suitable (possibly large) perturbations such as noise, transient perturbations of the

¹Carbon dioxide is essentially chemically inert under the current experimental conditions.

3. CELLULAR INSTABILITIES IN JET DIFFUSION FLAMES

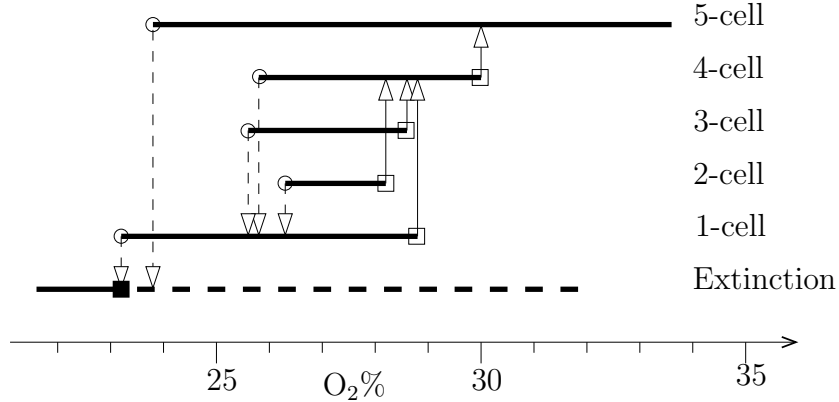


Figure 3.4: Forward- and backward-transition oxygen values observed for 22.5% H₂-77.5% CO₂ jet diffusion flames burning in O₂-CO₂. Fuel and oxidizer velocities as in Fig. 3.2. [■]: Dynamic extinction limit. [- - -]: No extinction observed for unperturbed flames. [○]: Backward-transition points. [□]: Forward-transition points.

jet flow field or the fuel flow rate, etc. As a consequence, the regions in Fig. 3.1 with different numbers of cells are overlapping and indicate where such a state *can* be produced in an ensemble of attempts with different initial conditions and/or perturbations. Except very near extinction, the most commonly encountered cellular state in our experiments at relatively high oxygen concentrations (‘fuel-lean’ conditions) were 5 or, with smaller probability, 6 stationary cells shown in Fig. 3.3(e) and 3.3(f), respectively. At lower oxygen concentrations (‘fuel-rich’ conditions), the 6-cell mode was no longer observed, but the flame could be forced to switch from the preferred 5-cell mode to the stationary 4-cell mode of Fig. 3.3(d). The (overlapping) parameter regions, in which these 4- to 6-cell states can appear, are shown in Fig. 3.2.

Close to extinction, a sequence of transitions could be induced between the 5-cell state, which dominates further away from the extinction boundary, and the 4-, 3-, 2-, and single-cell states. Figure 3.4 shows a transition diagram between the states shown in Fig. 3.3(a)–3.3(e) for the fixed fuel concentration of 22.5% H₂ (the line of symbols in Fig. 3.2) and the fixed reactant stream velocities used throughout the study. For this fuel composition, only the stationary 5-cell state illustrated in Fig. 3.3(e) was observed above 30% O₂

3.2 Effect of reactant composition on cellular instabilities

Combust. Theory and Modelling, 7, 2003 [67]

concentration and no flame could be sustained below 23.2% O₂ concentration, the extinction limit. Between these concentrations, (hysteretic) transitions could be induced either by gradually changing the O₂ concentration in small steps of 0.1% or by “inducing” the system with a large perturbation (actually a screwdriver). In Fig. 3.4 all the so-called “forward-transition” and “backward-transition” points resulting from a gradual increase or decrease in the O₂ concentration, respectively, are indicated by arrows. Starting with the 5-cell state, for instance, a gradual decrease of the oxygen concentration in the oxidizer stream leads directly to extinction at about 23.8% O₂ concentration². The corresponding inverse transition from extinction to the 5-cell state is of course not defined, as it involves the intervention of an ignition source. Consequently, the broken line on Fig. 3.4, labeled “no extinction observed for unperturbed flames,” simply indicates the O₂ concentrations for which the current flames could possibly be extinguished with perturbations.

From the direction of the arrows in Fig. 3.4, it is immediately clear that the 1- to 4-cell states *cannot* be reached from the 5-cell state by slow variations of the O₂ concentration in the oxidizer stream. Hence, they were all produced by large initial perturbations (insertion of a screwdriver into the flame in a manner promoting the desired symmetry, or possibly upon ignition). The interval of O₂ concentrations over which our “screwdriver perturbation” was effective, is indicated by the solid lines associated with the 1- to 4-cell states in Fig. 3.4. Once one of these states was “induced” into existence, the O₂ concentration was again slowly varied to locate the forward and backward transitions to other modes. Since this procedure to locate the transition points is clearly independent of the initial perturbation, the observed “intervals of existence” of the 1- to 4-cell modes are believed to correctly represent the stability boundaries of these (saturated) modes. These stability intervals were furthermore tested by repetitive perturbations (typically more than 50 attempts) at each fuel/oxidizer composition investigated. The O₂ concentrations for the forward- and backward-transition points obtained in this manner were repeatable to within 0.3% vol.

Within a narrow range of O₂ concentrations around 27%, all states from 1 to 5 cells are possible. This range corresponds to the white region in Fig. 3.2,

²5-to-1 transitions could be observed at higher hydrogen concentrations.

3. CELLULAR INSTABILITIES IN JET DIFFUSION FLAMES

just prior to extinction, where the 3R, 2R, and 1R states can all be excited. Since the preferred state in this region is a rotating single-cell (1R) state, transitions from high-numbered cellular states such as the 4-, 3-, and 2-cell states typically go directly to the rotating single-cell state. Even closer to extinction in Fig. 3.4, only the 5-cell and the 1-cell state can be observed, and it is interesting that the flame in the 1-cell mode can persist longer (down to 23.2% O₂) than the 5-cell flame which extinguishes at 23.8% O₂³.

3.2.4 Discussion and conclusions

For a given fuel composition, examination of Fig. 3.2 shows that the likelihood of observing a low-number cellular state increases with decreasing oxygen concentration. Since the Damköhler number and initial mixture strength vary with changing oxygen concentration, it is important to examine the data in the entire fuel-oxygen parameter space. Figure 3.2 shows that the rotating single-cell state can only be observed at relatively large initial mixture strengths near the extinction limit. Also, Fig. 3.2 shows that the propensity for the rotating single-cell flame state increases with decreasing oxygen concentration or Damköhler number (i.e. nearer the dynamic extinction limit). The trend with initial mixture strength is consistent with recent theoretical work in our laboratory consisting of a viscous, finite-rate linear stability analysis of a non-premixed circular jet flame [87]. Also, recent numerical simulations of two-dimensional counterflow diffusion flames have shown that transitions from states with narrow “stripes” (cells) to wider “stripes” occur as the Damköhler number is reduced [63].

Table 3.1 summarizes the conditions at which cellular instabilities have been observed in the current study and previous investigators. The first and second columns identify the fuel system and inert, respectively. The third and fourth columns report the fuel and oxygen Lewis number, respectively, calculated for the overall mixture (fuel/inert as well as the oxygen/inert mixtures) [46]. The fifth and sixth columns report the initial mixture strength ϕ , based on the molar fuel-to-oxygen concentrations in the fuel and oxidizer

³Note that the extinction value reported in Fig. 3.2 corresponds to the extinction of the 1-cell flame.

3.2 Effect of reactant composition on cellular instabilities

Combust. Theory and Modelling, 7, 2003 [67]

Fuel	Inert	Le _F	Le _O	ϕ	ϕ_m	X_F	X_O	Obs.	Config.
H ₂	CO ₂	0.25	1.06	0.117	0.112	0.175	0.746	C	AJ
H ₂	CO ₂	0.24	1.04	0.145	0.145	0.180	0.621	C	AJ
H ₂	CO ₂	0.24	1.03	0.211	0.226	0.190	0.450	C	AJ
H ₂	CO ₂	0.24	1.03	0.260	0.288	0.200	0.384	C	AJ
H ₂	CO ₂	0.24	1.03	0.328	0.375	0.210	0.320	C	AJ
H ₂	CO ₂	0.24	1.04	0.457	0.543	0.225	0.246	C	AJ
H ₂	CO ₂	0.24	1.05	0.500	0.603	0.235	0.235	C	AJ
H ₂	CO ₂	0.24	1.06	0.587	0.726	0.250	0.213	C	AJ
H ₂	CO ₂	0.25	1.09	0.716	0.920	0.275	0.192	C	AJ
H ₂	CO ₂	0.25	1.12	0.811	1.079	0.300	0.185	C	AJ
H ₂	CO ₂	0.26	1.15	0.918	1.266	0.325	0.177	NC	AJ
H ₂	CO ₂ /N ₂	0.27	1.13	0.461	0.370	0.194	0.210	C	AJ ^a
H ₂	N ₂	0.31	1.21	0.274	0.316	0.115	0.210	C	WP ^b
H ₂	Ar/N ₂	0.30	1.20	0.255	0.205	0.107	0.210	C	WP ^b
H ₂	N ₂	0.31	1.21	0.271	0.313	0.114	0.210	C	CF ^c
H ₂	Ar	0.29	1.18	0.193	0.200	0.081	0.210	C	CF ^c
H ₂	He	0.92	3.20	0.283	0.743	0.119	0.210	NC	CF ^c
H ₂	N ₂	0.31	1.22	0.250	0.294	0.128	0.256	C	WP ^d
H ₂	N ₂	0.32	1.25	0.500	0.599	0.158	0.158	C	WP ^d
H ₂	N ₂	0.33	1.29	1.000	1.250	0.203	0.102	C	WP ^d
H ₂	N ₂	0.34	1.33	1.500	1.961	0.244	0.081	C	WP ^d
H ₂	N ₂	0.35	1.40	2.000	2.857	0.315	0.079	NC	WP ^d
CH ₄	SF ₆	0.50	0.50	0.420	0.113	0.210	1.000	C	AJ ^e
CH ₄	SF ₆	0.47	0.48	0.477	0.184	0.210	0.880	C	AJ ^e
CH ₄	SF ₆	0.52	0.52	0.560	0.163	0.280	1.000	C	WP ^e
C ₃ H ₈	SF ₆	0.92	0.45	1.358	0.590	0.220	0.810	NC	AJ ^e

^aGarside and Jackson [29].

^bDongworth and Melvin [22].

^cIshizuka and Tsuji [43].

^dChen *et al.* [13].

^eFüri [26].

Table 3.1: Characteristic parameters for various flames near extinction. AJ denotes axisymmetric jet burners, WF denotes Wolfhard–Parker jet burners, and CF denotes counter-flow burner.

streams, and the mass-based initial mixture strength ϕ_m . This mass-based ratio equals the ratio of the fuel mass fraction in the fuel stream to oxygen mass fraction in the oxidizer stream normalized by the stoichiometric fuel-to-oxygen mass ratio. Both parameters completely identify both the fuel/inert and oxygen/inert stream compositions. The ninth column indicates if cellular instabilities, denoted by “C,” or non-cellular flames, denoted by “NC,” were observed. Finally, the last column relates the type of experimental apparatus used as well as the reference citation.

The propensity of diffusion flames to form cellular instabilities with de-

3. CELLULAR INSTABILITIES IN JET DIFFUSION FLAMES

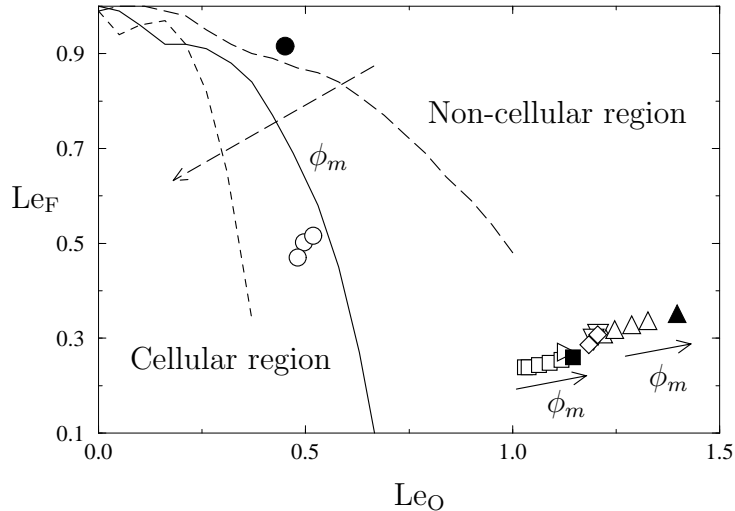


Figure 3.5: Theoretical cellular instability boundaries (lines) for an ideal unstretched planar flame and experimental jet flame data near extinction in the Le_F - Le_O plane. Open and solid symbols correspond to cellular and non-cellular flames, respectively. Theoretical calculation taken from [12] for $\phi_m = 1/3$ [---]; $\phi_m = 1$ [—]; $\phi_m = 2$ [- - -]. Experimental data: [□]: CO₂ diluted H₂ cellular axisymmetric jet flames (AJ) burning in CO₂-O₂ co-flow; [△]: N₂ diluted H₂ cellular Wolfhard–Parker flames (WP) burning in N₂-O₂ co-flow taken from [13]; various other conditions specified in Table 3.1 from [29] [▷]; [22] [▽]; [26] [○]; [43] [◇].

creasing reactant Lewis numbers and decreasing initial mixture strength has been demonstrated by the linear stability analysis of Cheatham & Mat-alon [12] for a unstretched planar flame, as well as recently by Rais [87] for the axisymmetric jet flame configuration. The reactant Lewis numbers and the initial mixture strength in experiments, are of course not independently controllable parameters; thus, the variation of both parameters must be considered when analyzing data. As reported previously, the reactant Lewis numbers did not vary significantly over the whole range of the mixture compositions investigated in the current hydrogen-oxygen flames — [1.1–1.2] for oxygen and [0.25–0.28] for hydrogen. The effect of the initial mixture strength, therefore, on the formation of cells is clearly evident in Fig. 3.2. In this figure, the parameter space where cell instabilities occur is relatively broader on the fuel-lean (right-side) side of the graph; thus, the current ex-

3.2 Effect of reactant composition on cellular instabilities

Combust. Theory and Modelling, 7, 2003 [67]

perimental results are consistent with the theoretical work cited above. This observation is also consistent with the previous experimental data reported by Chen *et al.* [13] for nitrogen diluted, hydrogen-oxygen flames established in a Wolfhard–Parker burner (see Table 3.1). In their study, cellular instabilities were not observed for relatively high initial mixture strength values $\phi \gtrsim 1.5$. Despite the relatively low reactant Lewis numbers, the last system reported in Table 3.1 for a SF₆-diluted propane-oxygen jet diffusion is also not cellular as a consequence of the relatively high initial mixture strength.

In order to examine the effects of Lewis number on the flame data reported in Table 3.1, Fig. 3.5 shows selected data in the Lewis number plane. Of particular interest are the data sets in the lower right-hand corner of this figure for the current CO₂-diluted H₂ axisymmetric jet flame experiments (squares) and the N₂-diluted H₂ Wolfhard–Parker flame data reported by Chen *et al.* [13] (triangles). Although the hydrodynamic conditions and burner geometries are not the same for these data, both data sets show that cellular instabilities do not occur above a certain initial mixture strength, as shown by the filled symbols. The arrowed lines next to these data indicate the direction of increasing initial mixture strength. The curves dividing the graph into a cellular and a non-cellular region are taken from Cheatham & Matalon’s [12] stability analysis of a *planar* diffusion flame for three different initial mixture strengths ($\phi_m = 1/3, 1, \text{ and } 2$) very close to the extinction limit (at $\delta - \delta_c = 0.01$ in their article). The selected theoretical curves separate the cellular instability region at relatively low reactant Lewis numbers from the non-cellular region. These results show that the region for cellular instabilities decreases with increasing initial mixture strength, as shown by the dashed arrow in Fig. 3.5. These theoretical trends are in agreement with our recent linear stability results for axisymmetric jet flames near the extinction limit [87].

It must be stressed that the theoretical boundaries in Fig. 3.5 depend on several parameters, including the initial mixture strength. Also, other effects such as density variation and hydrodynamics do not correspond to the various experimental conditions. Nevertheless, the theory correctly reproduces the experimental trends.

3. CELLULAR INSTABILITIES IN JET DIFFUSION FLAMES

3.3 Jet burner velocity profiles

This section will present the flow characteristics of the two jet diffusion burners. Velocity profiles and the initial vorticity thickness have been determined. The velocity profiles presented are in both burners with air instead of fuel. The vorticity thickness has been determined experimentally for both burners with reacting and non-reacting flows. The reacting condition was 20% H₂-80% CO₂ fuel mixture burning in pure oxygen. In the following the Reynolds number is defined as $Re_L = \bar{u}_F L / \nu_F$, where \bar{u}_F is the mean velocity of the fuel outlet, L is the characteristic geometric length scale (D for the AJ burner and W for the WP burner), and ν_F the viscosity of the fuel mixture at cold conditions.

3.3.1 Axisymmetric jet burner

The velocity profile was measured over the nozzle diameter ($D = 7.5$ mm), from ± 3.9 mm, using the LDA apparatus. The distance between the measuring points varied between 0.05 mm and 0.5 mm, where the resolution close to the edge (high gradient region) of the jet was highest. An average of 70 measuring points were used close to the nozzle exit $z = 1$ mm. The turbulence level at the nozzle exit was not measured, but the quality of the facility is reflected by the possibility of obtaining completely steady laminar hydrogen-air flames up to Reynolds numbers of 1750 [86]. The binary data obtained by the burst spectrum analyzer were post-processed by a Matlab code. For every measuring point, 50000 samples (Doppler bursts) were taken. This number was enough to obtain converged mean velocities. Figure 3.6 shows an example of two profiles at $Re_D \approx 775$ and $Re_D \approx 1400$ with the associated standard deviation profiles. The standard deviation profiles show high values on the edge of the nozzle, where the gradient is highest. The profiles are symmetrical, and were repeatable to within less than 2%. For the experiments conducted in Sec. 3.4, the Reynolds number range was $Re_D \in [300, 1500]$.

3.3 Jet burner velocity profiles

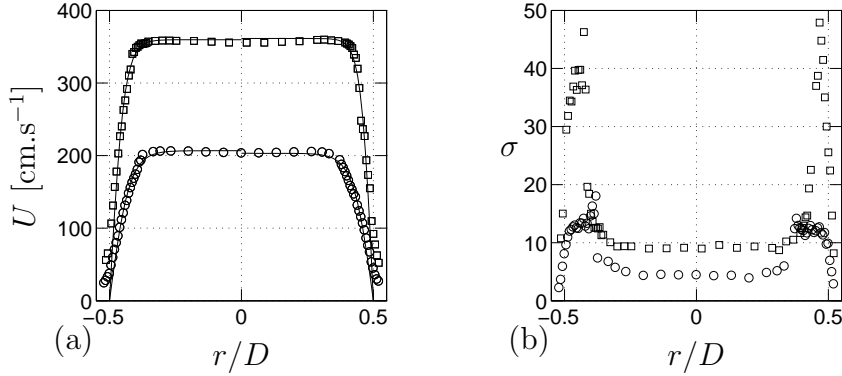


Figure 3.6: Typical velocity measurements from the LDA apparatus for the AJ burner. Profiles for air taken near the fuel outlet at $z = 1$ mm. The $[\square]$ and $[\circ]$ symbols represent the $\text{Re}_D = 775$ and $\text{Re}_D = 1400$ conditions, respectively, based on the mean velocity for air at cold conditions. (a) Axial velocity in $\text{cm}\cdot\text{s}^{-1}$ the solid line correspond to a $u = \tanh$ fit. (b) Standard deviation of the axial velocity in $\text{cm}\cdot\text{s}^{-1}$.

3.3.2 Wolfhard–Parker burner

The velocity profile was measured across the fuel gap ($W = 8$ mm), from ± 4.5 mm, at a distance of $z = 1$ mm from the fuel outlet using the HW anemometer. The distance between the measuring points was fixed to 0.15 mm. Each velocity profile was determined twice with 60 measuring points, and was repeatable to within less than 3%. The calibration of the HW was made before and after each profile. The sampling rate was fixed at 200 Hz during 20 s.

Figure 3.7(a) shows symmetrical velocity profiles. The Reynolds number varied from 200 to 330 (based on the mean velocity). The profiles present a slight overshoot on each side located at a quarter of the gap, due to unavoidable leakage around the upstream screens. For the reacting experiments in Sec. 3.4, the Reynolds number varied from 60 to 300. Figure 3.7(b) shows the uniformity of the flow in the longitudinal direction for the highest Reynolds number ($\text{Re}_W = 330$). The velocity profiles show a nonuniformity of about 5% in the jet core.

3. CELLULAR INSTABILITIES IN JET DIFFUSION FLAMES

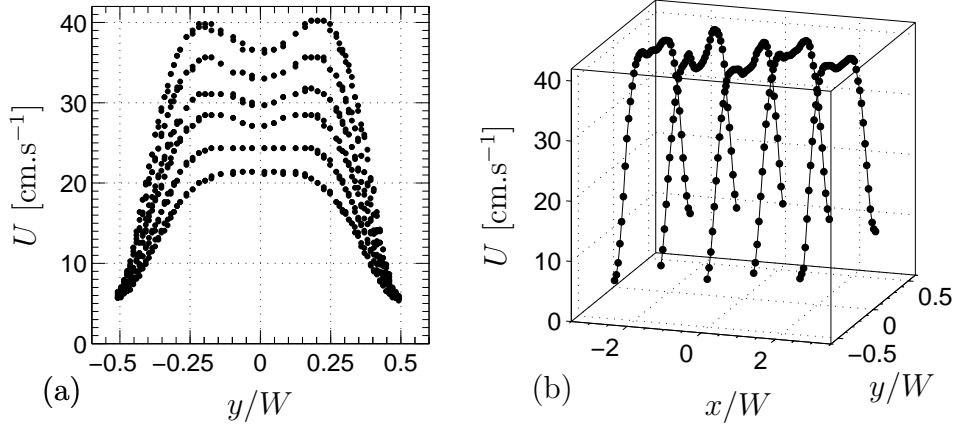


Figure 3.7: Typical velocity measurements from the HW apparatus for the WP burner. Profiles for air taken near the fuel outlet at $z = 1$ mm. (a) Profiles of axial velocity in $\text{cm}\cdot\text{s}^{-1}$ taken at the center of the burner ($y/W = 0$), for Reynolds number ranging from 200 to 330. (b) Profiles of axial velocity taken at several y -locations, for Reynolds number 330.

3.3.3 Determining the vorticity thicknesses

Several scaling lengths are used in the literature for shear layer studies. The most common is the vorticity thickness δ_ω defined as:

$$\frac{\delta_\omega}{L} = \frac{\bar{U}_{\max} - \bar{U}_{\min}}{\left| \frac{d\bar{U}}{dr} \right|_{\max}}, \quad (3.1)$$

where \bar{U} is the mean velocity, and L is a characteristic geometrical length, here the diameter D of the fuel jet for the AJ burner and the width W of the fuel nozzle for the WP burner. Since the co-flow velocity is low compared to the inner flow, the *initial* vorticity thickness is determined assuming $\bar{U}_{\max} = \bar{u}_F$ and $\bar{U}_{\min} = 0$.

The vorticity thickness measurements of the AJ burner were performed with non-reacting (air) and reacting flow. Since the measurements were made near the nozzle exit $z = 1$ mm, the vorticity thickness and the velocity profiles did not change for reacting and non-reacting flows. To obtain the maximum slope of the velocity profiles, the common hyperbolic tangent velocity profile was assumed. This nonlinear curve-fitting was performed with a Matlab function `lsqcurvefit`, which solves nonlinear data-fitting problems. The

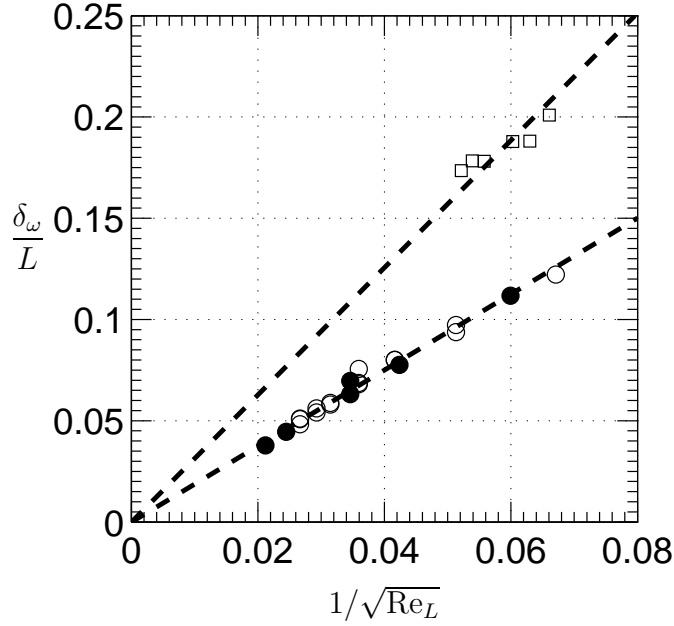


Figure 3.8: Vorticity thickness normalized with the fuel outlet L versus the inverse square root of Re_L . The \square symbols represent the WP burner measurements. The \circ and \bullet symbols represent the AJ burner measurements for the non-reacting (air) and reacting (20% H_2 -80% CO_2 fuel mixture burning in 100% O_2) case, respectively. The dashed-lines represent a linear fit.

determination of the maximum slope was performed by averaging the fitted-slope at the left hand and right hand side of the mixing layer on two successive measurements. The maximum error between the left hand and right hand slopes was found to be less than 0.6%.

The vorticity thickness measurements of the WP burner were only performed for the non-reacting case. Since the difference of δ_ω between the reacting and the non-reacting case is negligible for the AJ burner, the same behavior was assumed for the WP burner. The determination of the maximum slope was graphically obtained by averaging the right and left hand side of the profiles on two successive measurements. The maximum error between the left and right slopes was about 2%.

For laminar flow in the nozzle, the vorticity thickness scales with the

3. CELLULAR INSTABILITIES IN JET DIFFUSION FLAMES

Reynolds number approximately as follows [91]:

$$\frac{\delta_\omega}{L} = m \frac{1}{\sqrt{\text{Re}_L}}, \quad (3.2)$$

where m is a parameter depending on the geometry, and L is the characteristic length scale of the burner. Figure 3.8 shows the vorticity thickness versus the inverse square root of Re_L . Equation (3.2) fits our data well for non-reacting and reacting cases. The error between the left hand and right hand side slopes was about 1.5% for the AJ burner and 5% for the WP burner. The results for the vorticity thickness are:

$$\frac{\delta_\omega}{D} = 1.81 \frac{1}{\sqrt{\text{Re}_D}}, \quad (3.3)$$

$$\frac{\delta_\omega}{W} = 3.14 \frac{1}{\sqrt{\text{Re}_W}}, \quad (3.4)$$

for the AJ and WP burner respectively. A particular effort was made to reduce the uncertainty of Eq. (3.3) and Eq. (3.4) because, as we shall see in Sec. 3.4, this initial vorticity thickness plays a significant role in the stability characteristics of the initial mixing layers.

3.4 Effect of jet velocity on cellular instabilities

This section focuses on cellular instabilities in jet diffusion flames for several fuel velocities with a fixed initial concentration. The jet flow properties at the nozzle exit are mainly imposed by the upstream geometrical properties such as the shape of the contoured nozzle or different flow straighteners. The ratio between the nozzle radius and the vorticity thickness of the shear layer at the jet nozzle exit plays a significant role in the jet behavior [16, 41, 74, 77]. Both the axisymmetric jet (AJ) burner and the Wolfhard–Parker (WP) burner are used for this study. The flames are limited to $\text{H}_2\text{-O}_2$ diluted in CO_2 flames. First, it is useful to consider what happens for a fixed fuel velocity in the previous AJ burner study (Sec. 3.2). The mean velocity in the

3.4 Effect of jet velocity on cellular instabilities

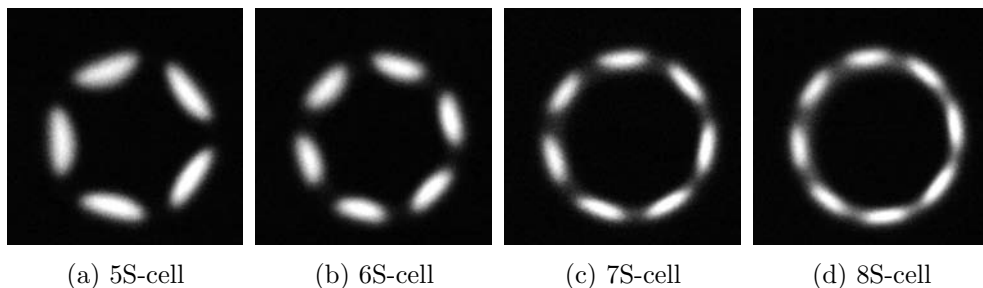


Figure 3.9: Examples of several cellular modes coexisting for a particular state. 17% H₂-83% CO₂ fuel mixture burning in 100% O₂ vol. (a,b): $\bar{u}_F = 0.377 \text{ m.s}^{-1}$; (c,d): $\bar{u}_F = 0.943 \text{ m.s}^{-1}$.

previous study was $\bar{u}_F = 0.377 \text{ m.s}^{-1}$. Cellular states were found to depend significantly on the initial mixture strength and confirm qualitatively the prediction of Cheatham and Matalon [12]. The tendency to form cells was found to decrease with increasing ϕ_m (see Fig. 3.2).

As stated in the introductory chapter and illustrated with Table 1.1, previous studies have not thoroughly investigated the parametric dependance of the cellular wavelength. This wavelength is of importance for quantitative comparison with theory. In this section, experimental data for the wavelength are provided and correlated with the shear layer thickness which in turn depends on the fuel jet velocity, \bar{u}_F . The O₂ concentration and the co-flow mean velocity were fixed at the same value as in Sec. 3.2, i.e. $\bar{u}_O = 4.66 \text{ cm.s}^{-1}$. For the AJ burner, several cellular modes coexisted for a particular operating condition (see previous section) giving discrete values of the cellular wavelength, λ/D , where $D = 7.5 \text{ mm}$ is the nozzle diameter. For the WP burner the values of the cellular wavelength, λ/W , where $W = 8 \text{ mm}$ is the width of the fuel inlet are quasi-continuous. An example is given in Fig. 3.9 for the AJ burner and in Fig. 3.10 for the WP burner.

This section is divided as follows: first, the procedure for determining the different λ/L is presented, where L is the reference length of the AJ or the WP burner. Second, the evolution of cellular boundaries when varying the jet velocity will be discussed. Finally, for a particular value of fuel mixture (17% H₂-83% CO₂ vol.) results for the scaling of the cellular wavelength are

3. CELLULAR INSTABILITIES IN JET DIFFUSION FLAMES

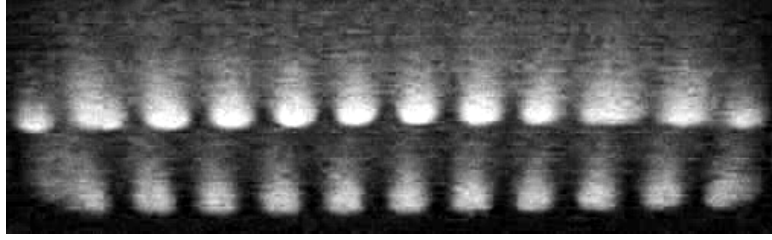


Figure 3.10: Typical two-dimensional cellular flame instability of a diluted hydrogen diffusion flame, from the WP burner. 17% H₂-83% CO₂ fuel mixture burning in 100% O₂ vol.

presented.

3.4.1 Procedure

To determine the width of the cells, pictures of the flames were taken for both jet burners (AJ & WP). For the AJ burner, photographs of the top view of the flame were taken to determine the size of the cells. For the WP burner, digital pictures were taken from an oblique angle at 45° with respect to the horizontal. Calibration photographs of a ruler were taken for both burners.

The AJ burner

For this apparatus, photographs were taken with Nikon D70 digital SLR camera (3008 × 2000 px). To avoid heating up the camera, the downstream distance from the lens to flame was about 60 cm and in addition the AJ burner was placed on a traverse allowing lateral movement of the AJ burner during concentration changes without changing the camera focal plane. In order to maximize the resolution of the camera, a Vivitar macro lens (85-205 mm, 1:3.8, 85 mm dia.) and two extension rings Nikon PK-3 (27.5 mm) and Nikon PK-1 (8 mm) were added. The combination of all these parameters gave a spatial resolution of about 60 px/mm. The resolution was high enough to capture the effective diameter of the flame D_f , based on the maximum of the integrated chemiluminescence. The camera was operated on-line by a USB-connection. These measurements were then processed using a Matlab code. As the center was not fixed, the aim of the code was to sum the

3.4 Effect of jet velocity on cellular instabilities

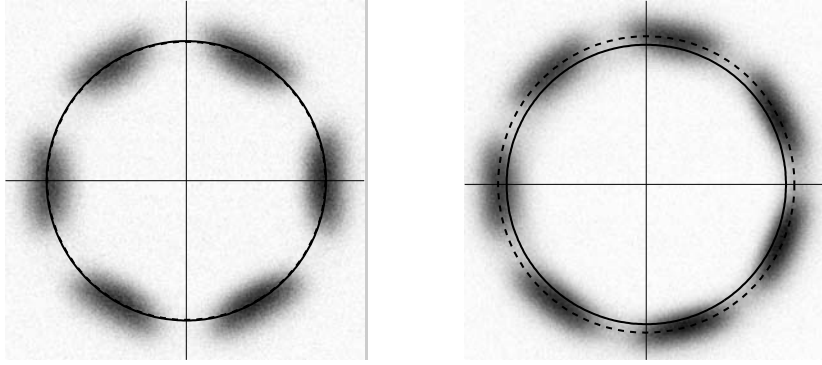


Figure 3.11: Example of two top views of the AJ burner for two different fuel velocities \bar{u}_F . The solid lines represent the burner nozzle inner diameter $D = 7.5$ mm and the dashed lines represent the calculated flame diameter D_f . 17% H₂-83% CO₂ fuel mixture burning in 100% O₂ vol., $\phi_m = 0.0738$. Oxidizer co-flow velocity $\bar{u}_O = 4.66$ cm.s⁻¹. Fuel velocity: $\bar{u}_F = 37.7$ cm.s⁻¹ and $\bar{u}_F = 75.4$ cm.s⁻¹ for left and right photographs respectively.

intensities on a fitted circle (three independent variables: two for the center and one for the radius. The built-in function `fminsearch` for unconstrained nonlinear optimization was used to determine these three parameters.

Figure 3.11 illustrates how cellular wavelengths were obtained. The continuous circle represents the nozzle inner diameter, $D = 7.5$ mm, and the dashed line represents the calculated circle of the flame with the diameter D_f . These photographs were taken for fixed oxidizer and fuel concentration (H₂ = 17% vol., O₂ = 100% vol.) and for a fixed co-flow velocity ($\bar{u}_O = 4.66$ cm.s⁻¹). Only the fuel velocity varied from $\bar{u}_F = 37.7$ cm.s⁻¹ to $\bar{u}_F = 75.4$ cm.s⁻¹. The left hand photograph shows that for the lowest velocity the flame diameter is nearly the same as the nozzle diameter and that there are 6 cells. The right hand photograph shows a larger flame diameter and a 7-cell state. The cellular wavelengths are then simply obtained by dividing the circle perimeter by the number of cells:

$$\lambda = \frac{\pi D_f}{N_{\text{cell}}}, \quad (3.5)$$

3. CELLULAR INSTABILITIES IN JET DIFFUSION FLAMES

where N_{cell} is the number of cells observed⁴. The repeatability was within 1%, provided the photograph was not saturated.

The WP burner

For the data acquisition, a SONY DSC-F828 Digital Still Camera (3264×2448 px) was used. The camera was positioned on the side of the burner, with an oblique angle of about 45° and at 8 cm from the flame. The combination of these parameters gave a spatial resolution of about 50 px/mm. The pictures were taken for various conditions with the speed burst mode, i.e. seven pictures every 0.38 s and a shutter time of 30 ms. The reason for collecting pictures at this speed was that the cells in the WP burner, for certain conditions, were more likely to move laterally without any preferred direction.

Figures 3.12–3.13 illustrates how cellular wavelengths were determined. The black lines, on the top picture of Fig. 3.12, represent the region of interest (ROI). The bottom graph shows the filtered signal of the raw signal taken at the center of the ROI. The ROI had a height of 60 pixels. The wavelength was determined as follows: for each row in the 60 pixels ROI, the signal was low-pass filtered; then, on each filtered signal a Hanning window and zero padding were applied in order to obtain 8192 long samples. These samples were then processed with a Fast Fourier Transform (FFT) and the average of each peak obtained determined our λ/W . Figure 3.13 shows the results of the same filtered signal presented at the bottom of Fig. 3.12. The calculated cellular wavelength for each photograph can be written as:

$$f_i(x) \xrightarrow{\text{FFT}} \hat{f}_i(k) \implies k_i^* \text{ as the } \max \left| \hat{f}_i(k_i^*) \right| ,$$
$$\lambda = \frac{1}{N} \sum_{i=1}^N \frac{1}{k_i^*} , \text{ for } N = 60 . \quad (3.6)$$

⁴If the inner diameter of the jet had been used as a length scale, the cellular wavelength would have been underestimated: 3.36 mm instead of 3.59 mm, for the example illustrated in Fig. 3.11

3.4 Effect of jet velocity on cellular instabilities

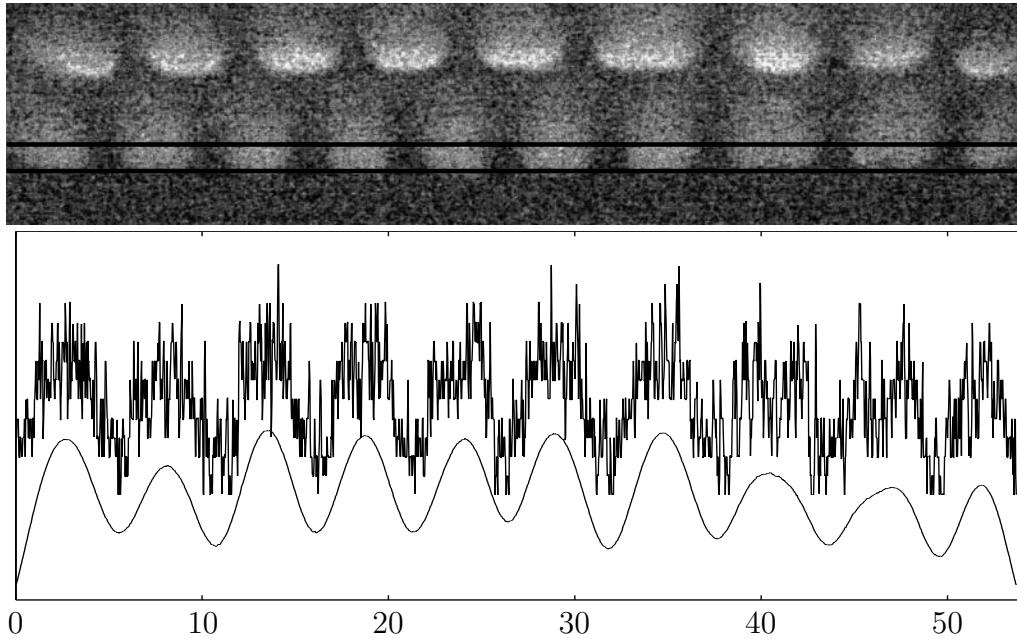


Figure 3.12: Top: Typical photograph of the diffusion flame in the WP apparatus. The black lines represent the region where the wavelength was determined (ROI). Conditions: $\bar{u}_F = 0.186 \text{ m.s}^{-1}$, 17% H_2 -83% CO_2 fuel mixture burning in 100% O_2 vol., $\phi_m = 0.0738$. Bottom: typical raw signal (intensity versus the longitudinal axis of the burner given in mm) at a center position of the ROI and the low-pass filtered signal.

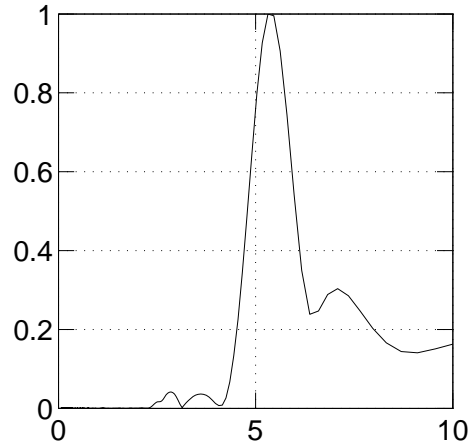


Figure 3.13: Typical result of a FFT from the filtered signal of Fig. 3.12. The FFT was performed after applying a Hanning window and padding of zeros up to 8192. The abscissa is in mm.

3. CELLULAR INSTABILITIES IN JET DIFFUSION FLAMES

3.4.2 Results

Cellular boundaries

In the previous section (see Sec. 3.2), the jet and co-flow velocities have been fixed and a wide variety of cellular states was found. A map (see Fig. 3.2) of the ϕ -parameter space (the range of initial mixture strengths) in which different cell patterns appear has been constructed. More information is needed to understand the physical effects of the large amount of parameters involved in cell formation in jet burners. This relative lack of experimental data motivated this new parameter space investigation (varying the fuel velocity).

Figure 3.14 reports the cellular modes occurring in the AJ burner for several jet flow velocities. The detection of the cell modes, i.e. the number of the cells occurring, was performed directly by visualization. In order to detect several cellular modes at one condition, the flame was manually disturbed using a bluff-body⁵. Measurements were performed for several values of \bar{u}_F ranging from 0.3 to 3.4 m.s⁻¹ in steps of 0.18 m.s⁻¹ (0.5 sl/min). The concentration of H₂ was varied from 14.1% to 21.1% vol. in steps of 0.2% vol. in the cellular region. For the determination of the cellular boundaries, namely the extinction limit and the onset limit, the steps were reduced to 0.1% vol. The extinction boundaries were repeatable within 0.1% vol. For the onset limit the error is larger for high values of \bar{u}_F than for low ones. For high fuel velocity the cell ‘flamelets’ are close to each other making the onset of cells less clear. The repeatability for the onset limit is estimated to be around 0.3% vol. The measurements were performed by fixing \bar{u}_F and decreasing the concentration of H₂.

Figure 3.14 shows several important features. Concerning the cellular modes, up to three different cellular modes could coexist for several conditions. With increasing \bar{u}_F the cell length λ/D — inversely proportional to the cellular mode — is found to decrease; the onset limit decreases making the cellular zone smaller since the extinction limit is found to be less sensitive to this parameter. It should be noted that higher values of λ/D occur very near the extinction limit even for high values of \bar{u}_F .

⁵The same bluff-body as in Sec. 3.2, i.e. a screwdriver.

3.4 Effect of jet velocity on cellular instabilities

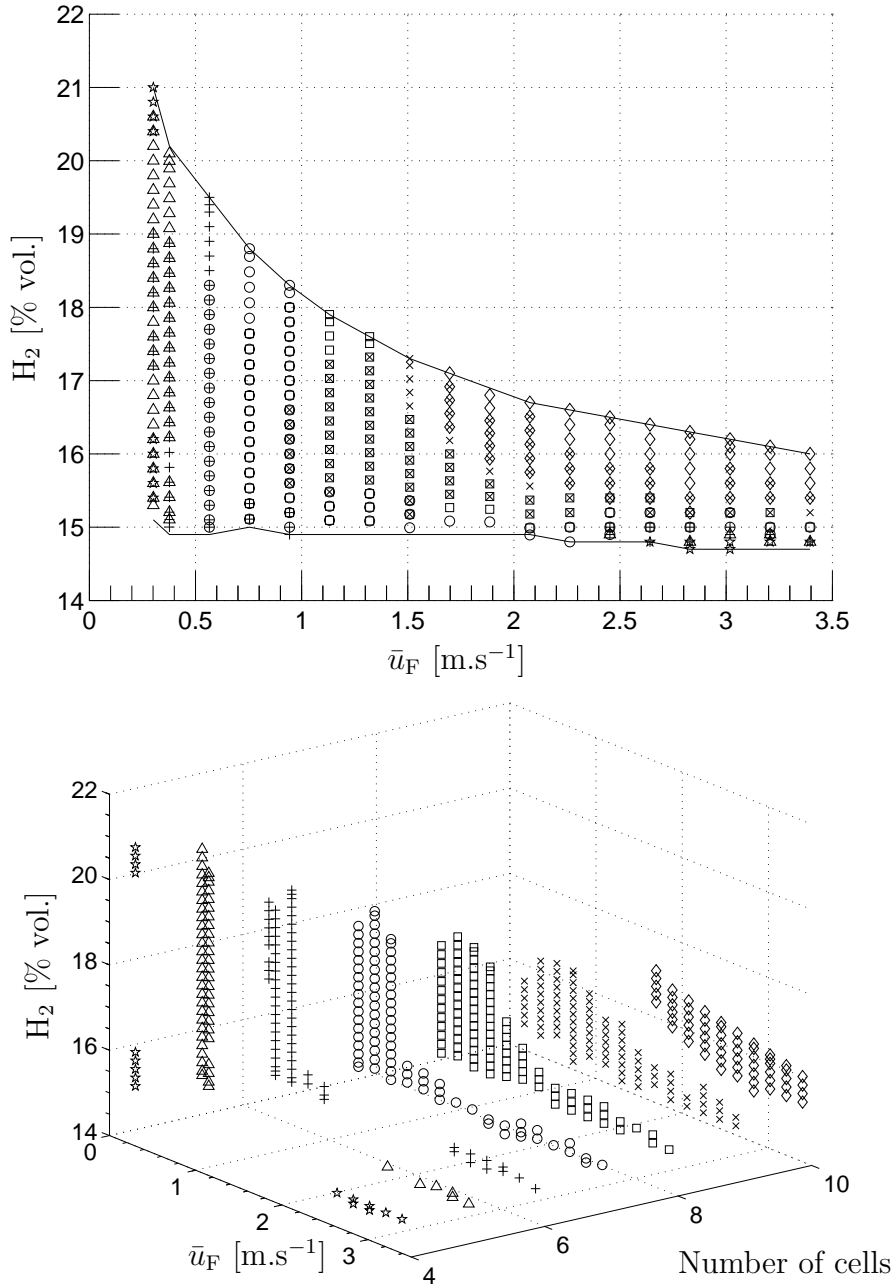


Figure 3.14: Extinction limit and boundaries of different cellular instabilities observed in AJ diffusion flames. H_2 - CO_2 fuel mixture burning in 100% O_2 . Oxidizer co-flow velocity $\bar{u}_O = 4.66$ cm.s⁻¹. The related cellular symbols are found on the bottom graph.

3. CELLULAR INSTABILITIES IN JET DIFFUSION FLAMES

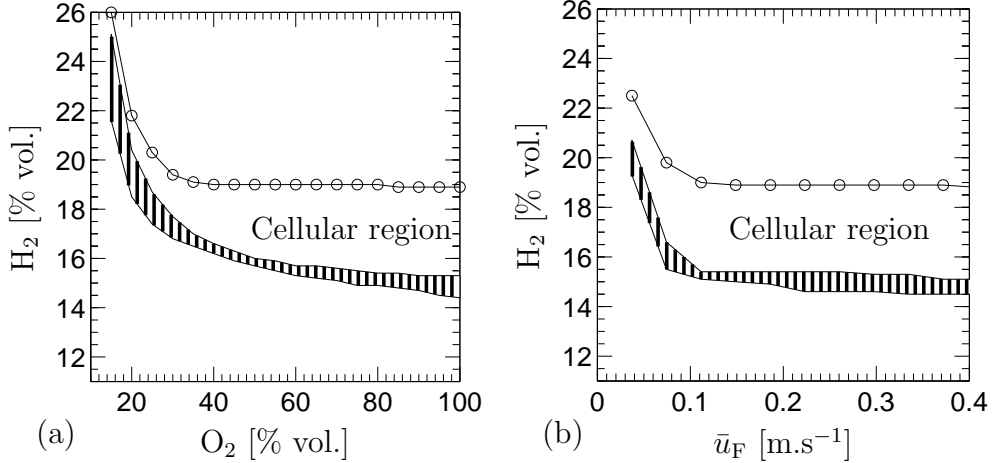


Figure 3.15: Extinction limit and boundaries of the onset and lift-off of cellular instabilities observed for CO₂ diluted, H₂-O₂ diffusion flames in WP burner. The onset limit is represented with lines and circles. The region between the lift-off limit and the extinction limit is hatched. The oxidizer co-flow velocity is $\bar{u}_O = 4.66 \text{ cm.s}^{-1}$. (a) Fixed fuel velocity condition: $\bar{u}_F = 0.377 \text{ m.s}^{-1}$. (b) Fixed oxidizer concentration: O₂ = 100% vol.

Similar investigations of the cellular instabilities occurring in the WP burner have been undertaken. Figure 3.15 shows the cellular instability boundaries for the two parameters investigated: (1) decreasing O₂% for a fixed velocity and (2) increasing \bar{u}_F for a fixed O₂ concentration. The probability of finding cellular instabilities in the WP burner increases as ϕ_m decreases. The determination of the different boundaries was made by fixing the O₂ concentration and decreasing in small steps 0.1% H₂ vol. The position of the fixed parameter — O₂ concentration for Fig. 3.15(a) or \bar{u}_F for Fig. 3.15(b) — is represented with the circle symbol on the onset limit line. It should be noted that the hatched region represented in Fig. 3.15(a,b) corresponds to flame lift-off (approximately 3W high), which is present near the extinction limit. This behavior is similar to the one recorded in the early work of Dongworth and Melvin [22]. The anchoring edges of these flames, which were lifted above the jet nozzle rim, were found to meander in the downstream direction, but regular flame-edge oscillations [26, 27] were not

3.4 Effect of jet velocity on cellular instabilities

observed for the conditions explored. Since it is not the focus of the current study, this lifted flame regime will not be discussed further. The extinction limit is found to be less sensitive to the \bar{u}_F parameter than with ϕ_m . These results are similar to those found with the AJ burner.

Behavior of the cells

To investigate the precise dependence of the cellular wavelength in both jet facilities, the number of variable parameters must first be reduced. The cellular wavelength function can be written as:

$$\lambda = f(Y_F, Y_O, u_F, u_O, \text{geometry, reactant properties}) ,$$

where Y_k are the mass fractions. Keeping the co-flow velocity constant, $\bar{u}_O = 4.66 \text{ cm.s}^{-1}$, and assuming that it is small compared to the fuel velocity allows to neglect the dependence on \bar{u}_O . To further reduce the number of parameters, the initial concentration are kept fixed at $[\text{H}_2] = 17\% \text{ vol.}$ and $[\text{O}_2] = 100\% \text{ vol.}$ with CO_2 as inert in all cases ($\phi_m = 0.0738$). This fuel mixture covers a wide range of the cellular zone in both burners, see Fig. 3.14 and Fig. 3.15(b). The cellular wavelength can be rewritten as:

$$\lambda = f(u_F, \text{geometry}) ,$$

if the reactant properties and the initial mixture strength are held constant. The ‘‘geometry’’ includes the vorticity thickness in each burner determined in Sec. 3.3.3. Here . Eqs. (3.3)–(3.4) and the notations are repeated:

$$\frac{\delta_\omega}{L} = \begin{cases} \frac{\delta_\omega}{D} = 1.81 \frac{1}{\sqrt{\text{Re}_D}} \\ \frac{\delta_\omega}{W} = 3.14 \frac{1}{\sqrt{\text{Re}_W}} \end{cases} \quad L = \begin{cases} D = 7.5 \text{ mm} \rightarrow \text{O} \\ W = 8.0 \text{ mm} \rightarrow \square - \square \end{cases} \quad \text{Re}_L = \frac{\bar{u}_F L}{\nu_F} ,$$

with ν_F the fuel viscosity taken at 300 K for the concentration indicated above [46]. It should be noted from the above equations that the coefficient before the inverse square root of Re_L is different for the two burners. This characteristic is important in the sense that it will permit to distinguish between a scaling with Re_L and δ_ω/L .

3. CELLULAR INSTABILITIES IN JET DIFFUSION FLAMES

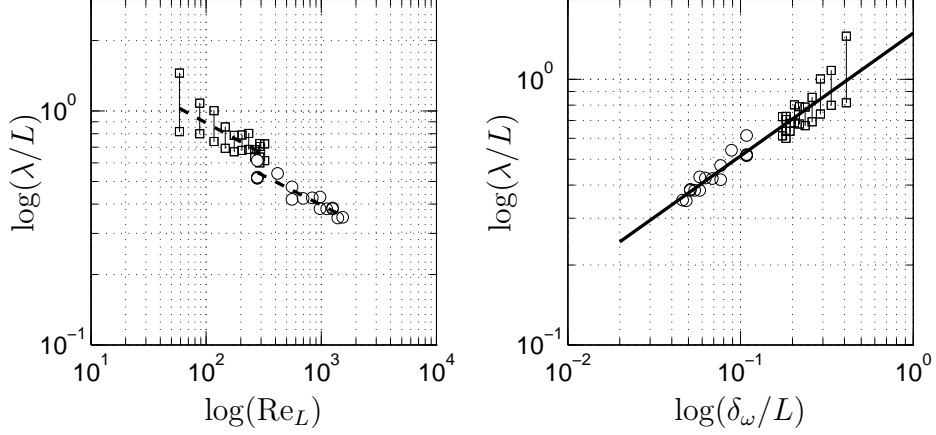


Figure 3.16: Cellular wavelengths measurement in the WP and AJ burner, for 17% H₂-83% CO₂ fuel mixture burning in 100% O₂ vol., $\phi_m = 0.0738$. [O]: Cellular wavelengths from the AJ burner λ/D ; [□—□]: cellular wavelengths from the WP burner λ/W . The solid line is fit through symbols. (a) Scaling with Re_L . (b) Scaling with δ_ω/L .

Figure 3.16 shows the cellular wavelength λ/L measurements in both burners for 17% H₂-83% CO₂ fuel mixture burning in 100% O₂ vol. It should be noted that several wavelength coexist for a particular fuel velocity, therefore the line between the symbols represents the variation of the number of cells observed. Figure 3.16(a) shows that the trend of the cellular wavelengths with the fuel velocity is the same for both burners, but that both data sets do not collapse. When plotted against δ_ω/L , however, all data collapse onto a single line in Fig. 3.16(b). The line fitted through both sets of measurements in fact covers the separate fits of each data set. Therefore, the geometry dependence of the cellular wavelength is given by:

$$\frac{\lambda}{L} = a\sqrt{\frac{\delta_\omega}{L}}. \quad (3.7)$$

For the flame conditions specified above, the empirical coefficient $a = 1.6$ is found from Fig. 3.17. The coefficient is found to be equal to $a = 1.6$. Figure 3.17 also present a blow-up of the AJ burner data which illustrates that the cellular wavelengths from the AJ burner are strongly “quantized” by Eq. (3.5) compared to the ones from the WP burner. Therefore, the resulting

3.4 Effect of jet velocity on cellular instabilities

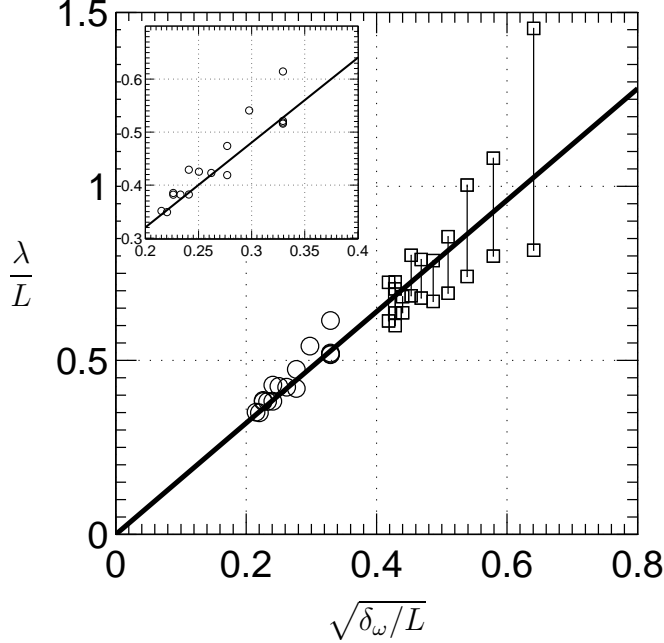


Figure 3.17: Cellular wavelengths measurement in the WP and AJ burner, for 17% H₂-83% CO₂ fuel mixture burning in 100% O₂ vol., $\phi_m = 0.0738$. [○]: Cellular wavelengths from the AJ burner λ/D ; [□—□]: Cellular wavelengths from the WP burner λ/W . The solid line is given by Eq. (3.7), with $a = 1.6$.

relations should be regarded as *typical* cellular wavelengths.

As discussed previously, the parameter a is dependent on the flame parameters and the reactant properties. Notably, it was shown that increasing initial mixture strength increases the wavelength of the cellular instability. For fixed initial fuel mixture, the cellular instability domain changes smoothly with increasing ϕ_m , up to a particular value of O₂ close to extinction, see Fig. 3.2 and Fig. 3.15 for the AJ and the WP burner, respectively. Consequently the reactant properties are assumed to be constant sufficiently far from the O₂ extinction limit. This last assumption decouples the effect of ϕ_m from the one of δ_ω in the cellular wavelength relation:

$$\frac{\lambda}{L} = a(\phi_m) \sqrt{\frac{\delta_\omega}{L}}. \quad (3.8)$$

Additional experiments were conducted to see if a suitable relation could

3. CELLULAR INSTABILITIES IN JET DIFFUSION FLAMES

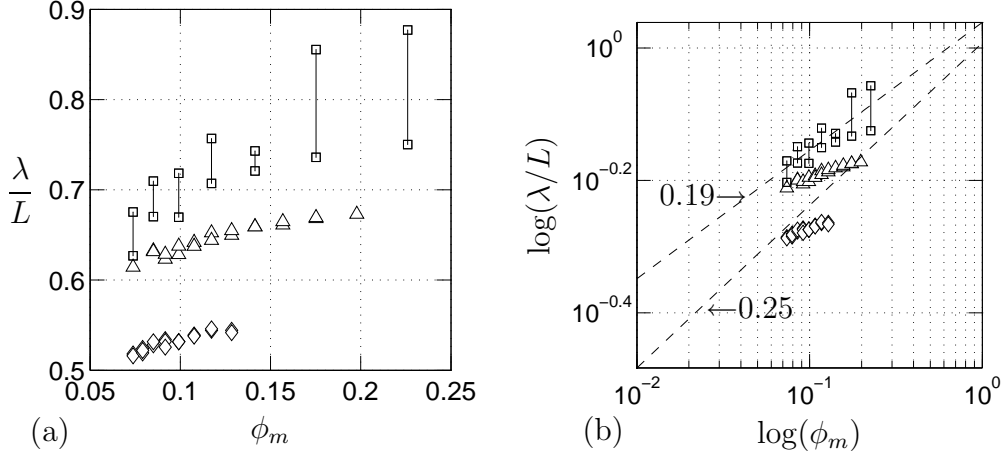


Figure 3.18: Cellular wavelengths measurement in the WP and AJ burner, for 17% H₂-83% CO₂ fuel mixture burning in O₂-CO₂ mixture. The fuel velocity and the oxidizer co-flow velocity is $\bar{u}_F = 0.377 \text{ m.s}^{-1}$ and $\bar{u}_O = 4.66 \text{ cm.s}^{-1}$, respectively. [Δ]: 5-cell mode wavelengths from the AJ burner; [\diamond]: 6-cell mode wavelengths from the AJ burner; [\square — \square]: cellular wavelengths from the WP burner. (a) λ/L versus ϕ_m ; (b) $\log(\lambda/L)$ versus $\log(\phi_m)$. [- -]: fit through the cellular wavelength of the two burners.

be found for $a(\phi_m)$. The velocities of the jet flow and the co-flow were held constant for both burners. The fuel velocity and the oxidizer co-flow velocity was $\bar{u}_F = 0.377 \text{ m.s}^{-1}$ and $\bar{u}_O = 4.66 \text{ cm.s}^{-1}$, respectively. The fuel mixture was fixed to 17% H₂-83% CO₂, for both burners. It should be recalled that even if the fuel velocities are equal for both burners, the vorticity thicknesses are different (see Fig. 3.17).

Figure 3.18 confirms that the cellular wavelengths increase with increasing initial mixture strength ϕ_m . Only two cellular modes were observed in the AJ burner, compared to a higher number of cellular modes in the WP burner. Assuming a power law for $a(\phi_m) = b\phi_m^\gamma$, two different powers are found for the two burners on Fig 3.18(b). Since the two powers are close, the average $\gamma = 0.22$ is used to arrive at:

$$\frac{\lambda}{L} = b\phi_m^\gamma \sqrt{\frac{\delta_\omega}{L}}, \quad (3.9)$$

To confirm this relation and to find the appropriate empirical coefficient $b = 2.83$ all data are plotted on Fig. 3.19. To confirm Eq. (3.9), still more

3.4 Effect of jet velocity on cellular instabilities

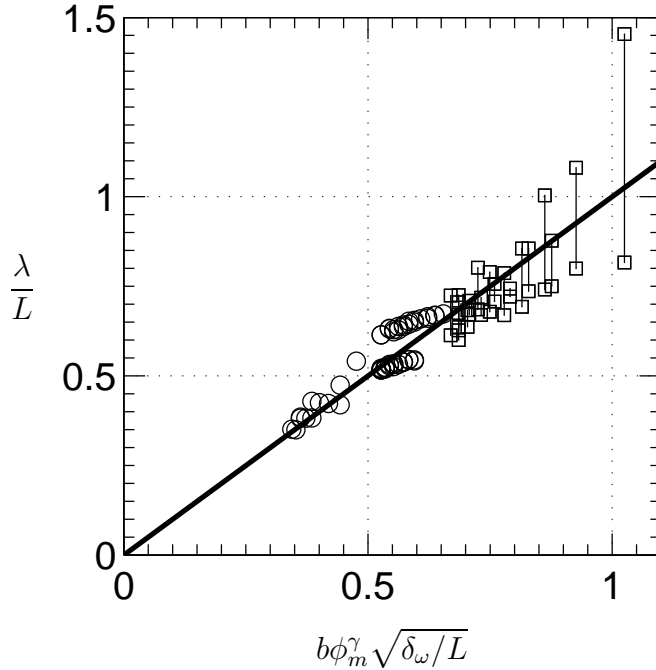


Figure 3.19: Cellular wavelengths measurement in the WP and AJ burner, for 17% H₂-83% CO₂ fuel mixture burning in O₂-CO₂ mixture. The fuel velocity and the oxidizer co-flow velocity is $\bar{u}_F = 0.377 \text{ m.s}^{-1}$ and $\bar{u}_O = 4.66 \text{ cm.s}^{-1}$, respectively. [O]: Cellular wavelengths from the AJ burner for $\phi_m = 0.0738$; [Δ]: 5-cell mode wavelengths from the AJ burner; [\diamond]: 6-cell mode wavelengths from the AJ burner; [\square — \square]: cellular wavelengths from the WP burner. Empirical fitted values: $\gamma = 0.22$ and $b = 2.83$.

measurements for different combinations of δ_ω and ϕ_m are required. In addition, the parameters γ and b are expected to be dependant on the thermochemical properties of the reactants. To explore this suggestion, additional experiments are required with other reactants. Replacing the CO₂ inert with CF₄ will lower the Lewis number without changing the combustion properties. Other inerts with higher molecular weights than CF₄ (SF₆, Xe, Kr, ...) can sufficiently reduce the Lewis number of the hydrocarbons so that cellular instabilities are possible. In the hydrogen system higher Lewis numbers can be obtained with inerts such as Ar or N₂, which are known to produce cellular instabilities [13, 22, 43]. However these inerts will lower the chemiluminescence and the identification of cells may become difficult.

3. CELLULAR INSTABILITIES IN JET DIFFUSION FLAMES

Conclusions

An empirical scaling of the cellular instability wavelength was found, for a 17% H₂-83% CO₂ fuel mixture burning in a O₂-CO₂ mixture. This scaling is based on a large Reynolds number variation from 50 to 1500 at a fixed $\phi_m = 0.0738$, and a variation of $\phi_m \in [0.0738, 0.2260]$, at one fixed fuel Reynolds number. This empirical relation is valid if several hypotheses are met. Firstly, the oxidizer co-flow velocity has to be low compared to the fuel velocity. Secondly, the thermo-chemical properties (reactant properties) were assumed to be constant sufficiently far from extinction. Therefore, high values of the cellular wavelengths for conditions very close to extinction cannot be predicted with the empirical relation Eq. (3.9), see Fig. 3.4 and Fig. 3.14. However, the region near-extinction where there are large changes in the cellular wavelength is small.

The Damköhler number for jet diffusion flames is the ratio between the hydrodynamic effects and chemical effects. Two regimes can therefore be distinguished: a near-extinction regime where λ/L is controlled primarily by the thermo-chemical parameters and a second regime, investigated here, where λ/L is determined primarily by hydrodynamics.

Additional measurements are needed to confirm these results, notably, the dependence on the physical properties of the reactants (thermal and mass diffusion). The initial assumption of a small co-flow velocity needs to be studied as Fűri [26] reported different cellular behavior, such as traveling cells, when varying the oxidizer co-flow in the WP burner.

Chapter 4

Realization of a nearly one-dimensional diffusion flame

4.1 Introduction

This chapter is devoted to a new type burner designed to produce a one-dimensional diffusion flame. The material is in essence contained in the Combustion Symposium paper [66] mentioned in the title. However, for consistency and clarity purposes the presentation has been modified and the original paper expanded. The additional material consists of velocity measurements (Sec. 4.4.1) and temperature measurements (Sec. 4.4.2). A notable modification has also been made to the discussion of the flame stand-off distance and corresponding figure in Sec. 4.4.3.

A unique burner was constructed to realize experimentally a one-dimensional *unstrained* planar non-premixed flame, previously only considered in idealized theoretical models. The potential experiments in such a burner, free of flame stretch effects, include investigations of instabilities, extinction dynamics and heat loss and chemistry effects. The capabilities of this unique burner are demonstrated in Chap. 5 with a preliminary investigation of cell formation in CO₂-diluted H₂-O₂, *nearly unstrained* non-premixed flames near the extinction limit.

The *unstrained* one-dimensional diffusion flame has served for over six decades, starting with Zeldovich [118], Shvab [94], and Spalding [103, 104],

4. REALIZATION OF A NEARLY ONE-DIMENSIONAL DIFFUSION FLAME

as an idealized construct for theoretical modeling. The principal obstacle in the way of an experimental realization of this idealized burner is the uniform oxidizer supply. Even with a screen separating the chamber from the fast oxidizer stream across the top of the combustion chamber, one-dimensionality in the chamber is unlikely to be approached in practice, as it can only be expected in the limit of an infinite ratio between the cross stream and chamber exhaust velocities. Therefore, experimental investigations of non-premixed flames have until now been restricted to burners which produce non-uniform conditions over the flame surface. Several common burners are the Wolfhard–Parker burner, axisymmetric jet and counterflow configurations. Of the cited examples, the counterflow burner comes closest to the idealized burner discussed above. There are two major types of counterflow diffusion flames, namely the opposed-jet and Tsuji burners. Opposed jet flames are planar, i.e. free from curvature effects, but the flow is non-uniform and characterized by a single parameter — the axial velocity gradient or strain rate. Recently, Han *et al.* [35] proposed an original idea to obtain low strain flame by means of a Tsuji burner with a small curvature. They were able to obtain flames with a strain rate around 1.4 s^{-1} .

This chapter will be organized as follows. The details of the theoretical model will be discussed in Sec. 4.2. The design consideration and details of the burner construction are discussed in the Sec. 4.3. Experimental characterization (Sec. 4.4) includes velocity, temperature and stand-off distance measurements will end this chapter.

4.2 The theoretical one-dimensional burner

The idealized burner is supplied from the bottom with one reactant, the fuel in this study¹, through a “semi-permeable plate” (impermeable in the downward direction). The oxidizer diffuses from a reservoir on top of the chamber to the flame, against the upward flow of products. Conditions at the boundary where the oxidizer originates are maintained constant by a fast-flowing oxidizer stream across the top exit of the combustion chamber.

¹the role played by the two reactants can be easily interchanged.

4.2 The theoretical one-dimensional burner

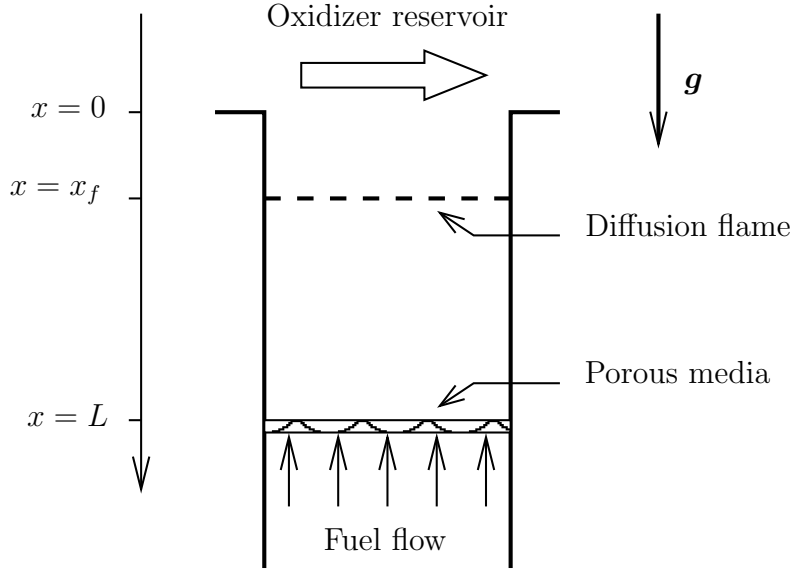
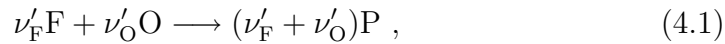


Figure 4.1: Schematic of the ideal 1-D model.

The supply of both reactants is assumed to be uniform over the respective horizontal burner cross sections such that the velocity, which is directed upwards because of the bottom semi-permeable plate, as well as all other physical quantities depend only on the vertical coordinate normal to the planar flame (see Fig. 4.1).

The chemical activity is modeled by a one-step global irreversible reaction of the form



where ν'_k is the stoichiometric coefficient of species k , and F , O , and P represents the fuel, the oxidizer and the products respectively. The chemical reaction rate ω is assumed to obey an Arrhenius type law:

$$\omega = A \frac{\rho Y_F}{W_F} \frac{\rho Y_O}{W_O} \exp\left(\frac{-E_a}{RT}\right) , \quad (4.2)$$

with R the gas constant, T the temperature, E_a the overall activation energy, A a constant pre-exponential factor, ρ the density of the mixture, W_k and Y_k are the molecular weight and the mass fraction of species k respectively. For steady burning, the equations of conservation of mass, momentum and

4. REALIZATION OF A NEARLY ONE-DIMENSIONAL DIFFUSION FLAME

energy are expressed as follow:

$$\rho u = \text{const.} , \quad (4.3)$$

$$\rho u u_{,x} = -p_{,x} + \rho g + (4/3)(\mu u_{,x})_{,x} , \quad (4.4)$$

$$\rho u c_p T_{,x} - (\lambda T_{,x})_{,x} = Q \omega , \quad (4.5)$$

$$\rho u Y_{F,x} - (\rho \mathcal{D}_F Y_{F,x})_{,x} = -\nu_F W_F \omega , \quad (4.6)$$

$$\rho u Y_{O,x} - (\rho \mathcal{D}_O Y_{O,x})_{,x} = -\nu_O W_O \omega , \quad (4.7)$$

where p represent the pressure, g the gravitational acceleration, Q the total heat released during combustion, λ , c_p and μ are the thermal conductivity, specific heat at constant pressure and dynamic viscosity of the mixture, and \mathcal{D}_k is the binary diffusion coefficient of species k .

For low-speed flows (isobaric assumption, low Mach number) it can be that the spatial variation in pressure is small, so that the equation of state can be written as follow:

$$p_0 = \frac{\rho R T}{\bar{W}} , \quad (4.8)$$

with P_0 representing the ambient pressure and \bar{W} the mixture average molecular weight. The boundary conditions for the top $x = 0$ and bottom $x = L$ of the chamber are:

$$x = 0 : \begin{cases} T = T_{O_i} , \\ Y_F = 0 , \\ Y_O = Y_{O_i} , \\ p = 0 , \end{cases} \quad x = L : \begin{cases} \lambda T_{,x} = \rho u (T - T_{F_i}) , \\ \rho \mathcal{D}_F Y_{F,x} = \rho u (Y_F - Y_{F_i}) , \\ \rho \mathcal{D}_O Y_{O,x} = \rho u Y_O , \end{cases} \quad (4.9)$$

where Y_{F_i} and Y_{O_i} are the initial mass fraction of fuel and oxidizer respectively. The solution corresponding to complete combustion, called the Burke–Schumann solution [9], will be presented. This solution is also designated as “fast-chemistry” because the associated Damköhler number, Dam , tends to infinity. This correspond to the leading order of an asymptotic solution for large activation energy² [12, 49, 52, 64]. This solution will not allow any leak-

²For finite Damköhler number the following expression are not the same but the position of the reaction sheet remains very close which therefore could be used as a reasonable

4.2 The theoretical one-dimensional burner

age of the reactants. The reaction zone thickness will be infinitely small (also called flame sheet model) and will be located at $x = x_f$ where fuel and oxidizer meet at stoichiometric proportions. Assuming transport properties $\lambda, \mu, c_p, \rho \mathcal{D}_k$ remain constants, and denoting $\hat{x} = x/L$ the following solution is found for the fuel and oxidizer mass fractions:

$$Y_O = \begin{cases} Y_{O_i} \phi_m [-1 + \exp(-\text{PeLe}_O(\hat{x} - \hat{x}_f))] , & \forall \hat{x} \in [0, \hat{x}_f[\\ 0 , & \forall \hat{x} \in]\hat{x}_f, 1] \end{cases} \quad (4.10)$$

$$Y_F = \begin{cases} 0 , & \forall \hat{x} \in [0, \hat{x}_f[\\ Y_{F_i} [1 - \exp(\text{PeLe}_F(\hat{x}_f - \hat{x}))] , & \forall \hat{x} \in]\hat{x}_f, 1] \end{cases} \quad (4.11)$$

The reaction sheet location \hat{x}_f is located:

$$\hat{x}_f = (\text{PeLe}_O)^{-1} \ln(1 + \phi_m^{-1}) , \quad (4.12)$$

where

$$\phi_m = \frac{Y_{F_i}/\nu_F W_F}{Y_{O_i}/\nu_O W_O} , \quad (4.13)$$

is the (mass) initial mixture strength. The two Lewis number Le_F and Le_O are associated to the fuel and the oxidizer respectively. The Lewis number represents the ratio between heat and mass transfer and is defined for a specie k as, $\text{Le}_k = \mathcal{D}_{\text{th}}/\mathcal{D}_k$, where \mathcal{D}_{th} is the thermal diffusivity $\mathcal{D}_{\text{th}} = \lambda/(\rho c_p)$. The Péclet number³ Pe represents the ratio between convective transport and thermal diffusive transport and is defined as $\text{Pe} = uL/\mathcal{D}_{\text{th}}$. The temperature profile reads:

$$T = \begin{cases} T_f + (T_f - T_{O_i}) \frac{\exp(-\text{Pe}(\hat{x} - \hat{x}_f) + 1)}{\exp(-\text{Pe}(1 - \hat{x}_f) - 1)} , & \forall \hat{x} \in [0, \hat{x}_f[\\ T_{F_i} + (T_f - T_{F_i}) \exp(\text{Pe}(\hat{x}_f - \hat{x})) , & \forall \hat{x} \in]\hat{x}_f, 1] \end{cases} \quad (4.14)$$

approximation of the flame position [12]

³In literature concerning diffusion in reactors the term PeLe is replaced by the Bodenstein number Bs , or in porous media literature is replaced by Pe_m which is a Péclet number defined with mass diffusivity instead of thermal diffusivity.

4. REALIZATION OF A NEARLY ONE-DIMENSIONAL DIFFUSION FLAME

where the flame temperature T_f is given by:

$$T_f = T_{\text{Fi}} + \frac{q}{c_p} + \left(T_{\text{Oi}} - T_{\text{Fi}} - \frac{q}{c_p} \right) \left(1 + \frac{1}{\phi_m} \right)^{-1/\text{Le}_O}, \quad (4.15)$$

where $q = QY_{\text{Fi}}/\nu_{\text{F}}W_{\text{F}}$ is the heat release per mass unit of fuel supplied. In this configuration where oxidizer diffuses against the bulk flow only Le_O is present in the relations Eq. (4.12) and Eq. (4.15).

The density and the velocity fields can be solved from the equation of state Eq. (4.8) and Eq. (4.3):

$$\frac{u}{U_{\text{Fi}}} = \frac{\rho}{\rho_{\text{Fi}}} = \frac{T_{\text{Fi}}}{T}. \quad (4.16)$$

4.3 Design considerations

Proc. Comb. Inst., **30**, 2005 [66], expanded

The idealized burner in these studies is supplied with one reactant from the bottom through a “semi-permeable plate” — impermeable in the downward direction. The other reactant diffuses from the top of the chamber to the flame, against the upward flow of products. The supply of both reactants is assumed to be uniform over the burner cross section such that the velocity, which is upwards everywhere, and all other physical quantities depend only on the (vertical) coordinate normal to the planar flame. Since the uniform supply of the reactant diffusing against the bulk flow is a major experimental problem, laboratory investigations of non-premixed flames have until now been limited to burners with non-uniform conditions over the flame surface.

In order to more directly compare the theoretical results for the 1-D ideal flame with experiments, a new improved experimental realization of the ideal burner has been constructed. On the left hand side of Fig. 4.2 the idealized model with additional arrows is shown, where the straight ones correspond to convective transport and the wiggly ones to diffusive transport. The key for the uniform removal of products is to redesign the top of the idealized burner. By introducing an array of tubes through which the oxidizer is supplied the products can escape in-between the tubes, as shown on the right hand side.

4.3 Design considerations

Proc. Comb. Inst., **30**, 2005 [66], expanded

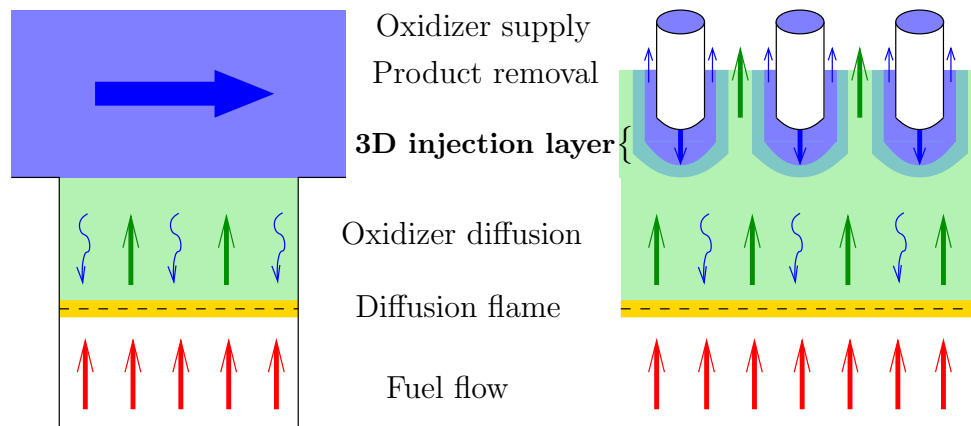


Figure 4.2: Sketch of the idealized burner (left) and the experimental realization (right). The straight arrows correspond to convective transport and the wavy ones to diffusion transport.

A three-dimensional layer therefore exist where the oxidizer and the products mix and where below this region the oxidizer diffuses down to the flame in the same manner as depicted in the idealized burner. The key of this apparatus is that the tube supply and the tube spacing must be kept small enough so that the non uniformity is in a smaller scale compared to the scale of the phenomena to be studied.

Figure 4.3 shows a schematic of the burner on which the various components are identified. The combustion chamber has a square cross section of 46×46 mm, and a brass back wall with a circular plug for the introduction of an ignition torch. The other three walls are fused silica windows (Optico, FS7980; $80 \times 46 \times 3$ mm) to provide optical access. For the current experiments, the adjustable vertical length of the combustion chamber (L in Fig. 4.3) was fixed at 20 mm.

To obtain a planar flame at some height x_f within the chamber, which is as nearly one-dimensional as possible, a uniform supply of the reactants over the cross section is crucial. The bottom reactant, the fuel in this study, is introduced through a diffuser, an initial porous plate, a layer of glass spheres (1 mm dia.), and finally enters the combustion chamber through a 34 mm square porous plate (Mott Metallurgical, 100 μ grade). The high pressure drops insure a good spatial uniformity of the fuel velocity at the porous

4. REALIZATION OF A NEARLY ONE-DIMENSIONAL DIFFUSION FLAME

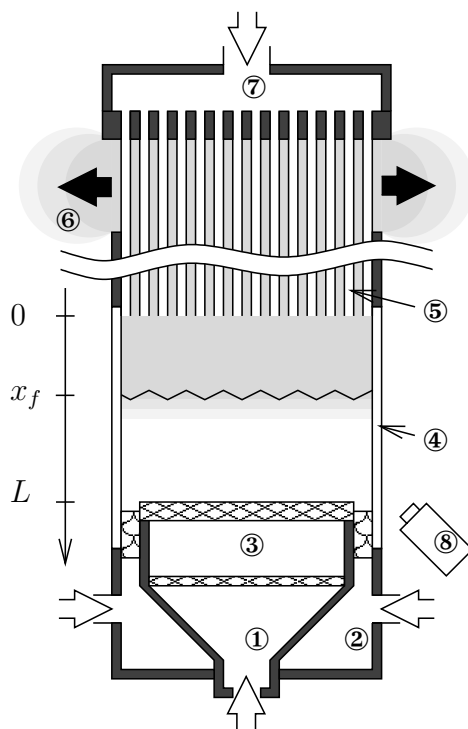


Figure 4.3: Schematic of the Mark I burner. ① bottom fuel flow, ② inert co-flow, ③ porous plates, ④ fused silica windows, ⑤ reactant tube array, ⑥ hot product exhaust, ⑦ oxidizer flow from top, ⑧ movie camera.

plate exit. This part is similar to the porous plug burner, which is commonly used for premixed flame studies. The square plenum for the bottom reactant (label ③ in Fig. 4.3) has an outer dimension of 38 mm and is surrounded by a 4 mm wide channel, which allows the introduction of an inert co-flow. For the first experiments presented here, however, no co-flow was used.

Since the combustion products have to escape upwards from the chamber with a uniform velocity over the entire cross section and the oxidizer supply from the top also needs to be uniform over the cross section, this oxidizer supply and the product exhaust have to penetrate each other. The solution adopted here is to allow non-uniformity on a small scale, with the expectation that it will become negligible near the flame front. In practical terms, the oxidizer is supplied from the top through a Cartesian array of $25 \times 25 = 625$ stainless steel capillaries (Unimed, AISI 304; 1 mm O.D., 0.8 mm I.D.) with

4.3 Design considerations

Proc. Comb. Inst., **30**, 2005 [66], expanded

1.78 mm center-to-center spacing. These 210 mm long hypodermic needles originate from a common top plenum with dimensions of $48 \times 48 \times 22$ mm and, to maintain even spacing, are threaded through a fine wire mesh (G. Bopp & Co, 0.75 mm nominal mesh size, 0.18 mm wire dia.) located about 20 mm above the tube exits. Since the oxidizer supply tubes occupy only 23% of the cross sectional area, the interstitial area is sufficient to allow the hot products to escape from the combustion chamber. As shown schematically in Fig. 4.3, the exhaust first flows vertically up, parallel to the capillaries, and then laterally out between the top end of the burner housing and the bottom of the oxidizer plenum.

Just below the oxidizer injection level at $x = 0$ (see Fig. 4.3), the flow is clearly three-dimensional on the scale of the tube spacing. Since the Reynolds number in the oxidizer mixture supply tubes, based on average velocity and tube I.D., is in the range of about 5–10, i.e. neither small nor large, the thickness of this layer can at this point only be bracketed as follows. In the Stokes flow limit, the “fundamental” of the flow non-uniformity at the upper edge of the combustion chamber, $u(x = 0, y, z) = \hat{u} \cos(2\pi y/s) \cos(2\pi z/s)$, with $s = 1.78$ mm the oxidizer supply tube spacing, is readily shown to decay as $\exp(-2\sqrt{2}\pi x/s)$ for uniform fluid properties, i.e. to less than 1% in one millimeter. On the other hand, one can use the standard similarity solution for a single laminar jet [91] into a *stagnant* fluid to estimate the distance required for the jet diameter to increase from the 0.8 mm supply tube I.D. to the tube spacing s . Assuming again uniform fluid properties, the result is less than one millimeter for the highest Reynolds number. Thus, both low and high Reynolds number estimates show that the thickness of the needle injection layer is less than one needle diameter. The end of this layer constitutes the virtual oxidizer boundary where the concentration appears uniform. To confirm this issue, a numerical simulation for the three-dimensional injection layer have been developed.

The numerical simulation of the 3D-layer was performed with Fluent®, a commercial software. The size of the numerical domain is $15 \times s \times s$ mm and includes, a 5 mm long tube (0.8 mm I.D., 1 mm O.D). The mesh used for the simulation consisted of unstructured triangular cells (≈ 400000), developed with Gambit® a commercial mesh-generator software. The calculation was

4. REALIZATION OF A NEARLY ONE-DIMENSIONAL DIFFUSION FLAME

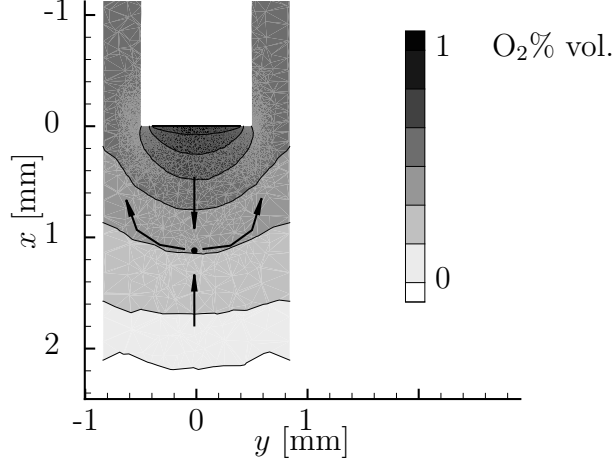


Figure 4.4: Slice of the numerical solution taken at the mid-plane of the computational domain. The field represented in gray level is the O_2 concentration in % vol. near the tube exit. The domain is ranging from -5 to 10 mm in the x -direction. The width of the numerical domain in the y -, and z -direction is of a tube spacing s length. Numerical boundary conditions: oxidizer inlet velocity $\bar{u}_\text{O} = 10 \text{ cm.s}^{-1}$; fuel inlet velocity $\bar{u}_\text{F} = 3 \text{ cm.s}^{-1}$; periodic conditions on the sides ($y = \pm s/2, z = \pm s/2$). The points and the lines represent the stagnation point.

made for pure hydrogen introduced at $x = 10$ mm, at a uniform velocity $\bar{u}_\text{F} = 3 \text{ cm.s}^{-1}$, against pure oxygen introduced at the tube exit ($x = 0$ mm) with a parabolic velocity profile and an average velocity of $\bar{u}_\text{O} = 10 \text{ cm.s}^{-1}$. The mixture exits the numerical domain at $x = -5$ mm. The boundary conditions on the side of the numerical domain ($y = \pm s/2, z = \pm s/2$) are imposed as periodic. The velocity field (not represented here) gives an estimate of about 1 tube diameter for the thickness of the layer.

Below this three-dimensional injection region, the oxidizer is transported towards the flame by one-dimensional diffusion against the product flow, as in the idealized burner discussed in the previous section. This aspect is completely different from the standard counterflow burner where the products are carried away radially from the opposing reactant jets and the resulting planar diffusion flame is necessarily *strained*.

4.4 Experimental characterization of the burner

Proc. Comb. Inst., **30**, 2005 [66], expanded

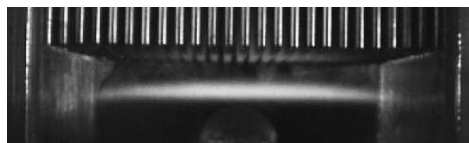


Figure 4.5: Example of a flame side view of 4.348% mass H_2 and 62.92% mass O_2 diluted in CO_2 , $Q_{\text{O}} = 3.33 \times 10^{-5} \text{ m}^3 \cdot \text{s}^{-1}$, $Q_{\text{F}} = 2.83 \times 10^{-5} \text{ m}^3 \cdot \text{s}^{-1}$. The scale is given by tubes of the 1 mm O.D. of the tubes.

Deviations of the steady flame surfaces from planar have not yet been quantified in detail, but Fig. 4.5 gives an impression of the typical flame flatness achieved in the new burner.

4.4 Experimental characterization of the burner

Proc. Comb. Inst., **30**, 2005 [66], expanded

4.4.1 Velocity profiles

In order to obtain velocity profiles, the fuel inlet of the burner was modified. The porous plug was replaced by $14 \times 14 = 196$ stainless steel tubes (Unimed, AISI 304; 3 mm O.D, 2.8 mm I.D.). To ensure a uniform bottom flow the porous plate of Fig. 4.3 was replaced by a 50 mm-long flow straightener preceded by several grids. Figure 4.6 shows several view of the new version of the burner. In addition, the back-side of the burner was modified. To improve the symmetry the original brass back wall with the ignition access was replaced with a fused silica window, identical to the three other windows except for the ignition hole. The modifications are shown to scale on Fig. 4.6, showing the side view, the front view and the cross section of the burner.

Preliminary three-dimensional velocity field measurements were performed in the middle section of the burner, with the LDA described in Sec 2.2.5. Only two components are represented in Fig. 4.7, as the third component was below $0.2 \text{ cm} \cdot \text{s}^{-1}$ everywhere, with measurements made at 5–7 x -positions, with measurements points equally spaced, 2 mm in the y -direction. The number

4. REALIZATION OF A NEARLY ONE-DIMENSIONAL DIFFUSION FLAME

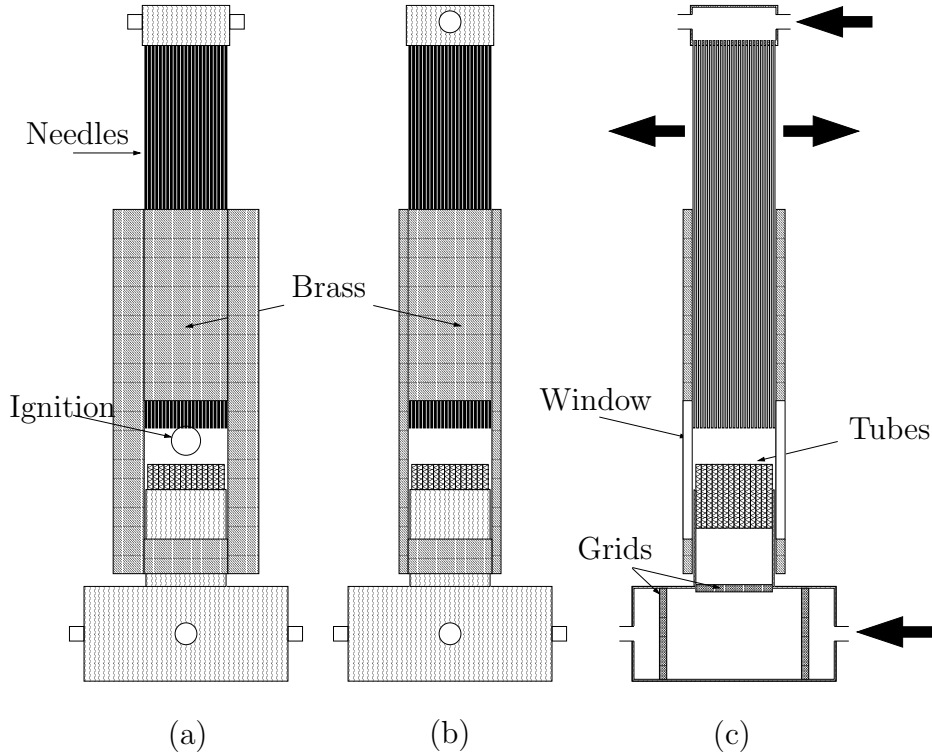


Figure 4.6: One-dimensional Mark Ia burner. (a) Front view; (b) Side view; (c) Cross section of the burner view.

of burst in each direction was fixed at 15000 and the processing of the data was performed with BURSTware software. The traverse used is similar to the one described in Sec. 2.2.3, without the additional correction. Figure 4.7 shows two velocity fields (vectors) corresponding to two conditions. The first condition, at the top of the figure, is the cold condition (air). The flow is uniform except near the tube exit (2-tube diameter), where a divergence of the vectors can be observed. The field represented in gray filled-contour is the dimensionalized strain rate calculated as the traverse gradient of the axial velocity. For the cold condition this strain rate is small ranging from -0.2 to 0.2 s^{-1} . The bottom plot of Fig. 4.7, represents a typical burning regime of 30% H_2 -70% CO_2 reacting with pure oxygen. The flowrate Q_O and Q_F are equal to $3.33 \times 10^{-5} \text{ m}^3 \cdot \text{s}^{-1}$. The strain rate field is ranging from -1.5 to 1.5 s^{-1} . Unfortunately, measurements could not be made above the flame (indicated by the solid line) because of seeding particles sticking on

4.4 Experimental characterization of the burner
Proc. Comb. Inst., 30, 2005 [66], expanded

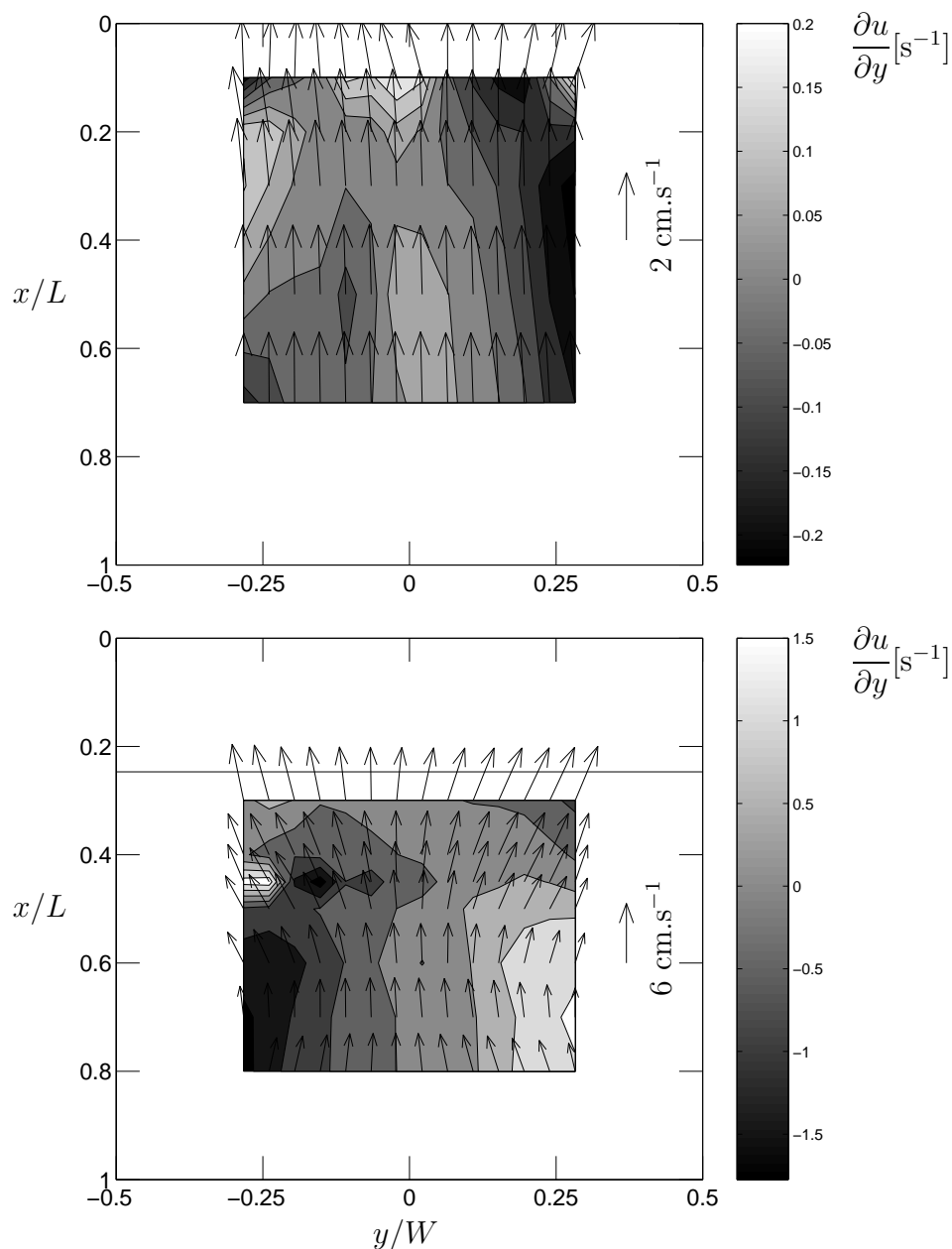


Figure 4.7: Velocity field and associated dimensional strain rate $\partial u/\partial y$ in contour filed. $L = 20$ mm and $W = 46$ mm. Flow rates: $Q_F = Q_O = 3.33 \times 10^{-5} \text{ m}^3.\text{s}^{-1}$ at standard conditions. Top: Cold conditions for air. Bottom: 30% H_2 -70% CO_2 fuel mixture burning in 100% O_2 vol. The solid line represents the flame position, $x_f = 4.94$ mm.

4. REALIZATION OF A NEARLY ONE-DIMENSIONAL DIFFUSION FLAME

the wall. These preliminary results show two interesting behaviors. The non-uniformity of the velocity field suggests that heat loss through the walls is important. This observation will be confirmed with temperature profiles presented in the next section. Nevertheless, the strain rate obtained is small, compared to typical counterflow burners (10 s^{-1} for the lowest). Han *et al.* [35] obtained a strain rate of about 1.5 s^{-1} which is low too, however, reduction of our residual strain to zero is not impossible since gravity does not break the symmetry of our design.

4.4.2 Temperature and heat loss consideration

The temperature profiles were made with type K thermocouples (Omega, 0.25 mm diameter) connected to a multi-channel thermocouple monitor (Stanford Research Systems, SR636). These thermocouples were 200 mm long, this length was long enough to perform temperature measurements from the top in-between the injection needles, and from the bottom through the grids and the flow straightener. Taking the two profiles were necessary because of the bias on the temperature measurement due to heat loss from conduction. However, without any radiation correction, the temperature profiles give a good estimate of the heat loss through the windows of the burner. The position measurements of each thermocouple were made with a digital height gauge (Trimos, mini-vertical) with a magnifying scope (f10/25X). Figure 4.8 shows several temperature profiles, those coming from the top and the bottom at the center of the burner ($\hat{y} = Y/W = 0$), those coming from the top and the bottom on the side of the burner ($\hat{y} = 0.5$) and the one taking the temperature on the outside surface of the burner window ($\hat{y} = 0.5^+$).

The difference at the flame position for the center profile and the side profile is important. Nearly half of the temperature is observed between the center of the flame and the temperature at the window. This creates temperature gradient inducing changes on the flow field.

The temperature difference across the window is about 100 K, the thermal conductivity of the window is estimated to be $\lambda_w = 1.67 \text{ W/m.K}$ [112]. A rapid estimate of the heat flux through the window can be made with the Fourier law, $q_w = \lambda_w dT/dx \approx \lambda_w \Delta T/e$, with $e = 3 \text{ mm}$ the thickness

4.4 Experimental characterization of the burner

Proc. Comb. Inst., **30**, 2005 [66], expanded

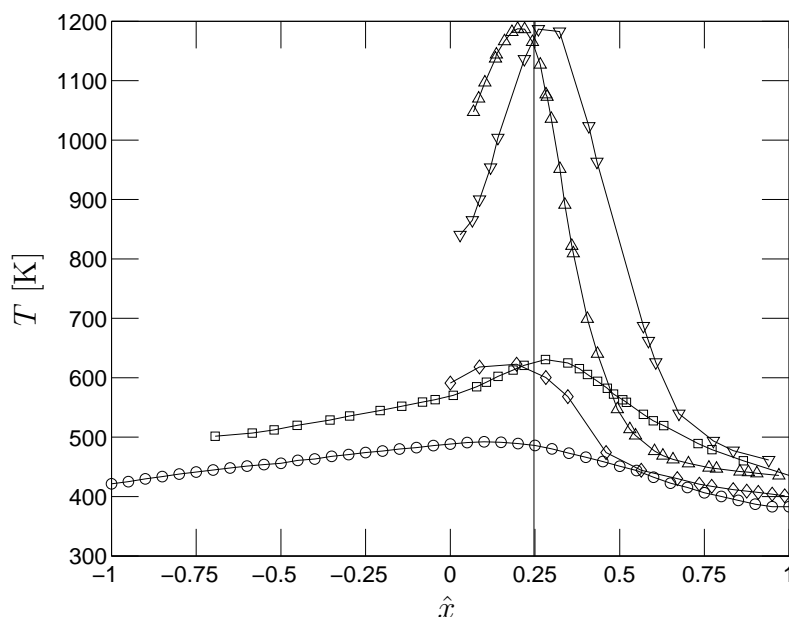


Figure 4.8: Thermocouple profiles at several locations without radiative correction, for 30% H₂-70% CO₂ fuel mixture burning in 100% O₂ vol. [—Δ—]: Thermocouple originating from bottom, at the center of the burner $\hat{y} = 0$; [—▽—]: thermocouple originating from top, at the center of the burner $\hat{y} = 0$; [—□—]: thermocouple originating from top, at the side of the burner, $\hat{y} = 0.5$; [—◇—]: thermocouple originating from bottom, at the side of the burner, $\hat{y} = 0.5$; [—○—]: thermocouple outside at the side of the burner, $\hat{y} = 0.5^+$; the solid line at $\hat{x} \approx 0.25$ is the flame position.

of the window, resulting in 56 kW/m². Thus, for a 1 cm high strip of window surrounding the flame, there will be a total heat loss of about 110 W, which represents approximately 3.6% of the thermal power produced by the flame. Assuming 2.86 kJ/g for the heat of combustion, 30% H₂-70% CO₂ fuel mixture flowing at 2 sl/min.

4.4.3 Flame position measurements

The flame position x_f , measured from the ends of the oxidizer injection tubes, was taken to be the center of the visible luminous zone in the dark laboratory. A digital height gauge (Trimos, mini-vertical) with a magnifying scope (f10/25X) was used to measure x_f with a resolution of 0.01 mm. From repeated measurements, the overall uncertainty in x_f , was estimated at about

4. REALIZATION OF A NEARLY ONE-DIMENSIONAL DIFFUSION FLAME

± 0.2 mm. The temperature T^e of the exhaust gases near the capillary tube exits was measured with a type K thermocouple (Omega, 0.25 mm diameter) connected to a multi-channel thermocouple monitor (Stanford Research Systems, SR636).

To characterize the burner, the position x_f of steady flames and the exhaust temperature near $x = 0$, i.e. at the level of the oxidizer injection, were measured for different H₂-CO₂ and O₂-CO₂ reactant mixtures as well as oxidizer and fuel flowrates. Eighteen data sets for nine different reactant compositions have been acquired by fixing the oxidizer flowrate Q_O through the hypodermic needle manifold to either 3.33×10^{-5} or 5.00×10^{-5} m³.s⁻¹, and varying the fuel flowrate Q_F . These data sets are reported in Table 4.1, where the two vertical partitions correspond to the two fixed oxidizer flowrates used in this study. The first column defines the nine different combinations of initial fuel and oxidizer mixtures by specifying the respective H₂ and O₂ volume percent in CO₂. The second column gives the corresponding mass-based initial mixture strength ϕ_m , which is defined as the ratio of the H₂ and O₂ mass fractions supplied in the fuel and oxidizer streams, respectively, normalized by the stoichiometric ratio. The third and seventh columns specify the minimum and maximum fuel mixture flowrate Q_F used for each data set, i.e. for each combination of reactant mixtures and Q_O , while the corresponding range of measured flame positions x_f is given in the following columns. In columns five and nine, the range of exhaust temperatures T^e , measured near the chamber center, corresponding to the range of Q_F is reported. The total uncertainty of the reported temperatures, which were not corrected for radiation and conduction losses, is estimated at less than 2 K for the experimental conditions studied. The last columns six and ten list the range of diffusivity \mathcal{D}_O^e of oxygen into a *representative composition* of H₂-CO₂, calculated at the corresponding exhaust temperatures T^e [46]. The *representative composition* for the diffusion coefficient \mathcal{D}_O^e was estimated by taking into account the mass flux of the initial O₂-CO₂ mixture injected through the hypodermic needle manifold, the mass flux of CO₂ from the bottom porous plug, and by assuming that the H₂ is completely converted to water.

To compare the behavior of the present burner with that of the idealized burner discussed in the introduction (e.g. [53, 69]), the measured x_f is com-

System			$Q_O = 3.33 \times 10^{-5} \text{ m}^3 \cdot \text{s}^{-1}$				$Q_O = 5.00 \times 10^{-5} \text{ m}^3 \cdot \text{s}^{-1}$			
Symb.	H ₂ -O ₂ [% vol.]	ϕ_m	$Q_F \times 10^{-5}$	$x_f \times 10^{-3}$	T^e	$\mathcal{D}_O^e \times 10^{-4}$	$Q_F \times 10^{-5}$	$x_f \times 10^{-3}$	T^e	$\mathcal{D}_O^e \times 10^{-4}$
			[m ³ ·s ⁻¹]	[m]	[K]	[m ² ·s ⁻¹]	[m ³ ·s ⁻¹]	[m]	[K]	[m ² ·s ⁻¹]
★	30-50	0.36	2.50	2.70	831	1.13	2.83	2.74	859	1.22
			3.33	3.94	917	1.34	4.16	4.18	975	1.51
■	50-50	0.82	1.83	2.90	842	1.16	1.83	3.66	843	1.18
			2.50	4.42	990	1.53	2.66	5.35	988	1.55
◆	30-70	0.24	3.00	2.85	870	1.22	3.50	3.12	910	1.34
			4.16	4.15	977	1.49	4.66	4.28	1002	1.58
▲	50-70	0.55	2.00	3.70	853	1.19	2.16	4.43	853	1.20
			2.83	5.54	1008	1.57	3.00	6.09	1005	1.59
✱	30-100	0.15	3.33	3.33	888	1.27	3.33	4.10	880	1.27
			4.66	4.94	998	1.54	4.66	5.70	983	1.53
▼	50-100	0.35	2.33	4.70	903	1.31	2.66	5.35	938	1.42
			3.00	5.90	998	1.55	3.33	6.64	1023	1.64
▶	50-30	1.46	1.33	1.94	803	1.07	1.50	2.28	823	1.13
			1.83	3.30	906	1.32	2.33	3.98	979	1.53
●	70-30	3.23	1.16	1.12	873	1.24	1.16	2.24	833	1.16
			1.66	2.72	973	1.49	1.83	4.15	1002	1.59
◀	70-50	1.82	1.50	2.84	898	1.30	1.66	3.62	912	1.35
			2.00	4.25	1007	1.58	2.16	4.95	1016	1.63

Table 4.1: Range of conditions for flame position measurements. For each initial reactant mixture investigated, the minimum and maximum parameter values are reported.

4. REALIZATION OF A NEARLY ONE-DIMENSIONAL DIFFUSION FLAME

pared to the theoretical prediction for a one-dimensional, unstretched planar diffusion flame [12]. Under the simplifying assumption of constant transport properties (constant thermal conductivity, viscosity, specific heat at constant pressure, and $\rho\mathcal{D}_k$, where ρ is the local mixture density and \mathcal{D}_k the binary diffusion coefficient of species k), an explicit Burke–Schumann solution⁴ has been developed [12] for the relation between the flame position and system parameters:

$$x_f = \frac{\rho\mathcal{D}_O}{m_F} \ln(1 + \phi_m^{-1}) , \quad (4.17)$$

where m_F is the mass flux [kg/(m.s)] of the H₂-CO₂ mixture through the bottom porous plug, and the other quantities are defined earlier in this section (cf. also Table 4.1).

Guided by this analysis, the experimentally determined flame position x_f , is normalized as $\tilde{x}_f = (x_f m_F)/(\rho_O^e \mathcal{D}_O^e)$, where m_F is the mass flux of the H₂-CO₂ mixture from the porous plug, ρ_O^e the density of the O₂-CO₂ mixture at the measured exhaust temperature T^e , and \mathcal{D}_O^e the calculated binary diffusion coefficient of oxygen into the product gases at T^e (see above description associated with Table 4.1).

To compare with the idealized burner, the \tilde{x}_f corresponding to the eighteen data sets of Table 4.1 are plotted against $\ln(1 + \phi_m^{-1})$ in Fig. 4.9. The open and solid symbols in this figure correspond to the oxidizer flowrates of $Q_O = 3.33 \times 10^{-5}$ and $Q_O = 5.00 \times 10^{-5} \text{ m}^3 \cdot \text{s}^{-1}$, respectively. The solid line represents the ideal relationship of Eq. (4.17) and the dashed lines are separate linear fits, forced through the origin, for the two Q_O conditions. Despite the differences between the ideal theoretical model and experiments, the first observation drawn from Fig. 4.9 is that the theoretical and measured nondimensional flame positions \tilde{x}_f are both linearly correlated with $\ln(1 + \phi_m^{-1})$. However, the experimental standoff distance \tilde{x}_f is dependent on the oxidizer flow rate. Depending on the flow rate, \tilde{x}_f is either larger or smaller than the theoretical value $\tilde{x}_{f,\text{ideal}} = \ln(1 + \phi_m^{-1})$. The difference between the ideal and the measured standoff distance is denoted by $\tilde{\Delta}$.

One is tempted to identify the difference $\tilde{\Delta}$ with the non-dimensional

⁴For large activation energy, this solution is relevant even for incomplete combustion including conditions approaching extinction, as it represents the leading order term of an expansion in inverse powers of the activation energy [12].

4.4 Experimental characterization of the burner
Proc. Comb. Inst., **30**, 2005 [66], expanded

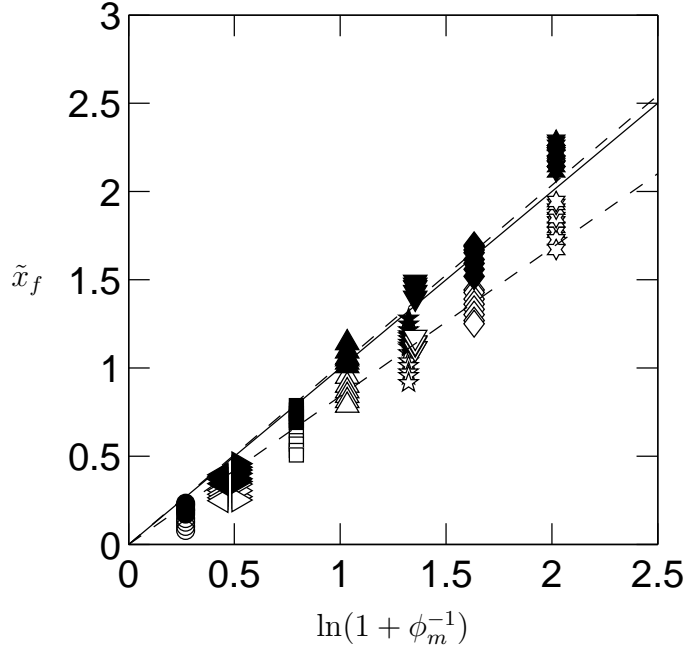


Figure 4.9: Flame position $\tilde{x}_f = x_f(m_F/\rho^e \mathcal{D}_O^e)$ as a function of $\ln(1 + \phi_m^{-1})$ for the data sets of Table 4.1. [—]: Theoretical line for a simplified one-dimensional unstrained planar flame [12]. Open symbols: $Q_O = 3.33 \times 10^{-5} \text{ m}^3 \cdot \text{s}^{-1}$; filled symbols: $Q_O = 5.00 \times 10^{-5} \text{ m}^3 \cdot \text{s}^{-1}$. [- -]: Separate fits through open and filled symbols.

thickness of the three-dimensional injection layer below the ends of the oxidizer supply tubes, and to conclude that $\tilde{x} = \tilde{\Delta}$ represents the virtual origin of one-dimensional downward diffusion of oxidizer against the upward exhaust flow. The observation (cf. Fig. 4.9) that, for any fixed ϕ_m and Q_F , $\tilde{\Delta}$ increases with increasing oxidizer injection rate Q_O is consistent with this view. However, the situation is not as simple. On the theoretical side, the analysis leading to Eq. (4.17) assumes constant transport properties. The measured exhaust temperature T^e at $x = 0$, however, can be up to three times higher than the fuel inlet temperature. Furthermore, since the binary diffusion coefficient of real gases increases approximately as $T^{1.8}$ [46], the variation of the physical properties with temperature is significant. If the temperature dependence of the transport properties is taken into account, a refined analysis of the idealized burner yields an increase of $\tilde{x}_{f,\text{ideal}}$ beyond

4. REALIZATION OF A NEARLY ONE-DIMENSIONAL DIFFUSION FLAME

its value given by Eq. (4.17), i.e. $\tilde{x}_{f,\text{ideal}} > \ln(1 + \phi_m^{-1})$. In other words, a part of $\tilde{\Delta}$ in Fig. 4.9 is due to the oversimplified theoretical analysis.

Since the calculated \mathcal{D}_O^e value in Table 4.1 is sensitive to the variation of both mixture composition and temperature, the uncertainties associated with \mathcal{D}_O^e are difficult to quantify. Since complete temperature profiles across the flame have not been measured, it is difficult to determine if the measured exhaust temperature is the appropriate reference temperature for the evaluation of transport properties. The variation of \mathcal{D}_O^e with the mixture composition must also be considered. If the representative mixture for the calculation of \mathcal{D}_O^e was taken to be the total initial reactant mixture (H_2 , O_2 , and CO_2) instead of the representative product mixture, for example, the \mathcal{D}_O^e in Table 4.1 would increase by as much as 20% in some cases which would shift the experimental points in Fig. 4.9 downwards. However, the measured x_f values in Table 4.1 strongly suggest that the transport of oxygen to the flame is mostly directed by diffusion against the upwards product flow.

Chapter 5

First investigation of cell formation in the new burner

5.1 Introduction

Idealized unstrained, planar non-premixed flames have been the object of numerous theoretical and numerical investigations. Spalding and Jain [104], for example, examined the effect of finite-rate chemistry and temperature-dependent fluid properties. Kirkby and Schmitz [53] examined the stability of this unstrained flame to infinitesimal one-dimensional disturbances. Their numerical results showed that a “pulsating” instability is possible in the presence of heat losses (non-adiabatic systems) or when the reactant Lewis numbers exceed unity. Using activation-energy asymptotics, Matalon *et al.* [69] determined the unburned fuel fraction (fuel leakage through the flame) as a function of the constant fuel flow rate for the whole range of Damköhler numbers. More recent work was directed towards thermo-diffusive instabilities, and both pulsation [59] and cellular modes [12,49] have been analyzed. These latter investigations revealed the influence of both reactant Lewis numbers, heat loss, and the initial mixture strength on these thermo-diffusive instabilities as well as the requirement of a relatively low Damköhler number (near extinction conditions) for their appearance. Cheatham and Matalon [12], for example, demonstrated that the propensity for the formation of cells increases with increasing heat loss and decreasing reactant Lewis numbers,

5. FIRST INVESTIGATION OF CELL FORMATION IN THE NEW BURNER

Damköhler number, and the initial mixture strength.

Some notable experimental investigations on cell formation in non-premixed flames include the works of Dongworth and Melvin [22] who observed cells at the base of a diluted H₂-O₂ diffusion flame, and Chen *et al.* [13] who clearly demonstrated the importance of relatively low Lewis and Damköhler numbers in a Wolfhard–Parker burner. More recent experimental work at EPFL has confirmed the influence of the initial mixture strength on cell formation in an axisymmetric jet flame [26,67]. Since these experiments can only be qualitatively related to the stability theories of idealized flames, the current attempt was made to experimentally realize, as closely as possible, the *unstretched* one-dimensional planar non-premixed flame assumed to exist in the idealized theoretical model mentioned above. To the authors' knowledge, this work is the first such attempt.

To explore the potential of the new burner, the formation of cellular structures in CO₂-diluted H₂/O₂ flames near the extinction limit has been investigated. Due to the nearly unstrained flame produced in the new burner, the comparison of the current investigation with a similar recent study in an axisymmetric jet flame [67] represents a first step towards a better understanding of cell formation in the absence of strain.

5.2 Preliminary results

Proc. Comb. Inst., **30**, 2005 [66]

The parameter space near the extinction limit was investigated by holding the oxidizer composition (O₂-CO₂ mixture) constant, and varying the H₂ concentration in the bottom fuel stream (H₂-CO₂ mixture). For all the experiments reported in this section, the oxidizer supply was fixed at $Q_O = 3.33 \times 10^{-5} \text{ m}^3 \cdot \text{s}^{-1}$, while the oxygen concentration was varied in the range of 10.6–100% mass (14.0–100% vol.). For each oxidizer mixture studied, the cell formation boundary and the extinction limit were identified by gradually decreasing the hydrogen concentration in steps of 0.2 and 0.1% vol. close to extinction. In terms of reactant Lewis numbers based on the overall reactant mixture at 300 K, the experiments cover the range of 0.97–1.33 for

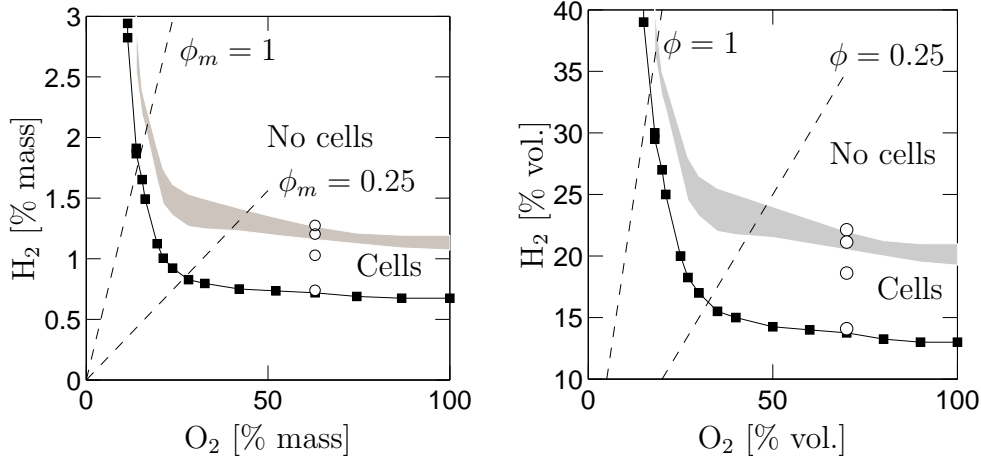


Figure 5.1: Near-extinction limit and cellular instability boundaries observed for nearly unstrained planar non-premixed CO₂-diluted H₂-O₂ flames; $Q_O = 3.33 \times 10^{-5} \text{ m}^3 \cdot \text{s}^{-1}$. Shaded region: transition region from non-cellular flames to cellular structures throughout the entire flame; [—■—]: near-extinction limit; [○]: conditions for Fig. 5.2.

oxygen and 0.22–0.29 for hydrogen. In terms of initial mixture strength, the range $0.05 < \phi_m < 3.55$ is covered. The results are shown in Fig. 5.1 in terms of the initial O₂ and H₂ concentrations, with two lines of constant ϕ_m added for reference.

The solid squares in this figure mark the reactant compositions at the “near-extinction” limit. For the current study, the flame was considered extinct when it consisted of less than 3 small cell structures or flame “patches”, corresponding to a total flame area of less than 0.2% of the burner cross section. The extinction curve in Fig. 5.1 has two asymptotes for the limiting hydrogen and oxygen concentrations. Irrespective of the composition of the other reactant, a diffusion flame could not be established below a limiting H₂ concentration of 0.65% mass (12.6% vol.) or a O₂ concentration of 10.60% mass (14.0% vol.). These limiting concentrations are lower than the values in the axisymmetric jet flame experiments [67], where limiting values of 0.94% mass (17.3% vol.) H₂ and 13.77% mass (18.0% vol.) O₂ were reported. These significant differences are at least partially attributable to the negligible flow strain rate in the current facility.

5. FIRST INVESTIGATION OF CELL FORMATION IN THE NEW BURNER

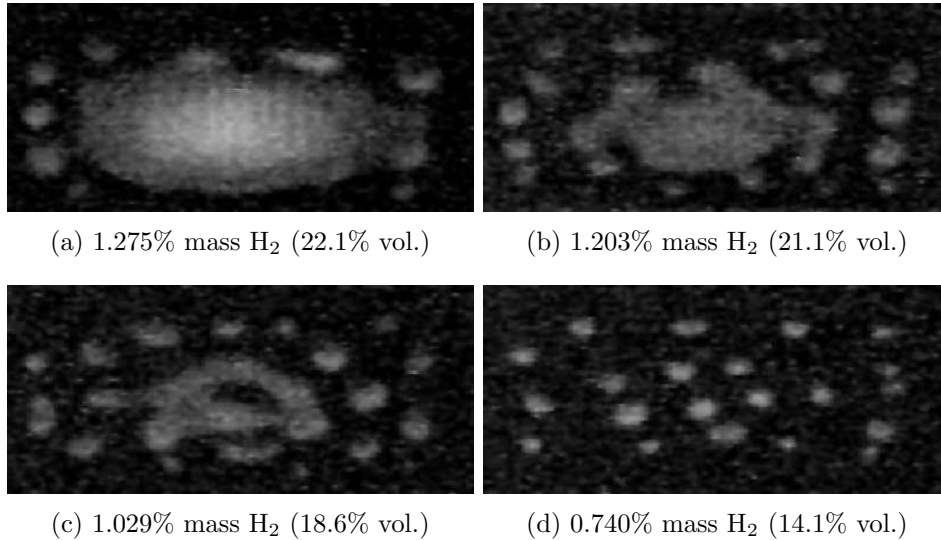


Figure 5.2: Digital images taken, at an oblique angle as indicated in Fig. 4.3, of the cells observed at the four points [O] in Fig. 4.9 ($Q_O = 3.33 \times 10^{-5} \text{ m}^3 \cdot \text{s}^{-1}$, $Q_F = 3.00 \times 10^{-5} \text{ m}^3 \cdot \text{s}^{-1}$). (a)–(c): Transition from no cells to the fully cellular regime; (d): near the extinction limit.

In Fig. 5.1, the transition region from a steady “featureless” flame to a flame with cells over its entire surface is identified by shading. As in previous work [67], the range of concentrations in the parameter space where cells are observed is shown to increase with decreasing initial mixture strength; in other words, the distance between the cell transition region and the extinction boundary increases with decreasing ϕ_m .

To illustrate the transition process to a fully cellular flame, Fig. 5.2 shows digital images taken for various conditions corresponding to the open circles in Fig. 5.1. The oxidizer mixture for these images was fixed at 62.92% mass O₂, and the reactant flowrates are given in the figure caption. The digital images were taken with a movie camera (Sony, DSR 300P) at an oblique angle of about 45 degrees with respect to the vertical (cf. Fig. 4.3).

The first image, Fig. 5.2(a), corresponds to a 1.275% mass H₂ fuel mixture. At this condition, the cell formation starts at the flame edges adjacent to the chamber walls. The linear cell dimensions at this condition are about 2–5 times the spacing $s = 1.78 \text{ mm}$ of the oxidizer supply tubes and cells are

not spatially locked to the tube grid. As the H₂ concentration is reduced to 1.203% mass H₂ in Fig. 5.2(b), the cellular region grows towards the center of the flame. At 1.029% mass H₂ in Fig. 5.2(c), the entire flame consists of cells and the transition to the fully cellular regime in Fig. 5.1 is considered complete. At this point, the cell structures (flame “patches”) are not stationary. They appear to be generated near the flame center, travel outwards, and then sometimes move along the chamber walls before vanishing. As the H₂ concentration is reduced further, the number of cells populating the flame region decreases progressively until the extinction limit is reached. Figure 5.2(d) shows an image at 0.740% mass H₂ which is close to the extinction limit. The cell sizes at this condition are up to 2 times larger than the tube spacing s . Therefore, the cell size over the entire cellular regime is believed to be unrelated to the spacing of the oxidizer supply tubes.

Additional experiments were conducted to investigate the sensitivity of the near-extinction limit and the cellular regime boundary in Fig. 5.1 to changes of the fuel and oxidizer flowrates, Q_F and Q_O . For the conditions shown in Fig. 5.1, extinction experiments were performed for Q_F and Q_O in the range of $1.67\text{--}4.17 \times 10^{-5}$ and $2.50\text{--}6.67 \times 10^{-5}$ m³.s⁻¹, respectively. As described before, extinction was found by gradually decreasing the H₂ concentration in decrements of 0.1% vol. Over the range of flowrates studied, the hydrogen concentration at the near-extinction limit was found to vary by less than 0.5% vol., i.e. to be essentially insensitive to flowrate changes. Hence, the 0.5% vol. variation can be considered to be the uncertainty of the H₂ concentration at the near-extinction in Fig. 5.1.

For fixed initial reactant concentrations and upper oxidizer flowrate, the highest bottom fuel flowrate was limited by the requirement of not pushing the flame too close to the oxidizer injection tubes. Since the extinction limits were not found to vary significantly with flowrate, and consequently stand-off distance, heat loss to the oxidizer injection manifold is not expected to be significant for the conditions investigated. Although the heat loss from the flame is difficult to quantify, one would expect that the flame-edges near the chamber walls experience a relatively higher heat loss, i.e. burn at a lower effective Damköhler number than the center of the flame. Therefore, heat loss is a possible explanation for the observation that in the *current configuration*

5. FIRST INVESTIGATION OF CELL FORMATION IN THE NEW BURNER

cells always appear first at the flame-edges. Since other explanations, such as non-uniformity caused by the unused co-flow slot around the fuel supply plug, are possible, further studies are required to clarify the issue.

Since the flow in the current apparatus is very close to one-dimensional, and cells appear in the same horizontal plane, the effects of buoyancy are not significant for the current experiments, see additional discussion in Sec. 5.4. There was no visual evidence of convective cells in the flowfield for the current flame experiments.

Discussion and conclusions

In the experiments reported here, the fuel was transported upwards to the flame in direction of the bulk velocity, while the oxygen diffused against the bulk flow to the flame front. The situation is analogous in the *steady* axisymmetric fuel jet flame, where the radial bulk flow through the flame is directed outwards from the fuel to the oxidizer side (cf. [32]). The same situation is also found in a “lean” flamelet, i.e. a small locally flat segment of a relatively large non-premixed flame. A prototype of a flamelet [85] is the strained planar flame front in a counterflow configuration. For opposed jet flames of highly diluted fuel, such as N_2 -diluted CH_4 burning with pure O_2 (e.g. [23]), the flame zone lies on the fuel side of the stagnation plane, and the O_2 reaches the flame by counterdiffusion as in the current experiments.

Previous theoretical studies [12, 59, 60] have shown that the reactant convected through the flame zone plays a significant role in determining the conditions for thermo-diffusive instabilities in non-premixed flames. When O_2 diffuses against the bulk flow, the current study and others (cf. [67]) have shown that cellular instabilities are more prevalent at low initial mixture strength and Lewis numbers, in agreement with theoretical predictions [12]. At this point it is interesting to consider the opposite situation, i.e. the counterdiffusion of *fuel* instead of oxygen. The theoretical studies cited above demonstrate that the effect on thermo-diffusive instabilities is major. Cells, for example, would become more prevalent at *high*, rather than low, initial mixture strength. For the flame position, the simplified theory [12] again yields Eq. (4.17), but with $\rho\mathcal{D}_\text{O}$ replaced by $\rho\mathcal{D}_\text{F}$. The new burner, which has

been shown to produce an essentially one-dimensional planar non-premixed flame with virtually no strain, appears to be the only possibility to test these theories. The experiment can be implemented relatively easily by interchanging the reactant supplies, i.e. by supplying the oxidizer through the bottom porous plug and the fuel through the upper hypodermic needle manifold. Preliminary experiments on this “reverse configuration” are presented in the next section (Sec. 5.3), and the dependence of pattern formation on the initial mixture strength is being examined. In addition to satisfying scientific curiosity, these future experiments may have some bearing on the dynamic extinction of “flamelets”.

Published comments

James G. Quinterie, University of Maryland, USA. Your experiment can be thought of as a representation of the ideal 1-D stagnant layer diffusion burning rate problem (for liquids or simple solids). Have you considered this connection?

Author’s reply. The objective of our experiment was to realize a planar unstrained diffusion flame. The bulk flow in our experiment is directed always upwards and hence our configuration does not correspond to an ideal 1-D stagnant layer in which both the fuel and oxidizer are brought together purely by diffusion. Now that we have demonstrated for the first time that it is possible to introduce one of the reactants (the oxidizer in this work) to the flame purely by diffusion, it is perhaps possible to modify the configuration and produce a diffusion flame in a 1-D stagnant layer. This modification will require both reactants to be introduced through hypodermic tube manifolds similar to the top manifold of the current experiment. In this way, both reactants would reach the flame through counterdiffusion and the bulk flow would be zero. We have given some thought to such a modification of our burner, but it is not yet clear whether all design problems can be resolved.

Alfonso F. Ibarreta. Case Western Reserve University, USA. How accurate is it to call your flame an “unstretched” diffusion flame? As mentioned

5. FIRST INVESTIGATION OF CELL FORMATION IN THE NEW BURNER

in your presentation there is a small but finite strain rate. For the limit of zero stretch, the diffusion flame thickness should go to infinity. This limit can thus never be achieved. It would be better to designate your flame as a “low stretch” or “ultra-low stretch” flame.

Author’s reply. All the presented evidence supports our claim that the flame is planar and that the flow is essentially uniform and unidirectional near the flame. As stated in the oral presentation, accurate measurements of the flowfield have been carried out very recently. For these experiments, the bottom porous plug was replaced by a closely packed bundle of 3 mm O.D. hypodermic needles (about 50 mm in length) to allow the introduction of solid particles for laser Doppler velocimetry. These preliminary measurements show the strain rate (the transverse gradient of vertical velocity) is less than 1 s^{-1} , i.e., is indeed “ultra-low” as stated in the comment (see Sec. 4.4.1). The “residual” strain, which results from non-uniformities due to heat losses to the chamber walls, can be minimized with proper heat loss management (see Sec. 4.4.2). Furthermore, gravity imposes no limit on the further reduction of strain, as fluxes can be perfectly aligned with the gravity vector. Therefore we maintain the reduction of the residual strain to ZERO (within experimental error, of course!) is not impossible, thus justifying the term “unstretched diffusion flame” we have used. Finally, the variation of the flame thickness with the inverse square root of the strain rate applies to a strained flame such as in a counterflow configuration, and does not hold for unstrained flame such as the one realized in our burner.

S. Candel, EM2C Lab. CNRS, Ecole Centrale Paris, France. Your theoretical analysis is based on the assumption that $\rho\mathcal{D} = \text{constant}^*$ while the more standard approach uses $\rho^2\mathcal{D} = \text{constant}^*$. The last assumption might give a better description of the flame structure.

*Using unequal diffusivities for the fuel and oxidizer

Author’s reply. Whether $\rho\mathcal{D}$ or $\rho^2\mathcal{D}$ is assumed constant in theoretical studies is a choice made solely for mathematical convenience. The diffusion term in the mass balance equation for a given species contains the nonlinear

5.2 Preliminary results

Proc. Comb. Inst., **30**, 2005 [66]

term $\nabla(\rho\mathcal{D}\nabla Y)$ where \mathcal{D} is the molecular diffusivity that depends in general on temperature. It is advantageous, for mathematical simplification, to replace this term with $\rho\mathcal{D}\nabla^2 Y$ by assuming $\rho\mathcal{D} = \text{const}$. When a density weighted coordinate is introduced in the analysis (usually in order to reduce the governing equations to an incompressible form), an additional ρ appears in front of $\rho\mathcal{D}$ from the coordinate transformation; linearization then requires introducing the assumption $\rho^2\mathcal{D} = \text{const}$. This issue, however, is irrelevant since, as noted in the oral presentation, we have extended the theory to accommodate for an arbitrary dependence of the diffusivity on temperature. This generalization includes the choice of $\rho\mathcal{D}$ or $\rho^2\mathcal{D}$ being constant. As noted, the physically realistic choice $\rho\mathcal{D} \sim T^{0.7}$ leads to a description of the flame structure that is more consistent with the experimental data.

5. FIRST INVESTIGATION OF CELL FORMATION IN THE NEW BURNER

5.3 Additional comments on the reverse configuration

Foreword A part of this section was presented at the 21st International Congress of Theoretical and Applied Mechanics (ICTAM) [65].

Previous experimental investigations on cell formation in non-premixed flames include the work of Chen *et al.* [13] who clearly demonstrated that low Lewis and Damköhler numbers are required for cells formation. More recently, the influence of the initial mixture strength on cell formation in an axisymmetric jet flame has been documented at EPFL [26,67]. While these studies qualitatively confirm the influence of the different parameters predicted theoretically for an ideal 1-D flame, the new burner described above should permit quantitative comparisons. In the following, preliminary results with the new burner are reported for CO₂-diluted H₂-O₂ *nearly unstrained*, non-premixed flames near extinction. Two configurations are considered: One with the fuel supplied from the bottom (FB) and the oxidizer counter-diffusing from the top, and the configuration with inverted supplies, i.e. the fuel counterdiffusing from the top (FT). Note that the FB configuration is analogous to the steady axisymmetric jet flame, where the radial bulk flow through the flame is directed outwards from the fuel to the oxidizer side. The same situation is also found in a “lean” flamelet. Finally, for opposed jet flames with highly diluted fuel (e.g. N₂-diluted CH₄ burning with pure O₂ [23]), the flame sits on the fuel side of the stagnation plane and O₂ reaches the flame by counterdiffusion, again as in the FB configuration.

First, the extinction limit for the FB and FT configurations were determined as a function of the initial O₂ and H₂ concentrations. For this, the top reactant composition was held constant, while the bottom reactant concentration was gradually decreased in small steps until the flame could barely be maintained (a further 0.1% reduction of the bottom reactant concentration below this “near-extinction” limit always resulted in complete extinction). As shown in Fig. 5.3, these extinction curves have asymptotes corresponding to limiting H₂ and O₂ concentrations, below which a diffusion flame cannot be established, irrespective of how “rich” the other reactant is. The influ-

5.3 Additional comments on the reverse configuration

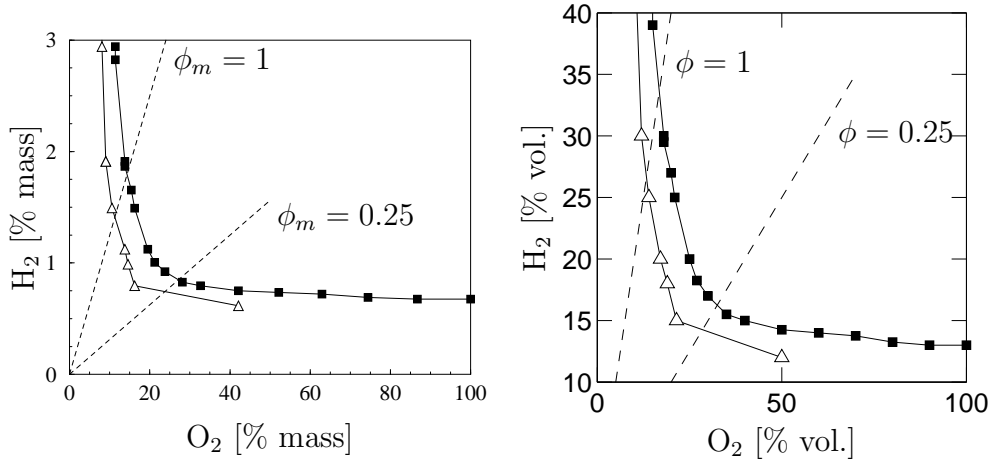


Figure 5.3: Near-extinction limits observed in nearly unstrained planar non-premixed CO₂-diluted H₂-O₂ flames; [—■—]: FB near-extinction limit; [—△—]: FT near-extinction limit.

ence of the direction of bulk flow on the limiting O₂ concentration is evident: when O₂ is supplied convectively by the bulk flow (FT configuration), a flame with excess fuel supply can be sustained at about 5% less O₂ concentration than in the FB configuration, where O₂ has to diffuse against the bulk flow. The comparison of the limiting H₂ concentrations, on the other hand, has not yet been carried out. Furthermore, it is noted that all the limiting concentrations in Fig. 5.3 are significantly lower than in the axisymmetric jet flame [67], which is believed to be at least partly due to the negligible flow strain rate in the present burner. Other effects, such as heat loss, remain to be investigated: for any given reactant composition, the flowrate of the bottom reactant had to be limited keep the flame away from the upper injection manifold. The limit where heat loss to this manifold affects the extinction limits, however, remains to be determined.

Next, the parameter space in which cellular flames are observed was determined for the *FB configuration only*. For the limited conditions examined to date in the FT configuration, no cells have been found yet.

5. FIRST INVESTIGATION OF CELL FORMATION IN THE NEW BURNER

Outlook

Theoretical studies [12, 59, 60] have shown that the reactant convected to the flame zone has a significant influence on the conditions for thermo-diffusive instabilities in non-premixed flames. When O₂ diffuses against the bulk flow (our FB configuration), the current study and others (cf. [67]) have shown that cellular instabilities are more prevalent at low initial mixture strength and Lewis numbers, in agreement with theoretical predictions. In the opposite FT configuration, theory predicts that *high* initial mixture strength promotes cell formation. In addition, as opposed to the FB configuration, a low O₂ Lewis number would be more important for cell formation than a low H₂ Lewis number. The new burner, which has been shown to produce an essentially 1-D planar non-premixed flame with virtually no strain, appears to be well suited to test these theories. As mentioned above, no cells have so far been observed near the FT extinction limit in Fig. 5.3, despite the high ϕ_m . The next step will therefore consist in lowering the oxidizer Lewis number and minimizing the effects of heat loss.

5.4 Comments on possible thermal-convection

In the 1-D burner, the flame produces a hot layer of fluid and the question arises whether the development of cellular instability is possibly related to thermal convection above the flame. The classical setup with a hot rigid (non-permeable) boundary below and cold rigid boundary can lead to the Rayleigh–Bénard instability [4, 55, 89]. The literature on this subject is abundant, and a complete review is beyond the scope of this discussion. The goal of this section is to present the literature on convection instability with a vertical *throughflow*.

In the classical problem named after Rayleigh and Bénard the criterion for the onset of convection in a horizontal fluid layer heated uniformly from below is given in terms of the Rayleigh number.

$$\text{Ra} = \frac{g\alpha d^3 \Delta T}{\nu \mathcal{D}_{\text{th}}},$$

5.4 Comments on possible thermal-convection

with ΔT the imposed temperature difference, d the layer depth and α the volumetric thermal expansion ($\alpha = 0.00367 \text{ K}^{-1}$ for most gases and temperatures for constant pressure [112]). If Ra exceeds the critical Rayleigh number $Ra_c = 1708$ [10], the basic conduction state becomes unstable with respect to convection rolls. At higher Ra transitions to increasingly complex spatio-temporal behavior occur. The case with permeable boundaries was first studied by Shvartsblat [95, 96] in the late 1960's and his results were summarized by Gershuni and Zhukhovitskii [31]. By changing the temperature profile from linear for no-throughflow to exponential for throughflow, convection rolls changed to hexagonal cells for moderate values of throughflow. The problem is of interest because the convective instability can be controlled by changing the throughflow. The theoretical and experimental work of Krishnamurti [56–58] and the numerical work by Somerville and Gal-Chen [102] dealt with this problem from a meteorologist's viewpoint. They obtained a $Ra_c = 1100$ and 657 for rigid-free and free-free conducting boundaries respectively, and found that the mean flow has a stabilizing effect. This problem of permeable boundaries was also studied from a porous media viewpoint. The convection in saturated porous medium was studied by Wooding [116] and Homsy and Sherwood [42]. They confirmed the stabilizing effect of the throughflow. Nield [80] studied the effects of various different boundaries on the onset of convection¹. He obtained a formulation for Ra_c in terms of Prandtl (Pr) and Péclet (Pe) numbers for rigid-rigid, free-free and rigid-free, conducting and/or insulating boundaries. In this problem, the Péclet number is defined as follow

$$Pe = \frac{ud}{\mathcal{D}_{th}},$$

with u the imposed vertical flow. The minimum Ra_c of $Ra_c = 720$ and 120 for rigid-rigid and free-free insulating boundaries respectively was obtained obtained for $Pe = 0$. For the rigid-rigid and free-free insulating case the mean flow always has a stabilizing effect independent of the direction of the

¹Some errors were found in [80] p356 concerning the free-free case, in the third equation the prefactor should be $[\mu^3(1 - e^\mu)]^{-1}$ and in equation (11) one of the terms in the denominator should be $12[\mu^4/(Q + \mu) - \mu^3 - Q^2\mu] \sinh((Q + \mu)/2)$. The limiting cases e.g. $Q \rightarrow \pm\infty$ and $Q \rightarrow 0$ are however not affected.

5. FIRST INVESTIGATION OF CELL FORMATION IN THE NEW BURNER

flow. For the rigid-free insulating case, $Pe > 0$ ($Pe < 0$) was stabilizing (destabilizing) for $Pr < 1.25$ and destabilizing (stabilizing) for $Pr > 1.25$. The critical Ra number at $Pe = 0$ and $Pr = 1.25$ is $Ra_c = 320$. For conducting boundaries Nield confirmed the values obtained by Krishnamurti using a single-term Galerkin method, see [56, 80] for more details.

A similar problem was treated in the context of internal heat generation in porous media. For example, Sparrow *et al.* [105] studied the convection in the Earth's mantle where radioactive materials are heat sources. Shivakumara and Suma [93] and Shivakumara [92] recently studied the onset of convection by using linear stability theory.

The problem of reaction-diffusion coupled with Rayleigh–Bénard convection and throughflow problem has received much less attention. Recently, the experiments of Vaezi and Aldredge [108] motivated a numerical work by Bayliss *et al.* [3] who investigated the combustion of premixed flames in a Taylor–Couette apparatus. The reason for which this problem has not been studied for diffusion flames is that steady state conditions — continuing supply of fresh reactive gas — could not be achieved. As seen previously, the 1-D unstrained ideal model studied by theoreticians [12, 53] does not have this problem and with the new burner developed (see Sec. 4) the fluid-flame interaction problem can be analyzed.

For the 1-D unstrained diffusion flames, the most appropriate boundary condition appears to be free-rigid conducting because of the presence of the metallic oxidizer injection manifold. To determine if the instabilities seen and reported in Sec. 5.2 are coupled with a reactive Rayleigh–Bénard problem, the Ra number must be calculated. The layer depth d is now the flame standoff distance x_f . In Fig. 5.4, the Rayleigh number, Ra, is plotted against x_f and the Péclet number, Pe. The imposed temperature difference ΔT was estimated to be 0.4 times the exit temperature T_e (see Fig. 4.8, in Sec. 4.4.2). The other values come from the experiment described in Sec. 4.4.3 where Table 4.1 contains the extreme values. The solid symbols are $H_2 = 30\%$ vol. From Fig. 5.1, no cellular flames exist above this concentration. The values of Ra fall in the range $Ra \in [100, 800]$. These values are below Ra_c as defined by Krishnamurti and Nield. Comparisons with the literature have to be made with caution, however, as all these studies were done with a single species.

5.4 Comments on possible thermal-convection

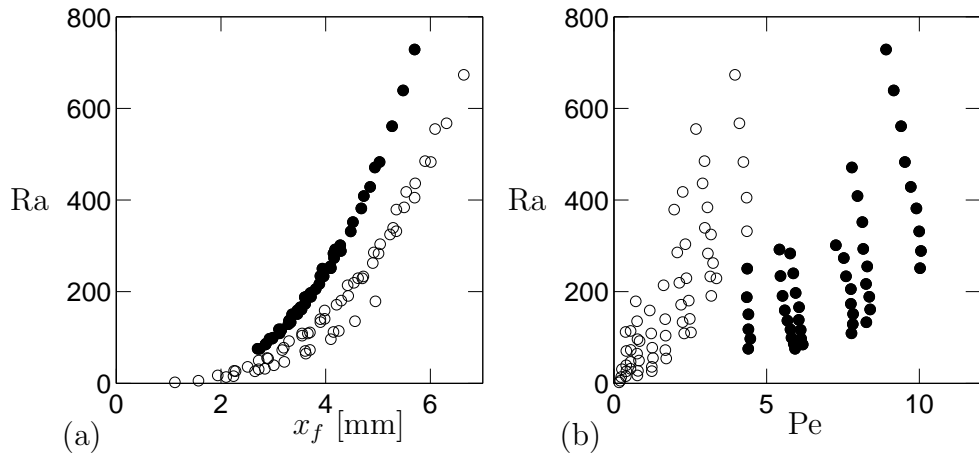


Figure 5.4: Rayleigh number calculated for a H_2 - O_2 diluted in CO_2 diffusion flames (a) versus standoff distance x_f ; (b) versus Péclet number for conditions taken at the flame position. The solid symbols represent the 30% vol. of H_2 , and the open symbols represent the other conditions defined in Table 4.1

It can be concluded that the cellular behavior of the flame is most likely not due to thermal convective instabilities (hexagonal cellular pattern [56]) *above* the flame.

5. FIRST INVESTIGATION OF CELL FORMATION IN THE NEW BURNER

Chapter 6

Summary and future work

Cellular instabilities found near the extinction limit were experimentally investigated in jet diffusion flames and in a 1-D unstrained flame.

For the jet diffusion flames, several parameters controlling the cellular instability of non-premixed hydrogen-oxygen diluted in carbon dioxide flames were identified and systematically investigated. The effect of reactant composition on cellular instabilities has been experimentally studied. The propensity of cellular instabilities increases with decreasing initial mixture strength. In addition, as the initial mixture strength near the extinction condition increases, experiments show that the propensity for the formation of a rotating one-cell state also increases. In accordance with previous work, cellularity in the non-premixed jet flame experiments was promoted by reducing the system Damköhler number and/or the reactant Lewis numbers. The experimental observations were in good agreement with the model proposed by Cheatham and Matalon [12], even though the model does not include hydrodynamic effects. The effect of jet velocity in cellular instabilities has also been experimentally studied. The propensity of the cellular instabilities decreases with increasing jet velocity, however, the extinction limit is less affected by increasing jet velocity. Additional experimental work on the scaling of the cellular wavelength has been undertaken. It has been shown that the cellular wavelengths for jet diffusion flames were dependent on the initial vorticity thickness. More precisely, the cellular wavelength increases with the square root of the vorticity thickness for jet burners.

6. SUMMARY AND FUTURE WORK

In order to compare the results with the idealized model, a novel burner producing a nearly 1-D unstrained flame has been realized. Although the burner is still under development, preliminary results of cellular instabilities have been examined. When the oxidizer diffuses against the bulk flow, the current study has shown that the propensity of cellular instabilities increases with decreasing initial mixture strength, in agreement with theoretical predictions and experimental investigations in jet diffusion flames. When the fuel diffuses against the bulk flow, no cells have so far been observed near the extinction limit, despite the high initial mixture strength. Thermal-convection as a driving mechanism in this novel burner is excluded.

Future work

On the jet diffusion flames, additional experimental data is needed in order to find the quantitative dependence on other parameters such as the Lewis numbers. This can be done by changing the fuel mixture and/or the oxidizer mixture with other inerts. Comparison with other jet burners will confirm the dependence of the cellular wavelength with the square root of the initial vorticity thickness. By changing the Lewis numbers and/or other parameters, the theoretical behavior of pulsating cells may be systematically studied.

On the unstrained diffusion flames, the next step will consist in lowering the oxidizer Lewis number and minimizing the effects of heat loss. Minimizing the oxidizer Lewis number will allow studying the effect of the reactant convected through the flame zone, which is known to play a significant role in determining the conditions for thermo-diffusive instabilities in non-premixed flames. Accurate measurements of the effective mixture burning with a mass spectrometer will allow exact definition of the different burning regime. Several associated studies such as kinetic modeling and thermo-diffusive analysis instability are also possible.

Another interesting proposition will be the realization of the ‘real’ ideal diffusion flame. The ideal situation for a diffusion flame is when there are no hydrodynamic forces. The flame will be produced only by the diffusion of both reactants against the product. The experimental realization of such a burner is possible if one replaces the bottom inlet with a device identical to

the top inlet/outlet. A second manifold of needles will allow the products to escape in between the needles at each side of the burner. This realization will be difficult considering the necessity of controlling the pressure drop to avoid any bulk flow above the flame, promoted by buoyancy. However, despite the technical issues, cellular instabilities in this idealized burner version should behave as Turing structures and the patterns should scale with Turing's chemical wavelength.

6. SUMMARY AND FUTURE WORK

Appendix A

Thermal properties of the reactants

The current investigation involved hydrogen flames burning in oxygen diluted with carbon dioxide. The physical properties presented here were calculated with the Sandia package [46] (see Sec. 2.2.1). Densities, kinematic viscosities, thermal diffusivities, mass diffusivities, Lewis and Prandtl numbers of pure fuel and oxidizer are given versus temperature in Fig. A.1. For a H₂-O₂ diluted in CO₂ mixture, the kinematic viscosities and Prandtl numbers (Fig. A.2), the Lewis numbers of fuel and oxidizer (Fig. A.3) and the Schmidt numbers of fuel and oxidizer (Fig. A.4) are given for several temperatures.

A. THERMAL PROPERTIES OF THE REACTANTS

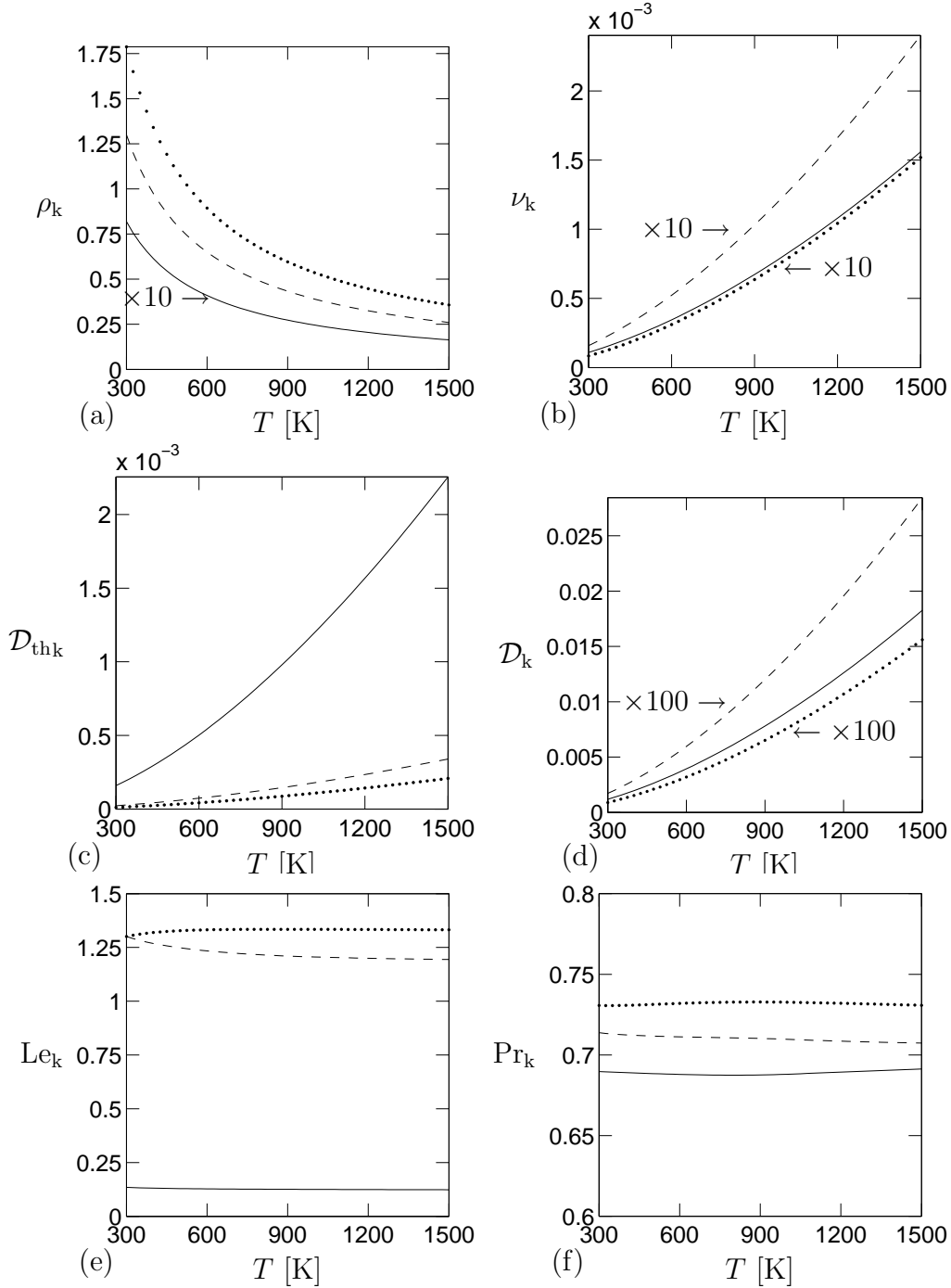


Figure A.1: Properties of pure H_2 (solid lines), pure O_2 (dashed lines) and pure CO_2 (dotted lines) versus temperature. (a) Densities, ρ_k ; (b) Kinematic viscosities ν_k ; (c) Thermal diffusivity \mathcal{D}_{thk} ; (d) Mass diffusivity \mathcal{D}_k ; (e) Lewis number Le_k ; (f) Prandtl number Pr_k .

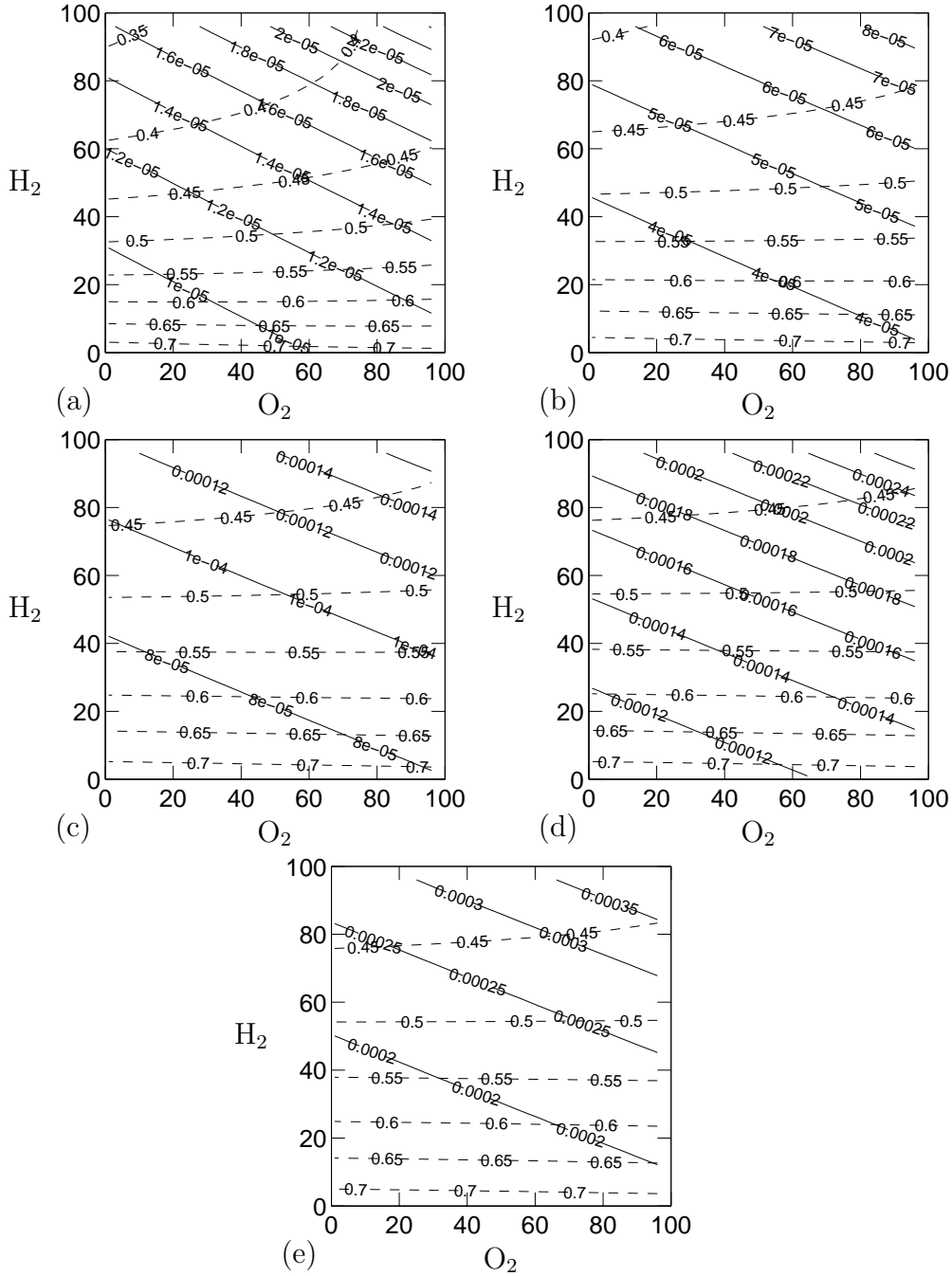


Figure A.2: Kinematic viscosities and Prandtl numbers of H₂-O₂ diluted in CO₂ mixtures. Solid lines kinematic viscosities ν ; dashed lines represents Prandtl number Pr. (a) $T = 300$ K; (b) $T = 600$ K; (c) $T = 900$ K; (d) $T = 1200$ K; (e) $T = 1500$ K;

A. THERMAL PROPERTIES OF THE REACTANTS

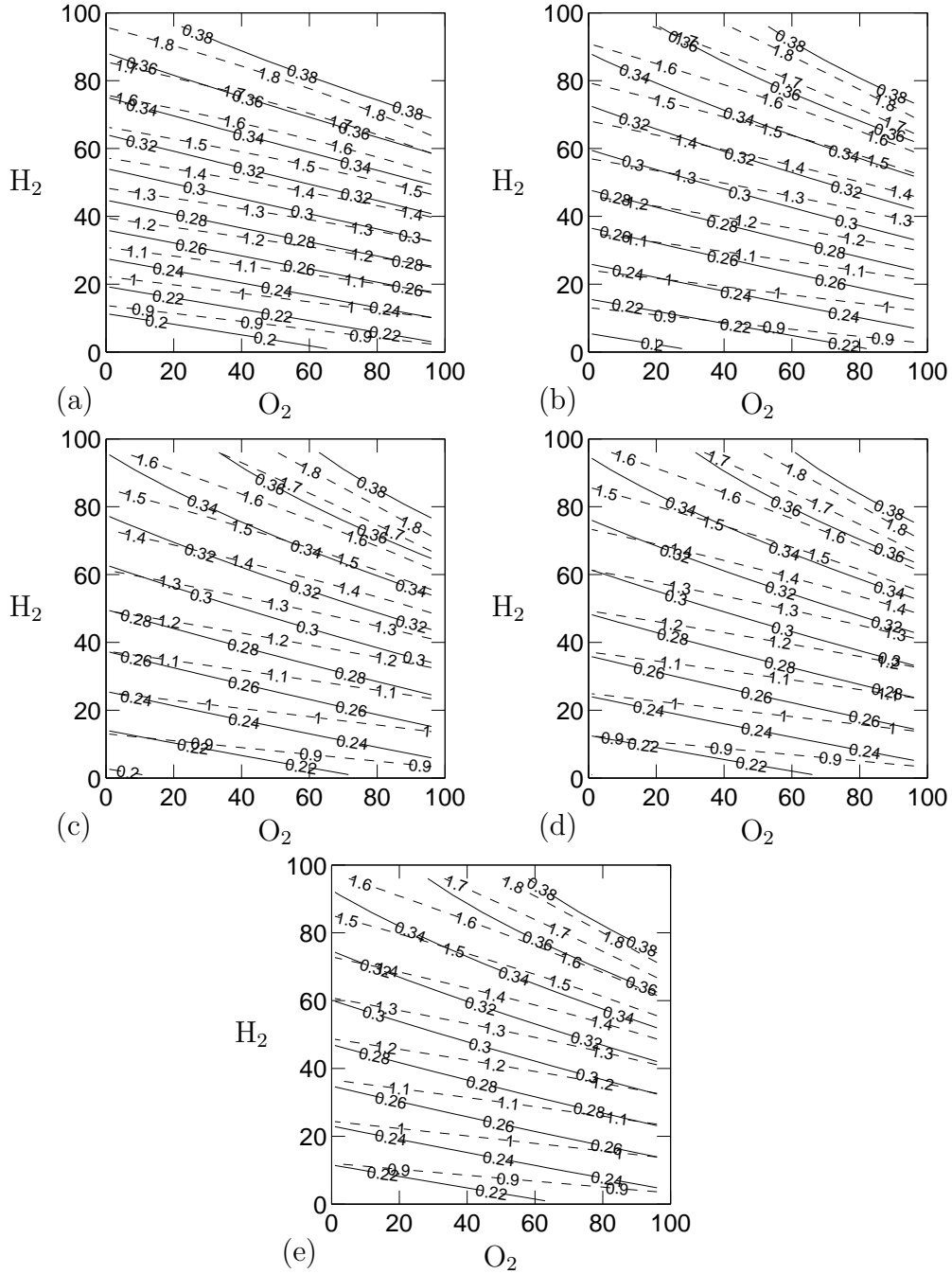


Figure A.3: Fuel and oxidizer Lewis numbers for H_2 - O_2 diluted in CO_2 mixtures. Solid lines represents fuel Lewis number Le_F ; dashed lines represents oxygen Lewis number Le_O . (a) $T = 300$ K; (b) $T = 600$ K; (c) $T = 900$ K; (d) $T = 1200$ K; (e) $T = 1500$ K;

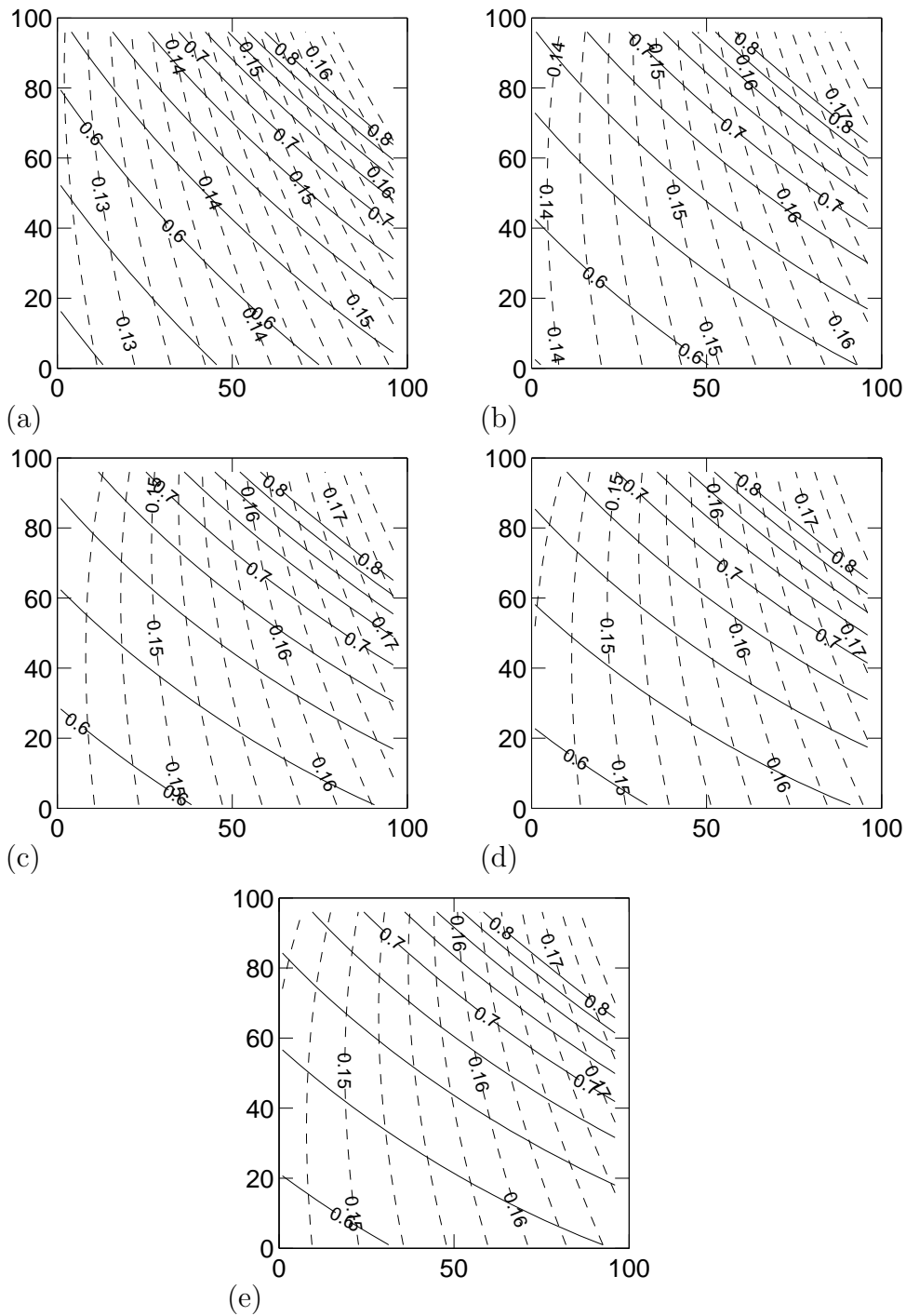


Figure A.4: Fuel and oxidizer Schmidt numbers ($Sc_k = Le_k Pr$) of H_2-O_2 diluted in CO_2 mixtures. Solid lines represents fuel Schmidt number Sc_F ; dashed lines represents oxygen Schmidt number Sc_O . (a) $T = 300$ K; (b) $T = 600$ K; (c) $T = 900$ K; (d) $T = 1200$ K; (e) $T = 1500$ K;

A. THERMAL PROPERTIES OF THE REACTANTS

Bibliography

- [1] Adler, I., Barabe, D. & Jean, R. V. A history of the study of phyllotaxis. *Annals of Botany*, **80**, 231–244, 1997.
- [2] Barenblatt, G. I., Zeldovich, Y. B. & Istratov, A. G. On diffusional thermal instability of laminar flame. *Prikl. Mekh. Tekh. Fiz.*, **2**, 2126, 1962.
- [3] Bayliss, A., Ma, T. K., Matkowsky, B. J. & Wahle, C. W. The reactive Rayleigh-Bénard problem with throughflow. *SIAM J. Appl. Math.*, **61** (4), 1103–1142, 2000.
- [4] Bénard, H. Les tourbillons cellulaires dans une nappe liquide. *Rev. Gen. Sci. pures et appl.*, **11**, 1261–1309, 1900.
- [5] Bradshaw, P. *An Introduction to Turbulence and its Measurement*. Pergamon Press, 1971.
- [6] Bruun, H. H. *Hot-Wire Anemometry, Principles and Signal Analysis*. Oxford Science Publications, 1995.
- [7] Buckmaster, J. The structure and stability of laminar flames. *Ann. Rev. Fluid Mech.*, **25**, 21–53, 1993.
- [8] Buckmaster, J. & Ludford, G. S. S. *Theory of Laminar flames*. Cambridge University Press, 1982.
- [9] Burke, S. P. & Schumann, T. E. Diffusion flames. *Indust. Engng Chem.*, **20**, 998–1004, 1928.

BIBLIOGRAPHY

- [10] Busse, F. H. Stability of finite amplitude cellular convection and its relation to an extremum principle. *J. Fluid Mech.*, **30**, 625–650, 1967.
- [11] Castets, V., Dulos, E., Boissonade, J. & De Kepper, P. Experimental evidence of a sustained standing Turing-type nonequilibrium chemical pattern. *Phys. Rev. Letters*, **64** (24), 2953–2956, 1990.
- [12] Cheatham, S. & Matalon, M. A general asymptotic theory of diffusion flames with application to cellular instability. *J. Fluid Mech.*, **414**, 105–144, 2000.
- [13] Chen, R.-H., Mitchell, G. B. & Ronney, P. D. Diffusive-thermal instability and flame extinction in non-premixed combustion. *Proc. Comb. Inst.*, **24** (3), 213–221, 1992.
- [14] Chung, S. H. & Law, C. K. Structure and extinction of convective diffusion flames with general Lewis numbers. *Combust. Flame*, **52**, 59–79, 1983.
- [15] Clavin, P. Dynamic behavior of premixed flame fronts in laminar and turbulent flows. *Prog. Energy Combust. Sci.*, **11**, 1–59, 1985.
- [16] Dahm, W. J. A. & Dimotakis, P. E. Measurements of entrainment and mixing in turbulent jets. *AIAA J.*, **25**, 1216–1223, 1987.
- [17] D’Arcy Thompson, W. *On growth and form*. Cambridge University Press, 2nd ed. edition, 1979. reprinted.
- [18] Darrieus, G. Propagation d’un front de flamme. Unpublished work presented at La Technique Moderne (and at Congrès de Mécanique Appliquée Paris, 1945), 1938.
- [19] De Kepper, P., Castets, V., Dulos, E. & Boissonade, J. Turing-type chemical patterns in the chloride-iodite-malonic acid reaction. *Physica D*, **49**, 161–169, 1991.
- [20] Dimotakis, P. E. Turbulent free shear layer mixing and combustion. *Progress in Astronautics and Aeronautics*, **137**, AIAA, 1991.

BIBLIOGRAPHY

- [21] Dixon-Lewis, G. Flame structure and flame reaction kinetics, 2. transport phenomena in multicomponent systems. *Proc. R. Soc. Lond. A*, **307** (1488), 111–135, 1968.
- [22] Dongworth, M. R. & Melvin, A. Transition to instability in a steady hydrogen-oxygen diffusion flame. *Combust. Sci. Technol.*, **14** (4-6), 177–182, 1976.
- [23] Du, J. & Axelbaum, R. L. The effects of flame structure on extinction of CH₄/N₂/O₂ diffusion flames. *Proc. Comb. Inst.*, **26**, 1137–1142, 1996.
- [24] Durst, F., Melling, A. & Whitelaw, J. H. *Principles and practice of Laser-Doppler Anemometry*. Academic Press, 1979.
- [25] Fisher, R. A. The advance of advantageous genes. *Ann. Eugenics*, **7**, 335–369, 1937.
- [26] Füre, M. *Non-premixed jet flame instabilities*. PhD thesis, No. 2468, École Polytechnique Fédérale de Lausanne, Lausanne, Switzerland, 2001.
- [27] Füre, M., Papas, P. & Monkewitz, P. A. Non-premixed jet flame pulsations near extinction. *Proc. Comb. Inst.*, **28**, 831–838, 2000.
- [28] Gardiner, W. C., editor. *Combustion Chemistry*. Springer, 1984.
- [29] Garside, J. E. & Jackson, B. Polyhedral diffusion flames. *Nature*, **168** (4286), 1085, 1951.
- [30] Garside, J. E. & Jackson, B. The formation and some properties of polyhedral burner flames. *Proc. Comb. Inst.*, **4**, 545–552, 1953.
- [31] Gershuni, G. Z. & Zhukhovitskii, E. M. *Convective stability of incompressible fluids*. Israel Program Scientific Translations., 1976.
- [32] Glassman, I. *Combustion*. Academic Press, San Diego CA 92101, (1996)., 3rd edition.

BIBLIOGRAPHY

- [33] Gorman, M., Elhamdi, M., Pearson, B. & Robbins, K. A. Ratcheting motion of concentric rings in cellular flames. *Phys. Rev. Lett.*, **76** (2), 228–231, 1996.
- [34] Gorman, M., Hamill, C. F., Elhamdi, M. & Robbins, K. A. Rotating and modulated rotating states of cellular flames. *Combust. Sci. Technol.*, **98** (1-3), 25–35, 1994.
- [35] Han, B., Ibarreta, A. F., Sung, C.-J. & T'ien, J. S. Experimental low-stretch gaseous diffusion flames in buoyancy-induced flowfields. *Proc. Comb. Inst.*, **30** (1), 527–535, 2005.
- [36] Harrison, L. G. *Kinetic theory of living pattern*. Cambridge University Press, 1993.
- [37] Harrison, L. G. & von Aderkas, P. Spatially quantitative control of the number of cotyledons in a clonal population of somatic embryos of hybrid larch *larix × leptoeuropaea*. *Annals of Botany*, **93**, 423–434, 2004.
- [38] Hertig, J.-A., Keller, J.-C. & Liska, P. Climod, sonde thermo-anemometrique directionnelle. Technical Report 501.169/Hr/dp, Dept. génie civil, EPFL, 1980.
- [39] Hirschfelder, J. O., Curtiss, C. F. & Bird, R. B. *Molecular Theory of Gases and Liquids*. John Wiley, 2nd edition edition, 1963.
- [40] Hjelmfelt Jr, A. T. & Mockros, L. F. Motion of discrete particles in a turbulent fluid. *Appl. Sci. Res.*, **16**, 149–161, 1965.
- [41] Ho, C.-M. & Huerre, P. Perturbed free shear layers. *Ann. Rev. Fluid Mech.*, **16**, 365–424, 1984.
- [42] Homsy, G. M. & Sherwood, A. E. Convective instabilities in porous-media with through flow. *AIChE J.*, **22** (1), 168–174, 1976.
- [43] Ishizuka, S. & Tsuji, H. An experimental study of effect of inert gases on extinction of laminar diffusion flames. *Proc. Comb. Inst.*, **18**, 695–703, 1981.

BIBLIOGRAPHY

- [44] Jean, R. V. *Phyllotaxis: a systematic study in plant morphogenesis*. Cambridge University Press, 1994.
- [45] Joulin, G. & Clavin, P. Linear-stability analysis of non-adiabatic flames — diffusional-thermal model. *Combust. Flame*, **35** (2), 139–153, 1979.
- [46] Kee, R. J., Dixon-Lewis, G., Warnatz, J., Coltrin, M. E. & Miller, J. A. A fortran computer code package for the evaluation of gas-phase multicomponent transport properties. Technical report, Sandia National Laboratories, 1986.
- [47] Kee, R. J., Warnatz, J. & Miller, J. A. A fortran computer code package for the evaluation of gas-phase viscosities, conductivities, and diffusion coefficients. Technical Report SAND83-8209, Sandia National Laboratories, 1983.
- [48] Kim, J. S. Diffusional-thermal instability of diffusion flames in the premixed-flame regime. *Combust. Sci. Technol.*, **118**, 27–48, 1996.
- [49] Kim, J. S. Linear analysis of diffusional-thermal instability in diffusion flames with Lewis numbers close to unity. *Combust. Theory and Modelling*, **1** (1), 13–40, 1997.
- [50] Kim, J. S. & Lee, S. R. Diffusional-thermal instability in strained diffusion flames with unequal Lewis numbers. *Combust. Theory and Modelling*, **3** (1), 123–146, 1999.
- [51] Kim, J. S. & Williams, F. A. Extinction of diffusion flames with nonunity Lewis numbers. *J. Eng. Math.*, **31**, 101–118, 1997.
- [52] Kim, J. S., Williams, F. A. & Ronney, P. D. Diffusional-thermal instability of diffusion flames. *J. Fluid Mech.*, **327**, 273–301, 1996.
- [53] Kirkby, L. L. & Schmitz, R. A. An analytical study of stability of laminar diffusion flame. *Combust. Flame*, **10** (3), 205–220, 1966.
- [54] Kolmogorov, A. N., Petrovsky, I. G. & Piskunov, N. S. Study of the diffusion equation with growth of the quantity of matter and its appli-

BIBLIOGRAPHY

- cation to a biology problem. *Moscow Univ. Math. Bull. Ser. Int. A*, **1**, 1–26, 1937.
- [55] Koschmeider, E. L. *Bénard cells and Taylor vortices*. Cambridge University Press, 1993.
- [56] Krishnamurti, R. Cellular cloud patterns. Part 1: Mathematical model. *J. Atmos. Sci.*, **32** (7), 1353–1363, 1975.
- [57] Krishnamurti, R. Cellular cloud patterns. Part 2: Laboratory model. *J. Atmos. Sci.*, **32** (7), 1364–1372, 1975.
- [58] Krishnamurti, R. Cellular cloud patterns. Part 3: Applicability of mathematical and laboratory models. *J. Atmos. Sci.*, **32** (7), 1373–1383, 1975.
- [59] Kukuck, S. & Matalon, M. The onset of oscillations in diffusion flames. *Combust. Theory and Modelling*, **5** (2), 217–240, 2001.
- [60] Kurdyumov, V. N. & Matalon, M. Radiation losses as a driving mechanism for flame oscillations. *Proc. Comb. Inst.*, **29**, 45–52, 2003.
- [61] Landau, L. On the theory of slow combustion. *Acta Physicochimica URSS*, **19**, 77–85, 1944.
- [62] Lee, S. R. & Kim, J. S. Nonlinear dynamic characteristics of flame stripes formed in strained diffusion flames by diffusional-thermal instability. *Combust. Theory and Modelling*, **4** (1), 29–46, 2000.
- [63] Lee, S. R. & Kim, J. S. On the sublimit solution branches of the stripe patterns formed in counterflow diffusion flames by diffusional-thermal instability. *Combust. Theory and Modelling*, **6** (2), 263–278, 2002.
- [64] Liñan, A. Asymptotic structure of counterflow diffusion flames for large activation-energies. *Acta Astronautica*, **1** (7-8), 1007–1039, 1974.
- [65] Lo Jacono, D., Papas, P., Matalon, M. & Monkewitz, P. A. A nearly 1-d non-premixed flame near extinction. Cell formation and the effect of the direction of bulk flow. ICTAM, 2004.

BIBLIOGRAPHY

- [66] Lo Jacono, D., Papas, P., Matalon, M. & Monkewitz, P. A. An experimental realization of an unstrained planar diffusion flame. *Proc. Comb. Inst.*, **30** (1), 501–509, 2005.
- [67] Lo Jacono, D., Papas, P. & Monkewitz, P. A. Cell formation in non-premixed, axisymmetric jet flames near extinction. *Combust. Theory and Modelling*, **7** (4), 635–644, 2003.
- [68] Markstein, G. H. *Non-steady flame propagation*. Pergamon Oxford, 1964.
- [69] Matalon, M., Ludford, G. S. S. & Buckmaster, J. Diffusion flames in a chamber. *Acta Astronautica*, **6**, 943–959, 1979.
- [70] Matalon, M. & Matkowsky, B. J. Flames as gasdynamic discontinuities. *J. Fluid Mech.*, **124**, 239–259, 1982.
- [71] Matalon, M. & Matkowsky, B. J. Flames in fluids: Their interactions and stability. *Combust. Sci. Technol.*, **34**, 295–316, 1983.
- [72] Meinhardt, H. *Positional Control in Plant Development*, chapter Models of pattern formation and their application to plant development. Cambridge University Press, 1984.
- [73] Melling, A. Tracer particles and seeding for particle image velocimetry. *Meas. Sci. Technol.*, **8** (12), 1406–1416, 1997.
- [74] Michalke, A. Survey on jet instability theory. *Prog. Aerospace Sci.*, **21**, 159–199, 1984.
- [75] Michelson, D. M. & Sivashinsky, G. I. Non-linear analysis of hydrodynamic instability in laminar flames. 2. numerical experiments. *Acta Astronautica*, **4**, 1207–1221, 1977.
- [76] Monchick, L. & Mason, E. A. Transport properties of polar gases. *J. Chem. Phys.*, **35**, 1676–1697, 1961.
- [77] Monkewitz, P. A. & Huerre, P. The influence of the velocity ratio on the spatial instability of mixing layers. *Phys. Fluids*, **25** (7), 1137–1143, 1982.

BIBLIOGRAPHY

- [78] Monkewitz, P. A., Simon, J. & Pfizenmaier, E. On the instability behavior of laminar hydrogen- and hydrogen-helium jet diffusion flames. *Deutsche Forschungsanstalt für Luft und Raumfahrt e. V.*, 1992.
- [79] Mungal, M. G. & Dimotakis, P. E. Mixing and combustion with low heat release in a turbulent shear layer. *J. Fluid Mech.*, **148**, 349–382, 1984.
- [80] Nield, D. A. Throughflow effects in the Rayleigh–Bénard convective instability problem. *J. Fluid Mech.*, **185**, 353–360, 1987.
- [81] Ouyang, Q., Boissonade, J., Roux, J. C. & de Kepper, P. Sustained reaction-diffusion structures in an open reactor. *Phys. Lett. A*, **134**, 282–286, 1989.
- [82] Palacios, A., Gunaratne, G. H., Gorman, M. & Robbins, K. A. Cellular pattern formation in circular domains. *Chaos*, **7** (3), 463–475, 1997.
- [83] Papas, P., Monkewitz, P. A. & Tomboulides, A. G. New instability modes of a diffusion flame near extinction. *Phys. Fluids*, **11** (10), 2818–2820, 1999.
- [84] Papas, P., Rais, R. M., Monkewitz, P. A. & Tomboulides, A. G. Instabilities of diffusion flames near extinction. *Combust. Theory and Modelling*, **7** (4), 603–633, 2003.
- [85] Peters, N. *Turbulent combustion*. Cambridge University Press, U.K., (2000)., 2000.
- [86] Pfizenmaier, E., Simon, J. & Monkewitz, P. A. Gallery of fluid motion. *Physics of Fluids A*, **9**, 547–565, 1993.
- [87] Rais, R. M. *Numerical investigations of diffusion flame instabilities*. PhD thesis, No. 2700, École Polytechnique Fédérale de Lausanne, Lausanne, Switzerland, 2002.
- [88] Rashevsky, N. An approach to the mathematical biophysics of biological self-organization and of cell polarity. *Bull. Math. Biophys.*, **2**, 15–21, 1940.

BIBLIOGRAPHY

- [89] Rayleigh. On the convective currents in a horizontal layer of fluid when the higher temperature is on the under side. *Phil. Mag.*, **32**, 529–546, 1916.
- [90] Saunders, P. T., editor. *Morphogenesis*, volume 3 of *Collected work of A. M. Turing*. Elsevier Science, 1992.
- [91] Schlichting, H. *Boundary-Layer theory*. McGraw-Hill, Inc., 7th edition.
- [92] Shivakumara, I. S. Boundary and inertia effects on convection in porous media with throughflow. *Acta Mech.*, **137** (3-4), 151–165, 1999.
- [93] Shivakumara, I. S. & Suma, S. P. Effects of throughflow and internal heat generation on the onset of convection in a fluid layer. *Acta Mech.*, **140** (3-4), 207–217, 2000.
- [94] Shvab, V. A. Relation between the temperature and velocity fields of the flame of a gas burner. *Gos. Energ.*, 1948.
- [95] Shvartsblat, D. L. The spectrum of perturbations and convective instability of a plane horizontal fluid layer with permeable boundaries. *J. Appl. Mech. (PMM). Translation from Prikl. Mat. Mekh.*, **32** (2), 266–271, 1968.
- [96] Shvartsblat, D. L. Steady convective motions in a plane horizontal fluid layer with permeable boundaries. *Fluid Dyn. Translation from Izv. Akad. Nauk SSSR, Fiz. Zhidkosti i Gaza.*, **4**, 54–59, 1969.
- [97] Sivashinsky, G. I. Diffusional-thermal theory of cellular flames. *Combust. Sci. Technol.*, **15** (3-4), 137–146, 1977.
- [98] Sivashinsky, G. I. Non-linear analysis of hydrodynamic instability in laminar flames. 1. derivation of basic equations. *Acta Astronautica*, **4**, 1177–1206, 1977.
- [99] Sivashinsky, G. I. Instabilities, pattern-formation, and turbulence in flames. *Ann. Rev. Fluid Mech.*, **15**, 179–199, 1983.

BIBLIOGRAPHY

- [100] Smithells, A. & Ingle, H. The structure and chemistry of flames. *J. Chem. Soc. Trans.*, **61**, 204–216, 1892.
- [101] Sohn, C. H., Chung, S. H. & Kim, J. S. Instability-induced extinction of diffusion flames established in the stagnant mixing layer. *Combust. Flame*, **117**, 404–412, 1999.
- [102] Somerville, R. C. J. & Gal-Chen, T. Numerical-simulation of convection with mean vertical motion. *J. Atmos. Sci.*, **36** (5), 805–815, 1979.
- [103] Spalding, D. B. A theory of the extinction of diffusion flames. *Fuel*, pages 255–273, 1954.
- [104] Spalding, D. B. & Jain, V. K. Theoretical study of effects of chemical kinetics on a one-dimensional diffusion flame. *Combust. Flame*, **6** (4), 265, 1962.
- [105] Sparrow, E. M., Goldstein, R. J. & Jonsson, V. K. Thermal instability in a horizontal fluid layer: effect of boundary conditions and nonlinear temperature profile. *J. Fluid Mech.*, **18**, 513–529, 1964.
- [106] Taylor, G. I. The instability of liquid surfaces when accelerated in a direction perpendicular to their planes. *Proc. R. Soc. Lond. A*, **201**, 192–196, 1950.
- [107] Turing, A. M. The chemical basis of morphogenesis. *Phil. Trans. R. Soc. Lond. B*, **237**, 37–72, 1952.
- [108] Vaezi, V. & Aldredge, R. C. Laminar-flame instabilities in a Taylor–Couette combustor. *Combust. Flame*, **121** (1-2), 356–366, 2000.
- [109] Wardlaw, C. W. A commentary on Turing’s diffusion-reaction theory of morphogenesis. *New Phytologist*, **52**, 40–47, 1952.
- [110] Wardlaw, C. W. Evidence relating to the diffusion-reaction theory of morphogenesis. *New Phytologist*, **54**, 39–49, 1954.
- [111] Warnatz, J. *Influence of Transport Models and Boundary Conditions on Flame Structure*. Numerical Methods in Flame Propagation. Friedr. Vieweg and Sohn, 1982.

BIBLIOGRAPHY

- [112] Weast, R. C., editor. *Handbook of Chemistry and Physics*. CRC Press, 55th edition edition, 1975.
- [113] Williams, F. A. *Combustion Theory*. Addison–Wesley, 1985.
- [114] Williams, T. J., Ali, M. R. M. H. & Anderson, J. S. Noise and flow characteristics of coaxial jets. *J. Mech. Eng. Sci.*, **11**, 133, 1969.
- [115] Wolpert, L., Beddington, R., Jessell, T., Lawrence, P., Meyerowitz, E. & Smith, J. *Principles of Development*. Oxford University Press, second edition edition, 2002.
- [116] Wooding, R. A. Rayleigh instability of a thermal boundary layer in flow through a porous medium. *J. Fluid Mech.*, **9**, 183–192, 1960.
- [117] Yule, A. J., Chigier, N. A., Ralph, S., Boulderstone, R. & Ventura, J. Combustion-transition interaction in a jet flame. *AIAA J.*, **19** (6), 752–760, 1981.
- [118] Zeldovich, Y. B. On the theory of combustion of initially unmixed gases. Translation 1296, NACA, 1951. Translation from K Teorii Gorenia Neperemeshannykh Gasov.

BIBLIOGRAPHY

Curriculum Vitae

David LO JACONO

Av. de Beaulieu, 7

CH-1004 Lausanne

tel: +44 21 311 1676

email:

david.lojacono@epfl.ch

Date and place of birth: April, 13 1977, Paris,
France.

Nationality: French

Education

2005 PhD at the Swiss Federal Institute of Technology, Lausanne (Switzerland)

Title: "Experimental study of cellular instabilities in non-premixed flames."

Advisor: Professor Peter Monkewitz.

2001 MSc. in Fluid Dynamics, University of Toulouse/IMFT (France).

Thesis: "Weak inertial flow between two rough surfaces."

Advisors: Pr. Alain Bergeon et Dr. Franck Plouraboué.

1999 BSc. Mechanics, University of Toulouse (France).

1998 BSc. Physics, University of Tours (France).

Publications

Articles

[A1] D. Lo Jacono, F. Plouraboué and A. Bergeon, Weak inertial flow between two rough surfaces, *Phys. of Fluids* 17, 2005

[A2] D. Lo Jacono, P. Papas, M. Matalon and P. A. Monkewitz, An experimental realization of an unstrained, planar diffusion flame, *Proc Combust Inst* 30, 2004.

[A3] D. Lo Jacono, P. Papas and P. A. Monkewitz, Cell formation in non-premixed, axisymmetric jet flames near extinction, *Combustion Theory and Modelling* 7(4), 2003.

International conferences (peer-reviewed with proceedings)

[C1] D. Lo Jacono, F. Plouraboué and A. Bergeon, Weakly inertial flows between rough surfaces, Proceedings of the EFMC Conference, Toulouse, France, Aug 2003.

[C2] D. Lo Jacono, F. Plouraboué, A. Bergeon and P. Assemat, Weak inertia and mixing between rough surfaces, Proceedings of the ICTAM 2004, Warsaw, Poland, Aug 2004.

[C3] D. Lo Jacono, P. Papas, M. Matalon and P. A. Monkewitz, A nearly 1-D non-premixed flame near extinction. Cell formation and the effect of the direction of bulk flow, Proceedings of the ICTAM 2004, Warsaw, Poland, Aug 2004.

National conferences

[CN1] D. Lo Jacono, P. Papas and P. A. Monkewitz, On the formation of cellular instabilities in non-premixed jet flames, Third Joint Meeting of the U.S. Sections of The Combustion Institute, Chicago, USA, Apr 2003.

[CN2] D. Lo Jacono, P. Papas and P. A. Monkewitz, Cell formation in non-premixed, axisymmetric jet flames near extinction, Proceedings of the APS, Newark, U.S.A., Nov 2003.

[CN3] D. Lo Jacono, F. Plouraboué and A. Bergeon, Écoulements faiblement inertiels entre surfaces rugueuses, 6ème Journées sur les Milieux Poreux, Toulouse, France, Nov 2003.